Laser-induced trapping and stabilization of nanostructured metastable metal-oxide phases for energetic applications

A Dissertation Presented for the
Doctor of Philosophy
Degree
The University of Tennessee, Knoxville

Elijah Michael Davis
August 2024

Acknowledgements

I would like to thank my advisor Dibs for his overwhelming mentorship during my PhD. Your ideas and questions kept me on my toes and thinking out of the box. Your methods, whilst unconventional, taught me how to conduct research and molded me into the scientist I am now. I can honestly say that we functioned less as boss and employee and more as two friends uncovering the mysteries of these strange materials. I hope, in the future, to hear from many more students the stories of the scientific explorations undertook by the Mukherjee lab. Thanks Dibs. Dr. Khomami, it is because of you that I am now defending my PhD. When I started you believed in me and agreed to sponsor my admission into the department. You have supported me academically and personally ever since. You have my most sincere appreciation and thanks. To Gerd, I must thank you for teaching me more about materials science than any class. You have been my friend and co-mentor throughout my PhD. I met you in MSE201 and you taught me how to use the TEM as an undergraduate before I got my driver's license. I wish you all the best and hope that you continue to teach students the joys of materials science. Dr. Gottfried, thank you for giving the work we did an application. Without your support our project would not have left the bench top. Thank you for agreeing to be on my committee and thank you for helping us understand the samples we made. Sorry about all the bad ones. I would like to thank the other professors and scientists that had a pivotal role in the research I conducted and the things that I learned. Thank you, Dr. Claudia Rawn and Dr. Michael Koehler, for the help with crystallography and XRD. For the Fridays spent collecting data and the Mondays spent discussing it. The support and feedback from my group members Dr. Erick Ribeiro, Dan Huber, Collin Ferrell, and Amanda Knobbs. You guys made years of memories and showed me what the elemental composition of true friendship was. I could not have asked for better lab mates and I wish you guys happy lives with successful careers. Finally, I would like to thank my family. They were there for the complaints, disappointments, late nights and they will likely be there for more. Thank you.

Abstract

Synthesis of kinetically “frozen” metastable nanostructures remains elusive. This limitation has severely restricted the current paradigms in materials discovery for metal/metal oxide-based energetic nanomaterials (ENMs) that can circumvent the diffusion limitations. Specifically, non-stoichiometric/amorphous Al-oxide (a-AlO_x) structures in metastable states, *albeit* theoretically predicted, are rarely reported in experiments due to the inability to kinetically trap and phase-stabilize such exotic out-of-equilibrium phases at nanoscale. We overcame this challenge by phase-stabilizing unusually hyper-oxidized and metastable amorphous-aluminum oxide (a-AlO_x; $2.5<x\leq3.5$) nanoparticles (NPs). We employed Laser Ablation Synthesis in Solution (LASiS) as a non-equilibrium technique to achieve this pivotal advancement. Structural and compositional characterizations of the as-synthesized material reveal highly disordered a-AlO_x NPs, remarkably stabilized by an interfacial monolayer of ordered carbon (C) atoms. Both structure and chemical composition were confirmed with disparate characterization methods at different length-scales. The nanoparticles of sizes less than 10 nm were stable even at elevated temperatures. Only at temperatures higher than 750^{o}C, the metastable a-AlO_x structures undergo solid-solid phase transition that culminates in the formation of stable α-Al_2O_3 while releasing excess trapped gases. Detailed chemical kinetic analyses for the solid-solid phase transformation were investigated via time-dependent high-temperature XRD, PDF analysis and in-situ high-temperature TEM imaging. The ability to kinetically trap such metastable nanomaterials in localized low-energy troughs, has wide-ranging implications for their potential applications as solid-state gas generator additives that can bypass the diffusion limitations. Furthermore, this thesis presents results for diverse Fe/Al-based carbides, oxides and oxycarbides that can be deployed as functional additives/oxidizers for solid fuels. Results are presented for the synthesis of Fe-oxide/carbide-based NPs with magnetic responses that have the potential for magnetic field-induced heating. To this end, laser and solvent parameters for LASiS are tuned to enable tailored synthesis of ultra-small (2-10 nm) amorphous Fe-oxide NPs, as well as core-shell Fe@Fe_2O_3 (20-40 nm) and Fe_3C@C (20-40 nm) NPs. Detailed structure-composition characterizations are presented that reveal that the crystalline phases and C-shell coatings in the aforesaid composite NPs could be tuned via LASiS under heated toluene. The research described paves the way for future investigations into other such metastable nanomaterials awaiting discovery in the non-equilibrium phase space.

Table of Contents

List of Tables

List of Figures

Chapter 1: Overview and Backgrounds: A case for energetic nanomaterials

1.1 Research Background:

In an era driven by technological innovation, the development and advancement of materials is crucial for revolutionizing industries ranging from aerospace and space exploration to automotive industry and energy storage. High Energy Density Materials (HEDMs), in particular, are at the forefront of this revolution, offering unprecedented capabilities for energy storage and rapid release. These materials are essential for the advancement of rocket propellants, where their ability to store and release vast amounts of energy efficiently can significantly enhance propulsion systems. Among these, metal-based energetic nanomaterials (ENMs), particularly those based on aluminum (Al), have captured the interest of scientists and engineers due to their unique size-dependent properties and exceptional combustion enthalpy which make them ideal candidates for next-generation propellant formulations.

Nanomaterials are materials with structural components that are smaller than 100 nanometers in at least one dimension. At this scale, materials often exhibit unique physical, chemical, and biological properties compared to their bulk counterparts. These properties arise due to the increased surface area to volume ratio, quantum effects, and the dominance of surface energy. Because of this, nanomaterials can exhibit increased strength, hardness, and elasticity compared to their bulk counterparts due to their small grain size and high surface energy.[1,2] This large surface area provides more reactive sites, leading to faster and more efficient chemical reactions. Additionally, the quantum size effects in nanomaterials result in unique electronic, optical, and magnetic properties that can be exploited for various high-energy applications.[2,3] Another advantageous property of nanomaterials in energetic formulations is their lower activation energy, which facilitates the initiation of chemical reactions.[4,5] This is crucial for applications such as rocket propellants, where rapid energy release is essential.[6] The ability to control the size, shape, and composition of nanomaterials during synthesis allows for precise tailoring of their properties, enabling the design of materials with specific burn rates, stability, and energy release profiles [7,8]. Moreover, nanomaterials improve combustion efficiency due to their ability to be mixed uniformly with other reactants, ensuring complete and efficient combustion. This results in higher energy output and better performance in propulsion systems. The small size of nanomaterials also reduces diffusion limitations, allowing for rapid diffusion of reactants to the reaction sites and enhancing overall reaction kinetics. A significant advantage of nanomaterials, which we will go into further detail later, is their potential to exist in metastable phases that are not stable in bulk form.[9,10] These metastable phases can have higher energy densities and unique structure-function properties, offering potential for higher energy output and novel energetic behaviors. The

ability to stabilize these phases for practical use can lead to the development of advanced energetic materials with superior performance characteristics.

Despite these remarkable properties, the widespread application of nanomaterials as HEDMs faces significant scientific and engineering challenges such as rapid oxidation and the formation of passivating layers. These issues can hinder the accessibility of active material and reduce the overall energy release. Addressing these challenges through innovative synthesis and stabilization techniques is the focus of this research, aiming to unlock the full potential of nanomaterials in high-performance rocket propulsion.[5,6,11-14] Past computational and experimental studies have specifically focused on Al nanoparticles (NPs) mixed with oxidizers[15-19] as composite HEDMs for propellant/pyrotechnic applications that have demonstrated high burning rates due to the large combustion enthalpy of Al (~2324 kJ/mol).[20,21] Additionally, the large Laplace pressure (~surface tension/radius) coupled with lowered melting points in particles in the nanoscale size regime (D_p<50nm) induce a significant pressure gradient upon their ignition that leads to the transport-limited oxidation driven by the relative transport fluxes of the reacting species (Al or, O_2) at the interfacial reaction zone[14,20,22-24] that eventually determines the relative reaction kinetics for the Al oxidation. This has led to the well-known hypothesis that relative surface energy and strain increases within a NP with diminishing particle sizes would effectively result in substantially higher enthalpy states and transport that can drastically increase the amounts of energy released above that of a bulk material.

1.2 Past research problems

The large heat release however, in first-generation Al NP-based ENMs was often offset by diffusion-limited sluggish energy release rates due to rapid parasitic oxide layer formations that passivate the NP surfaces, consume significant particle volume as dead loads, and eventually, limit the accessibility of active Al contents (see figure 1.1).[13,20,25-27] Such limitations hinder their long-term performance, storage and handling due to the rapid surface oxide formations upon their exposure to ambient conditions which, in turn, degraded their burn rates and reaction kinetics during on-site munitions/propellant deployment. To address the aforesaid challenges, past efforts have designed tailor-made Metastable Intermolecular Composites (MICs)[28] or resorted to a more innovative approach, as demonstrated in our group's recent work in synthesizing pre-passivated active Al NP surfaces with graphitic C shells via high-energy laser ablation techniques to preserve the active solid Al fuel cores.[29] However, even such efforts could not ensure pure kinetic activations, since they do not preclude diffusion-limited oxidation of the active Al contents available as solid fuel. Furthermore, aforesaid ENMs typically require stoichiometrically mixed

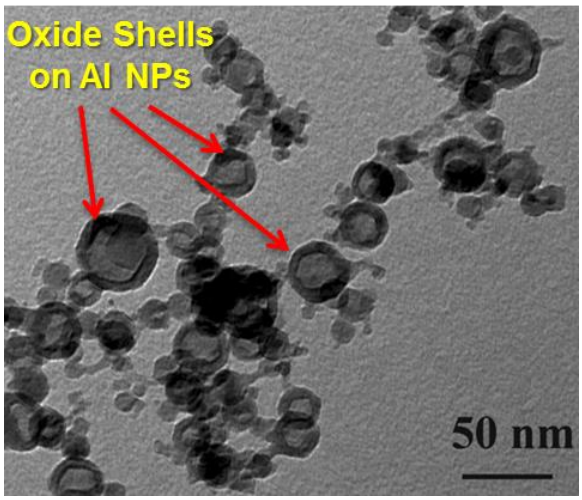

Figure 1.1) TEM image showing surface oxide shell formations in first-generation Al NP-based ENMs.

external oxidizers to ensure oxygen balance during their combustion. For such ENMs, the active fuel-oxidizer interfacial proximity plays an important role in the ensuing reaction kinetics. Non-surface functionalized energetic composites, for which the non-homogeneous blend of active material and oxidizer is less than ideal, can undergo inefficient combustion due to the absence of localized ideal combustion stoichiometry.[30] As a result, efforts toward tuning surface functionalized energetic composites has grown into an active area of investigation in the Al-based energetic materials research community.[30-32] However, typical synthesis routes such as conventional gas-phase condensation, wet chemistry or mechanical ball milling routes used for commercial Al NPs synthesis inevitably result in oxide shell formations during the process; apart from the harsh chemical reagents and surfactants/ligands used that can hinder their interfacial activities. Hence, the need for disruptive high-energy synthesis routes to enable transformative designs for next-generation ENMs made from metastable nanostructures comprising metal/metal-oxide composites that can be stabilized in suitable reactive casings/scaffoldings. Such nanocomposite m-ENMs can preserve their energy contents with high chemical stability over longer periods of storage while enabling rapid, kinetically controlled release under desired activations.[22,24,33,34]

To that end, it would be pertinent to point out here that, throughout the study and development of ENMs, the focus of this community has been solely on thermodynamically stable (equilibrium) materials as they are generally easy to synthesize even at nanoscale. However, as of yet, metastable phases of materials which are kinetically trapped in localized free energy minima with a positive free energy above that of the equilibrium state, have not been investigated for ENM applications. Metastable nanostructures could hold the key to engineering effective next-generation ENMs by combining the exotic properties arising from their kinetic entrapments in the non-equilibrium phase space that can allow non-diffusion-limited energy release mechanisms and unique structure-function properties resulting from their nanoscale size effects. Even though metastable nanomaterials have the aforesaid unique advantages, their synthesis-structure-functionality relations are only very recently being studied and understood. The main drawbacks to their study and implementation are the difficulty in their synthesis and stabilization coupled with a weak understanding of the ill-defined non-equilibrium phase space of materials.[35-37] A rough idea of which metastable phases can exist is an immense ongoing study utilizing large-scale computational techniques using density-functional theories (DFT) facilitated by the advent of supercomputing capabilities.[35] However, only a handful of studies have carried out any detailed experimental investigations into the real-life synthesis and entrapment of metastable structures.[35] The few cases studied that were able to produce metastable nanomaterials were through the use

of highly non-equilibrium synthesis routes such as ultra-fast quenching, physical/chemical deposition, ultra-high-pressure compression and non-thermal plasma reactors or "dusty plasma reactors".[10,38] These synthesis routes however are not capable of the large-scale manufacturing required for proper study and implementation into technology. To that end, recent studies have indicated the capabilities of laser-induced plasmas including Laser Ablation Synthesis in Solution (LASiS) as high-energy non-equilibrium routes to synthesize diverse classes of functional metastable and composite metal-oxide nanoparticles.[38,39] Bearing that in mind, this report lays out the detailed project descriptions, objectives, executables and deliverables for the PhD project on LASiS-driven design and facile synthesis of high-purity metastable metal-oxide-based nanocomposites (NCs) as next-generation metastable-ENMs (m-ENMs), and their detailed synthesis-structure-property characterizations.

1.3 Project Description: A conspectus for the current study

1.3.1 Kinetically Trapped Metastable Metal-Oxide (m-MO_x) *as Activators/Oxidizers*

For a conceptual understanding of the impact and significance of this PhD research, this section is dedicated to discussing the broader scientific implications of the materials to be developed during this project specifically for energetic applications. As discussed earlier, the drawbacks of diffusion-limited oxidation in first-generation Al-based ENMs have propelled the search for kinetically-controlled ENMs at the forefront of our current research efforts. The inherent challenges of diffusion-limited Al-oxidation can be explained from the Arrhenius-based heterogeneous gas-solid diffusion coefficient: D_{GB} (m^2/s) ~α. exp ($-\beta/R_uT$), where R_u = universal gas constant and T is the particle temperature. Herein, as reported in past kinetic Monte-Carlo simulations for Al NP surface oxidations,[14] the disparate values of the pre-exponential factors, α(m^2/s) and activation energy barriers, β(J/mol) for $O_2 \rightarrow$ Al diffusion ($\alpha = 1.72 \times 10^{-9}$ m^2/s; β= 69.5 J/mol) and $O_2 \rightarrow Al_2O_3$ diffusion (α= 2.8x10-3 m^2/s; β= 477.3 J/mol) can immediately explain the diffusion-limited retardation of metal oxidation reactions due to parasitic oxide shell formations. Furthermore, the lowered melting points of nano-Al also transition the solid-state grain boundary diffusion into the viscous diffusion regime. This plays an added role in altering the reaction kinetics in a step-wise fashion due to changes in the activation barrier during the process.

To this end, one can posit that kinetically trapped intermediate metastable metal-oxide (m-MO_x) phases, perched above the ground state equilibrium *en route* to their final stable oxide phases (see figure 1.2), can plausibly offer routes for instantaneous energy release (thermal/non-thermal) via structural bond rearrangements under external perturbations. Such molecular bond rearrangements can result in solid-state phase transitions to the lowest energy equilibrium states

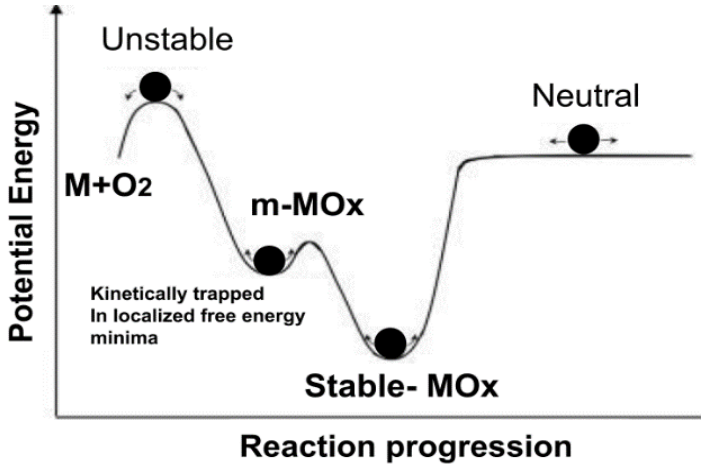

Figure 1.2) Schematic for reaction progression depicting the kinetic entrapment of m-MO_x phases

via direct nucleation/crystallization processes and hence need not rely on transport-dominated interfacial oxidation processes, thereby bypassing the diffusion limitations. In fact, solid-solid phase change materials (SS-PCMs) have received increasing interest for thermal energy storage because of their high energy-storage density. Specifically, inorganic SS-PCMs are able to store and release thermal energy in solid phase via various energy dissipation routes including crystallographic structure transformations (crystalline to crystalline), magnetic transformations, disorder-to-order transitions, as well as amorphous to crystalline structural transformations.[40-42] The usefulness of such SS-PCMs is highly dependent upon two parameters: 1) how large is the relative thermal energy release or storage and 2) what are the related kinetics for such release.[43] An example of this would be the well-studied diamond to graphite transition, with a tremendous amount of energy required for the perturbation and a relatively slow kinetics, thereby making it relatively unsuitable for use as a SS-PCM. However, our design concept here is the development of an SS-PCM with low perturbation energy or activation energy barrier and fast relative kinetics that can yet offer higher chemical stability under ambient conditions. This would allow for the safe long-term storage and instantaneous on-demand release of potentially large amounts of trapped energy either during a single metastable to stable transition or through reversible amorphous to crystalline transitions.[41] Such rearrangements do not require a catalyst or oxidizer as with most 1st-gen metalized ENMs. Without the need for external oxidizer mixes, metastable ENMs can achieve comparable energy release for substantially less overall weight, making for more efficient use in applications such as propellants where the overall weight due to dead loads is a major concern.

During Al oxidation, i.e., Al → stable α-Al_2O_3 transformation, one can conceive the formation of many intermediate Al-oxide structures/phases that can be kinetically trapped in localized free energy troughs in the non-equilibrium phase space. In fact, the emergence and stabilities of different AlO_x clusters/structures and their associated thermodynamic properties during the complex Al oxidation process to stable α-Al_2O_3 has been studied by previous atomistic and DFT-based computational studies (see figure 1.3 [44]); albeit, only a few of them have been experimentally realized to date, including the earliest anomalous observation of AlO_3 in vitreous SiO_2 stabilized by alkali or hydrogen compensators.[44-46] To this end, we have recently been able to successfully stabilize a form of metastable amorphous and hyper-oxidized Al-oxide NPs (a-AlO_x; $x > 1.5$) in our lab by using LASiS techniques. These unique a-AlO_x nanostructures notably stabilized in carbonaceous matrices have also indicated significant promise for their energetic activities via initial energetic tests carried out at the US Combat Capabilities Development Command's Army Research Lab (DEVCOM ARL, Aberdeen Proving Ground, MD). Details for

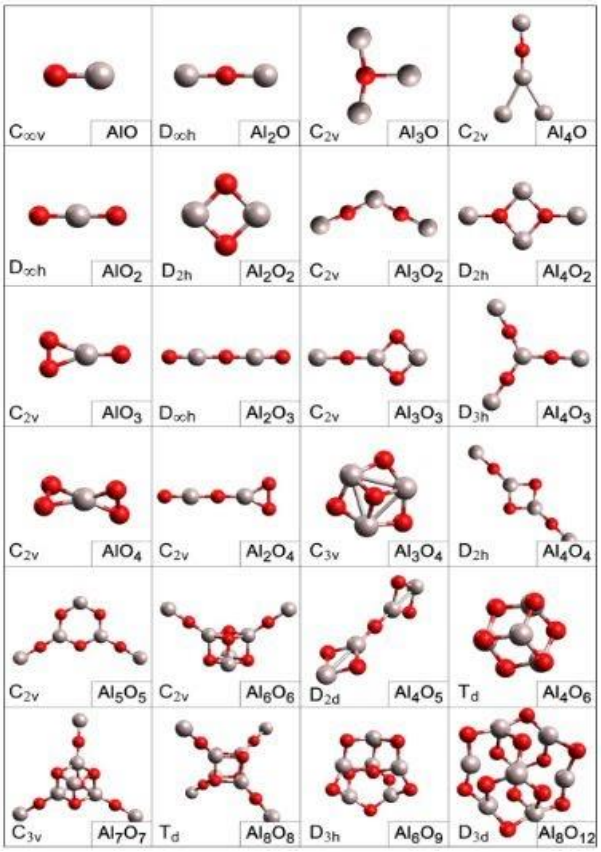

Figure 1.3) Most stable structures theoretically obtained from atomistic simulations (gray-Al, red-O) [44].

these preliminary results will be discussed later in section 3. Inspired by these preliminary results, the goal of this current study will be to investigate these as synthesized metastable a-AlO_x/C composite materials for their applications as next-generation m-ENMs as described earlier. Herein, our scientific quest is if these a-AlO_x NPs could exhibit the aforesaid instantaneous energy release during the transition of the metastable a-AlO_x structures to the stable equilibrium phase of α-Al_2O_3. As discussed earlier and indicated in figure 1.4,[44,45,47] depending upon the specific intermediate metastable AlO_x states, the energy release from such phase transitions can theoretically be up to roughly ~2 eV/atom or,192.98 kJ/mol. It needs to be mentioned that, based on the theoretical heats of formation, the theoretical energy release for the complete Al → α-Al_2O_3 transition during its oxidation is estimated to be ~3.4 eV/atom or 328 kJ/mol. However, the ensuing diffusion limitations arising from inevitable oxide shell formation during their storage hinders the net available moles of solid Al from undergoing a complete oxidation reaction, thereby impeding the full energy release from Al_2O_3 formation. Thus, our materials design concept here is that although the total energy release from Al → α–Al_2O_3 oxidation is larger than that for a-AlO_x → α-Al_2O_3 phase decomposition on a per mole basis, the effective moles of Al participating in the reaction is severely limited by the parasitic interfacial oxide formation when compared to the net moles of metastable a-AlO_x available for their direct solid-solid phase transitions. This could effectively result in higher energy release from the metastable-to-stable solid-solid phase transitions of a-AlO_x nanostructures shown in figure 1.4. Although the postulated mechanism could hold ground in overcoming the challenges of the 1st-gen ENMs, the PhD work will need significant fundamental understanding on: 1) tuning the relative kinetics of such solid-solid phase changes in the a-AlO_x-based m-ENMs by tailoring the sizes, volume loading, structure and compositions of these AlO_x nanostructures via optimal LASiS protocols, and 2) the mechanism for the kinetic entrapments and stabilization of these a-AlO_x NPs in the C-matrix. In light of these critical challenges as discussed above, the current study will throw light on the mechanistic underpinning for the kinetics and thermodynamics of such novel m-ENM designs along with the nature (microwave, laser, heat etc.) and amount of perturbation energy required to activate them.

To that end, this project will employ LASiS-driven techniques for non-equilibrium synthesis and tailoring of the synthesis-structure-property relations in diverse classes of m-MO_x/C NCs (M = Al, Mg, Cu, Fe) by tuning the laser and solvent-driven parameters and protocols for LASiS. Specifically, the study will significantly focus on a-AlO_x nanostructured materials used as the core example study to gain fundamental science knowledge on the broader classes of such materials.

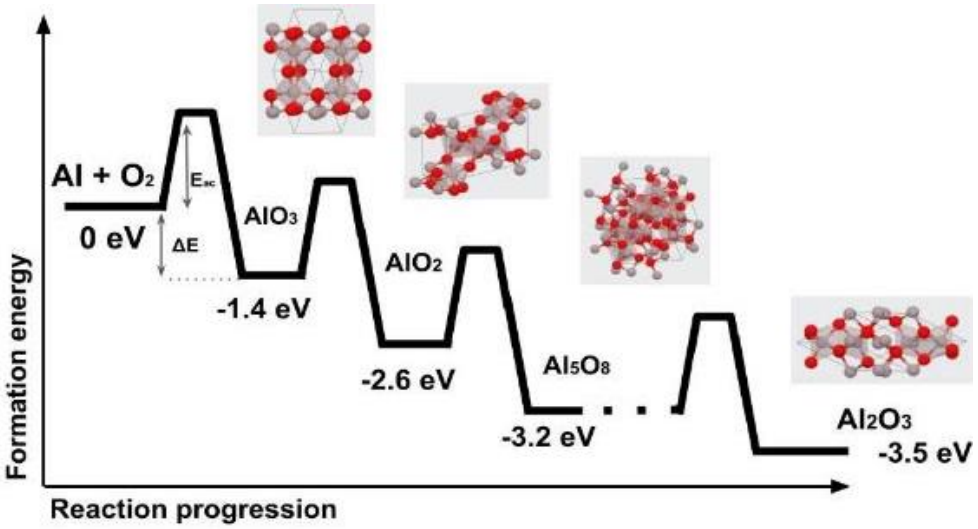

Figure 1.4) Reaction step processes for Al oxidation to stable equilibrium Al_2O_3 via predicted intermediate metastable states along with their respective theoretical formation energies.

LASiS can effectively, through laser-induced kinetic trapping, stabilize metastable states via rapid energy dumping and liquid-phase quenching. LASiS is in fact tunable with the final products being related to multiple synthesis parameters which will be discussed in detail in section 2.

The relative metastability for each sample as well as the determination of the sample's specific metastable state will be characterized using various analytical approaches including techniques such as high-resolution imaging via Transmission Electron Microscopy (TEM) structural analyses via Electron Energy Loss Spectroscopy (EELS) and X-ray photoelectron spectroscopy (XPS) that will be implemented as the two main analytical tools throughout the proposed work. Other techniques such as Fourier-Transform Infrared Spectroscopy (FTIR), Raman Spectroscopy, Inductively Coupled Plasma Optical Emission Spectrometry (ICP-OES), Laser-Induced Breakdown Spectroscopy (LIBS), and Solid-State Nuclear Magnetic Resonance (SS-NMR) will also be implemented, as and when necessary to characterize structural and compositional properties. All energetic characterizations are carried out off-campus in collaboration with the scientists from DEVCOM ARL (Aberdeen Proving Ground, MD) by using ARL's in-house developed and patented technique called Laser-induced Air Shock from Energetic Materials (LASEM). The detailed implementation of each of the characterization techniques to investigate the different structure-composition-property relations shall be discussed in later sections on project executables. However, when dealing with such a recently developing field as metastable nanomaterials, which do not have the convenience of roughly a hundred years of material science study to aid in classification, outside-the-box thinking and unique methods of problem solving is essential for the successful study of these revolutionary new materials.

1.3.2 Metal/ceramic-based nanocomposites as additives and solid fuels:

The scientific rationale behind this PhD research effort is that the proposed m-ENMs, synthesized via LASiS and discussed in the earlier section, will be added to solid fuels and tested as oxidizers/activators for more energy dense materials. Such solid fuels could possibly comprise: **1)** Metal carbide/oxycarbide NCs including Al-carbide and Fe-carbide based NCs; **2)** Carbon shell coated metal NPs including C shell coated Al cores (Al@C NCs), the latter being developed in our group in the past.[29] In our effort to design metal carbide/oxycarbide NCs as ENMs, the second effort directed in this research is toward the development of other Fe/Al-based ceramics (oxides/carbides/oxycarbides) that can: 1) be employed in typical 2-part energetic mixes as ceramic-based fuels; and 2) provide the advantages of the ceramic structures being activated via microwave frequencies due to their unique dielectric properties. Typically, composite ENMs

require two-part energetic mixes for rapid energy and heat release, with some of the more common examples being thermite or redox reactions and fuel oxidizer reactions. The thermite redox reaction between Al and Fe_2O_3 has been extensively studied throughout the past for decades due to its simplicity and high yield of heat release making it ideal for such applications as industrial metal welding, propulsion systems and ENMs at nanoscale.[48] In the case of the Al/Fe_2O_3 thermite redox reaction, the following reaction takes place (EQ1):

$$\mathbf{2Al + Fe_2O_3 => Al_2O_3 + 2Fe} \qquad \mathbf{EQ1}$$

Herein, Al acts as the reducing agent with a standard redox potential of $E°_{Al^{3+}/Al}$ = −1.662 V (vs. SHE), thereby undergoing oxidation and losing electrons wherein the oxidation number goes up, while Fe_2O_3 is the oxidizing agent (standard redox potential of $E°_{Fe^{3+}/Fe}$ = + 0.77 V), thereby gaining electrons with reduction in its oxidation number. This process is highly energetically favorable and exothermic in nature. The energy density and detonation velocity for such ENMs reactions are highly dependent upon the material's fuel density as well as their fuel to oxidizer interface distance.[6,49] As discussed earlier, naturally forming oxide shells can take up a large volume of the fuels over all payload while also slowing the necessary transfer of oxygen to the fuel metal via diminishing diffusion speeds as the shell thickness increases. It is for this reason that the design of materials that are both ultra-small and coated by some form of protective shell can both reduce the reaction distance as well as prolong the air-stability of these propellants that is vital for successful implementation of such ENMs. Another method of prolonged heat release is the use of more energy dense Al and Fe carbide NCs. This can also circumvent the problem of rapid surface oxidation of pure metal fuels owing to the higher thermal stability of metal carbides, while storing relatively high energy densities that can be released upon suitable activation to oxidize them to their most stable oxide structures. Metal carbides provide highly energy density for energetic materials, while being capable of expelling large amounts of prolonged heat during reaction.

As an example, one can immediately notice in Table 1.1 the energetic properties (enthalpy of combustion, $DH_{Comb}°$, J/mol-K) and relatively high energy densities (E_p, kJ/kg) of Al_4C_3, as compared to pure metallic Al. For this study we chose to focus on two separate metal-based carbide systems, Al-carbide and Fe-carbide, for which we will discuss the synthesis and detailed analysis in a later section. When ignited, the Al carbide and Fe carbide undergo the following reactions:

$$\mathbf{Al_4C_3 + 6O => 2Al_2O_3 + 3C} \qquad \mathbf{EQ2}$$

$$\mathbf{2Fe_3C + 9O => 3Fe_2O_3} \qquad \mathbf{EQ3}$$

Table 1.1) Thermochemical properties of Al and Al-carbide

	M.P. (°C)	C_p (J/mol-K)	$\Delta H°_{comb}$ (kJ mol^{-1} Al^{-1})	Ep (kJ/g)	n_{gas} (mol)
Al(Metal)	660	24.2	837.5	31.00	0
Al_4C_3 (Ceramic)	2650	116.0	1078.3	30.16	3

In both cases, although the heat release during reaction is high, the energy required to initiate said heat release is also quite high with the melting point being somewhere on the order of 2 to 4 times that of the standard Al based ENM (see table 1.1 for Al_4C_3 properties). Bearing this in mind, a significant disadvantage in using these energy dense and relatively air-stable metal-based carbides as ENMs resides in their relatively high ignition temperatures. In this way, if we could synthesize an ENM activator which could also provide the necessary oxygen for the metal-based carbide reactions, it would in theory solve the aforesaid problems by lowering the activation energies of their reactions. By implementing a kinetically-trapped intermediate metastable metal-oxide (m-MO_x) phase, with excess of trapped oxygen, as an activator/oxidizer additive in the metal/ceramic systems, one could possibly designing a composite fuel-activator/oxidizer mix. This would eliminate the excess parasitic weight of the oxidizer required for conventional fuel plus oxidizer mixes. In the constantly evolving area of rocket payload development, the need for such low-volume solid propellants with higher energy densities has increasingly gained prominence in the race to develop more technologically advanced rocket propulsion delivery systems for US' defense missions.

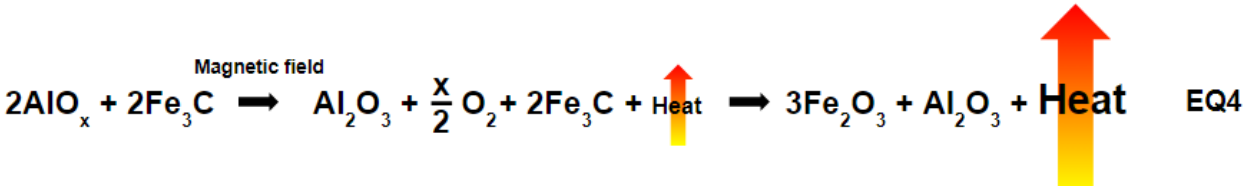

EQ4

Furthermore, it should be noted here that metal-carbides are known to have high dielectric and magnetic properties even in their amorphous forms. At the nanoscale, confined electronic interactions in magnetic materials also lead to unique size/morphology-dependent properties such as superparamagnetism.[50,51] Thus, metal-carbides nanomaterials are alluring for use as magnetic material due to certain complementary characteristics, including high melting points and chemical stability, along with high saturation magnetization (~140 emu/g), dielectric constants, and strong corrosion/oxidation resistance. By introducing the metal-carbides to an alternating magnetic field, just enough energy could be supplied to start a chain reaction starting with the ignition of the kinetically-trapped intermediate metastable metal-oxide (m-MO_x) phase resulting in the release of heat and oxygen which would in turn initiate the metal-carbide reaction. This can be seen in the reaction equation above, using AlO_x and Fe_3C as case studies (EQ4). When combined, the result could be a lowered activation energy and the elimination of the need for an additional oxidizer material thereby lowering the volume of solid propellants and delivering a

higher energy density material for advanced rocket propulsion delivery systems. The energy release could also, in theory, be tunable for more specific implementation via alteration of the m-MO_x additive and through different additive in the metal/ceramic systems mixtures. The methods, hypothesis and objectives for the research discussed in this thesis are outlined in the following section. The material analysis and initial results on the laser-induced trapping of these metastable and amorphous AlO_x/C ($2.5< x \leq 3.5$) nanocomposites is discussed in chapter 3. Investigations into tuning the reaction kinetics and tailoring the AlO_x/C compositions (x=O/Al) as well as structure (Crystallinity) is discussed in chapter 4. Further application of the LASiS technique for the synthesis and structure-composition characterizations of other Fe and Al-based oxides/carbides/oxy-carbides is discussed in chapter 5. Finally, the summary of this thesis and possible avenues for future research related to this work is presented in chapter 6 below.

Chapter 2: Research Methods and Objectives

2.1 Laser Ablation Synthesis in Solution (LASiS): An overview:

LASiS has recently emerged as a high-energy non-equilibrium route for facile colloidal synthesis technique for a plethora of unique metal/metal-oxide NPs, including amorphous metal NPs.[52] To this end, our group has recently developed and demonstrated the versatility of a specific class of reactive LASiS technique termed as Laser Ablation Synthesis in Solution-Galvanic Replacement Reaction (LASiS-GRR) *(Pat.: US 10,326,146 B2 (2019); Div. Pat.: 11,127,956 B2 (2021))*[53,54] that interfaces laser ablation under solutions with desired solution-phase reaction chemistry to synthesize disparate functional composite nanomaterials. Specifically, our group has employed LASiS-GRR in the past to synthesize a diverse library of functional nanomaterials for electrocatalytic, supercapacitive, and energetic applications that include: morphologically tailored CoO_x NPs[55] , Pt-Co-Cu-based tertiary and binary nanoalloys/nanocomposites[55-59], hybrid GO-interfaced MO_x NCs[60], graphitic shell coated Al NPs[29] and Metal-organic framework (MOFs) and MOF-derived MO_x hybrid- NCs[61,62] for use as superior electrocatalysis as well as high energy density nano energetics for use as solid propellants. But the long-postulated notion of highly non-equilibrium LASiS processes promoting laser-induced kinetic trapping of metastable states has rarely seen its experimental realization except for a few sparse reports to date.[39,63,64] The commonly postulated hypothesis here is that the highly non-equilibrium LASiS processes promote laser-induced kinetic trapping of metastable states, via rapid energy dumping and liquid-phase quenching. Specifically, LASiS involves the thermal vaporization of liquid-confined metal targets with high-energy laser to create plasma plumes with extremely high temperatures (~4000-5000 K) and pressures (~10-15 GPa) [65] that, in turn, produce charge-stabilized seeding NPs within a cavitation bubble.[66] The seeding NPs undergo ultrafast collisional quenching and subsequent interfacial interactions with by-products (graphitic/amorphous C nanostructures) from laser pyrolysis of organic solvents and/or other solvent chemistries at the bubble-liquid interface (figure 2.1).[67] Here the scientific rationale is that thermodynamics of composite phase formations, although rate-limited by the nucleating seeding NPs from LASiS, is finally rate-controlled by the organic

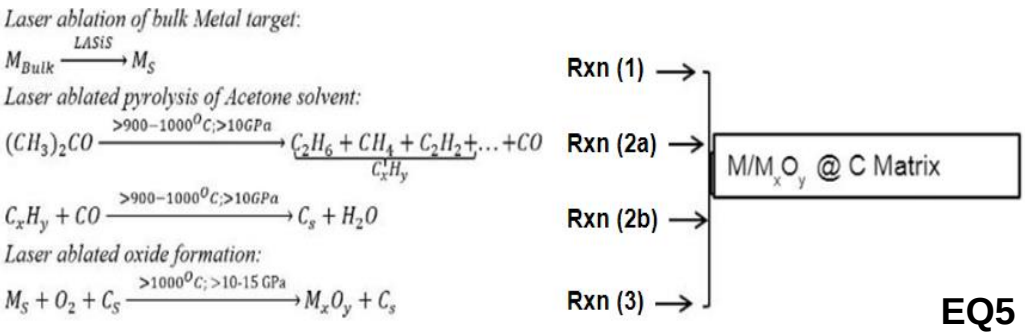

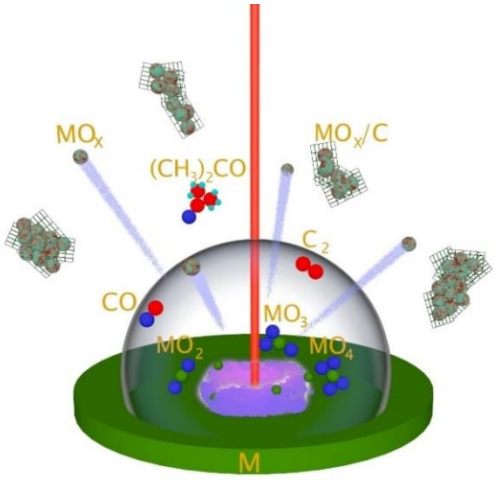

Figure 2.1) LASiS schematic showing plasma processes (target ablation, solvent pyrolysis) in cavitation bubble.

solvent chemistry that can be broadly described by the two most dominant and yet, competing reaction pathways:[59]

The aforementioned **Rxns. 1 - 3** in equation 5 (EQ5) depict the simplistic dominating rate controlling steps during the LASiS process. The detailed phase and structure evolutions during the highly non-equilibrium reaction mechanisms involved in the laser-induced plasma processes however, are far more complex. In fact, there could be many intermediate competing radical reactions beyond the above reactions through which the system can proceed to form kinetically trapped metastable states between metal oxide (MO_x)@C matrix interfaces that could potentially play critical roles in tailoring the energetic behavior of these composite ENM NPs in detonation-deflagration transition regimes. To this end, a fundamental understanding of these processes itself becomes one of the cornerstones of our investigations in the proposed work. The tunable process parameters for LASiS are:[59,68-70] **1)** Laser wavelengths (1064 and 532 nm) and energies (~70-330 mJ/pulse); **2)** Secondary solution-phase reactions to control reaction rates; **4)** Metal targets with desired high energy density; and **5)** Suitable solvents (aqueous, organic or cryogenic) to tailor desired interfacial solvent chemistry (pyrolysis, phase transformations etc.)

2.2 Characterizations Techniques:

Post-ablation, the samples are centrifuged, decanted and dried under vacuum to collect the solid powdered materials to carry out all subsequent material characterizations. X-ray diffraction study (XRD) and high-temperature XRD (HTXRD) were carried out on an Empyrean X-Ray diffractometer operating on a Cu radiation source. The HTXRD study was carried out on a Malvern PANalytical Empyrean X-ray diffractometer with Cu radiation and a PIXcel detector. High temperature X-ray diffraction (HTXRD) data were collected using an Anton Paar HTK1200N environmental chamber. The PDF analysis was carried out using the HighScore data analytics packages which were later verified using PDFgui and the data was gathered using an Ag radiation source. All transmission electron microscopy (TEM) imaging coupled with electron energy loss spectroscopy (EELS) measurements were carried out on a Zeiss Libra 200 MC Electron Microscope operating at 200 keV. Aberration-corrected high-resolution TEM (AC-HRTEM) imaging was conducted using a 200 keV beamline at the Argonne National Laboratory's (ANL) Center for Nanoscale Materials (CNM).

The in-situ heating S/TEM measurements were conducted using a 200 keV beamline at the Center for Nanophase Materials Sciences at Oak Ridge National Laboratory (ORNL). Thermogravimetric analyses (TGA) coupled with mass spectrometry (MS) for gas speciation

studies were carried out using a TA Discovery TGA-MS with a temperature ramp rate of 10^{o}C/min. Solid-state nuclear magnetic resonance (SS-NMR) was conducted on a solid-state Varian INOVA operating at 400 MHz. X-ray photoelectron spectroscopy (XPS) data was collected using a monochromatic X-ray source producing 1486.6 eV and a Phoibos 150 spectrometer. Differential Scanning Calorimetry (DSC) was gathered a TA DSA with a temperature ramp rate of 10^{o}C/min. For Mössbauer spectroscopy, all measurements are performed at room temperature under constant acceleration mode in transmission geometry in zero external field and in 1 T field with a 50 mCi ^{57}Co in Rh source. Aforesaid energy release from the solid-solid phase transition processes discussed earlier in chapter 1 is validated with energetic activity and stability tests from the laser excitation of the AlO_x/C NC samples carried out via LASEM (shown in figure 2.2*,* US Patent No. 9,551,692 (2017)) measurements at DEVCOM ARL(Aberdeen Proving Ground, MD); higher laser-induced shock velocities indicate increased energy release on the microsecond timescale relevant for increasing detonation performance.[71,72]

2.3 Research Objectives:

The objectives of this dissertation are to investigate the following:

Objective 1: Design and synthesis of carbon-stabilized metastable metal oxide (m-MO_x/C) NCs as advanced m-ENMs via LASiS for solid propellant activator/oxidizer.

Objective 2: Detailed material characterizations to establish synthesis-structure-functionality relations for the m-MO_x/C NCs and gain mechanistic insights into tuning LASiS protocols for tailoring their energetic properties and stabilization mechanisms.

Specifically, this study will focus on tailoring LASiS-directed entrapment of metastable Al-oxide phases, for use as activator/oxidizer as well as possible metal/metal carbide for advanced propellant systems.

2.4 Research Hypotheses:

Hypothesis 1: Non-equilibrium plasma dynamics in LASiS will enable kinetic entrapment and stabilization of m-MO_x/C NCs that can undergo instantaneous energy release via solid-solid phase transition between locally equilibrated metastable states and final equilibrium products. This will enable the bypassing of diffusion-limited oxidations in first generation metallized ENMs.
Test for hypothesis: By using LASEM we can establish a comparison for our ENMs compared to standard ENMs enabling us to determine their relative reactivity. HTXRD can be used to plot out the kinetics of the reactions during transition to the more stable phases. By studying and testing

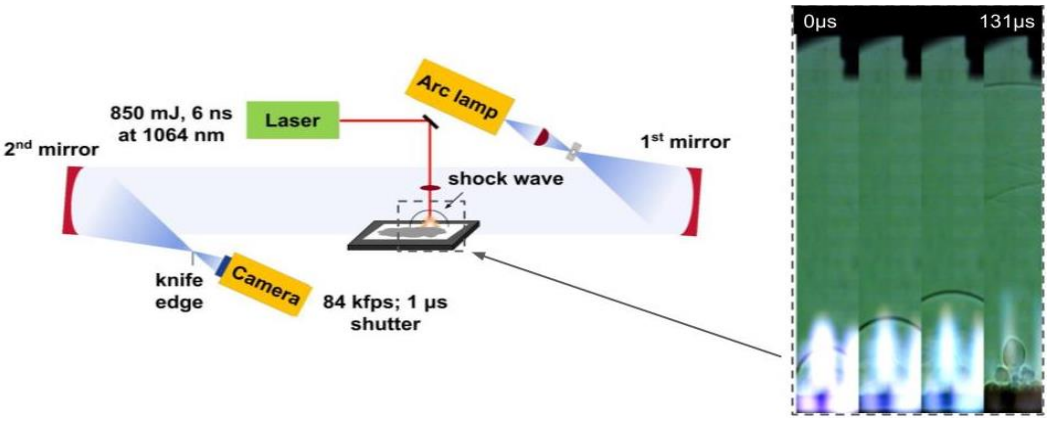

Figure 2.2) LASEM schematic showing captured schlieren image for a representative ENM

the materials before and after a long period of time we can determine whether oxide shells form and/or affect the reaction.

Hypothesis 2: Thermodynamics and kinetics of phase transition-driven energy release from MO_x structures phases can be tuned by tailoring sizes, structures (amorphous/crystalline), compositions, and specific metastable phases of the m-MO_x NPs and the pyrolyzed-C contents via optimally controlled laser and solvent parameters for LASiS protocols.

Test for hypothesis: 1) By tuning various LASiS parameters (l*aser energy, wavelengths, frequency, ablation time, pulse width along with choice of solvents, and solvent temperatures*), variations in synthesis-structure-composition properties and metastability in ensuing m-MO_x NPs can be investigated; 2) By using EELS, XPS and SSNMR, instability and non-standard spectrums can be analyzed to determine non-stoichiometric metastability.

Chapter 3: Laser-Induced Trapping of Metastable Amorphous-AlO_x/C ($2.5 < x \leqslant 3.5$) Nanocomposites: Implications for Use as Solid Phase Gas Generators

Disclosure:

This chapter is adopted from a manuscript published in ACS Applied Nanomaterials 2023 (V6.13 P10977-10985) and Journal of DoD Research & Engineering [LIMITED DISTRIBUTION MATERIAL] 2022. The full list of authors includes: Elijah Davis, Gerd Duscher, Jianguo Wen, Dibyendu Mukherjee, and Jennifer Gottfried. The role of Elijah Davis was to design and perform all experiments, process and analyze all data, and prepare the manuscript for submission.

3.1 Introduction:

A rapidly evolving landscape for complex human-technology interfaces in modern society have generated an unprecedented demand for new and exotic materials. Such additions to the current materials library can advance disparate technological frontiers, ranging from battery technology and memory storage devices to the burgeoning space missions and automotive industries. The diverse polymorphic phases of metastable nanostructured materials made from earth-abundant metals could hold the key to future engineering of economically viable exotic materials. This is due to the combination of their unique properties arising from kinetic entrapments of molecular structures in non-equilibrium phase spaces, and structure-functionality relations arising from nanoscale size effects. Amongst the known earth-abundant elements, Al is the most abundant metal (~8% by wt.) in the earth's crust that can be extracted without deep mining and finds widespread use in human goods and consumptions; yet, only ~35% of Al from consumer goods is recycled currently in the US.

Specifically, amorphous m-MO_x nanostructures can quickly emerge as potential game-changing materials with their properties and applications being investigated and understood only in the past few years.[73-75] The appeal for such materials arises from their long-range disordered structures comprising high concentrations of coordinately unsaturated constituent atoms that can trap considerable bond strain energies. This can manifest in atypical mechanical, energy storage/dissipation and optoelectronic properties, and pave the path for a plethora of applications where solid-state amorphous-crystalline phase change materials can prove to be highly beneficial. As pivotal as metastable nanomaterials promise to be, their accelerated design paradigms are limited by imprecise predictions for their synthesizability. Such limitations arise from inaccurate theoretical predictions of the thermodynamic and kinetic functions for non-equilibrium phase transitions in currently employed synthesis routes. Added to this is the lack of rational experimental designs to enable kinetic freezing of metastable nanophases *en route* to

their ground-state equilibrium phase. To this end, recent computational works harnessing data mining and supercomputing capabilities are working to predict the thermodynamic limits for the synthesis and stabilization of metastable materials.[9,76] However, experimentally viable non-equilibrium syntheses remain elusive with a few employing ultra-fast quenching, physical/chemical deposition, high-pressure compression, and mechanical attrition techniques.[77,78] A handful of amorphous m-MO_x nanostructures have also been synthesized via low-energy/low-temperature plasma routes, that include recently observed amorphous Al-oxide NPs from capacitively-coupled plasmas.[38] While such efforts are commendable, simple yet efficient synthesis of amorphous m-MO_x NPs stabilized in suitable media/matrices with high purity and yield continue to pose an immense challenge; this has deterred their detailed processing-structure-property characterizations and interfacing with advanced nano-manufacturing platforms.

High-energy LASiS has recently emerged as a powerful and facile colloidal synthesis route for diverse unique metal/metal-oxide NPs, including amorphous metal NPs.[52] Our group has successfully demonstrated LASiS, interfaced with solution chemistry (US Pat.: 10326146/11127956), as a versatile tool for synthesizing disparate functional MO_x and intermetallic/composite nanomaterials.[55,56,58,59,61] However, few works to date have experimentally demonstrated the long-postulated ability of non-equilibrium LASiS process to promote laser-induced kinetic trapping of metastable molecular structures, via rapid energy dumping and liquid-phase quenching.[39,52,63,79] To that end, we report here the use of LASiS for synthesizing a highly disordered, metastable nanocomposite (NC) of hyper-oxidized a-AlO_x NPs stabilized in pyrolyzed-C (a-AlO_x/C NCs). We present detailed physicochemical characterizations for the a-AlO_x/C NCs that can provide future guidelines for metastable nanomaterials analyses. Our results reveal unique stability for these NCs under ambient conditions, while undergoing thermally-activated solid-solid phase transformation from a-AlO_x to crystalline α-Al_2O_3 phase and releasing excess trapped gases (O_2, CO_2). To our knowledge, only a handful of studies till now have reported on the stabilization of such unusual Al-oxide phases under ambient conditions, with the earliest being a rare report on unique observations of AlO_3^- structures stabilized in bulk materials by vitreous SiO_2 and alkali charge compensators.[38,46]

3.2 Results and Discussions: Structure-function characterizations:

Recent preliminary studies for the proposed project indicate highly promising results for the first-ever synthesis and stabilization of metastable a-AlO_x/C NCs via LASiS, that has been heretofore inconceivable by conventional equilibrium chemical synthesis routes.

Our earlier work on the synthesis of graphitic-shell coated Al NPs[29] using the experimental set-up in figure 2.1 (details in section 4 below) motivated the current investigations into the unique emergence of Al-oxide nanostructures in the background carbon matrix. Specifically, it was observed that ultra-small amorphous structures emerged out of low-fluence (~1.0 -1.2 W) laser ablation of pure Al targets under acetone. Size and morphology of these a-AlO_x NPs in carbon matrix composites (a-AlO_x/C NCs) analyzed via high-resolution transmission electron microscopy (HRTEM) imaging (figure 3.1a), indicate AlO_x particle diameters to vary between 3-20 nm with the majority of them residing in less than 10 nm size ranges (figure 3.1b), and a negligible amount of large crystalline NPs in the ~50 - 200 nm size range. Detailed selected area electron diffraction (SAED) analysis (bottom inset in figure 3.1a) confirm that the small particles (<15 nm) are largely amorphous, while the larger particles (>70 nm) are mostly crystalline. Bulk X-ray powder diffraction (XRD) peak analysis, using an internal standard method, indicate an approximate percentage crystallinity of ~2.4 % wt. that mostly coincide with pure crystalline Al of ~70 nm crystallite sizes.[80,81]

The negligible percentage of crystalline Al NPs puts the focus of this article on a detailed investigation into the predominantly smaller amorphous AlO_x NPs. To that end, localized TEM-coupled electron energy loss spectroscopy (EELS) mapping and analyses (figure 3.2a) were carried out on these smaller a-AlO_x NPs to provide a better understanding of their individual elemental compositions. Specifically, the Al-L_{23} edge EEL spectrum from a representative AlO_x NP, as shown in the corresponding Al at. % distribution image in figure 3.2a, reveals a unique and distinct spectral profile when compared to the standard spectrum for α-Al_2O_3 samples. Previous articles have referred to such specific spectral peak arrangements as originating from a highly amorphous-Al_2O_3 or, in most cases, AlO_x of unknown stoichiometry.[82-84] Hence, the unique EELS profile plausibly emerges from metastable oxide states trapped in laser-induced free-energy minima during the transition of Al to their stable oxide forms. . Furthermore, the near edge structure of the O-K edge EEL spectrum corresponding to the O (at. %) distribution mapping, when compared to the EELS profile for α-Al_2O_3, also supports our hypothesis on the existence of non-stoichiometric amorphous Al-oxide structures.[82,83] Based on these EELS analyses, we posit that the NPs in question are composed of highly disorganized and amorphous metastable oxides of Al. Although we used the standard EELS spectra for α-Al_2O_3 as the reference here, we also confirmed that the standard spectra for most other stable polymorphs of Al_2O_3 such as γ-Al_2O_3, θ-Al_2O_3 and $Al(OH)_3$ were distinctly different from those reported here for the AlO_x NPs .[82,83,85-87]

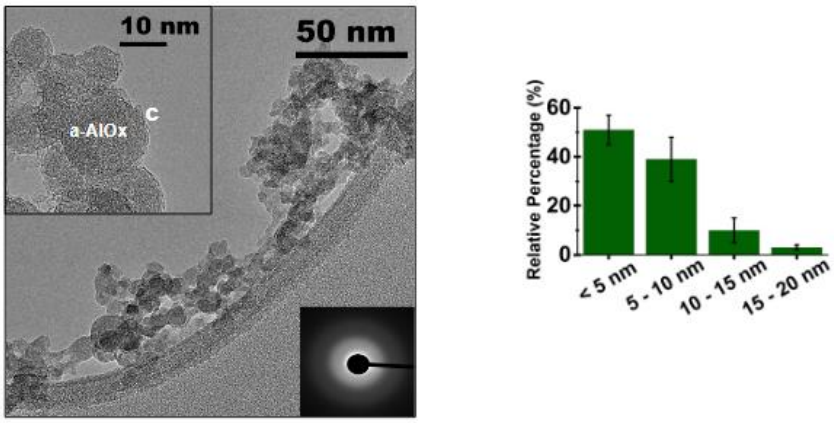

Figure 3.1) Synthesized AlO_X/C NPs. **a)** HRTEM image of AlO_X/C NPs with amorphous SAED (bottom); **b)** Size distribution for AlO_X/C NPs showing an average size between 5-10nm.

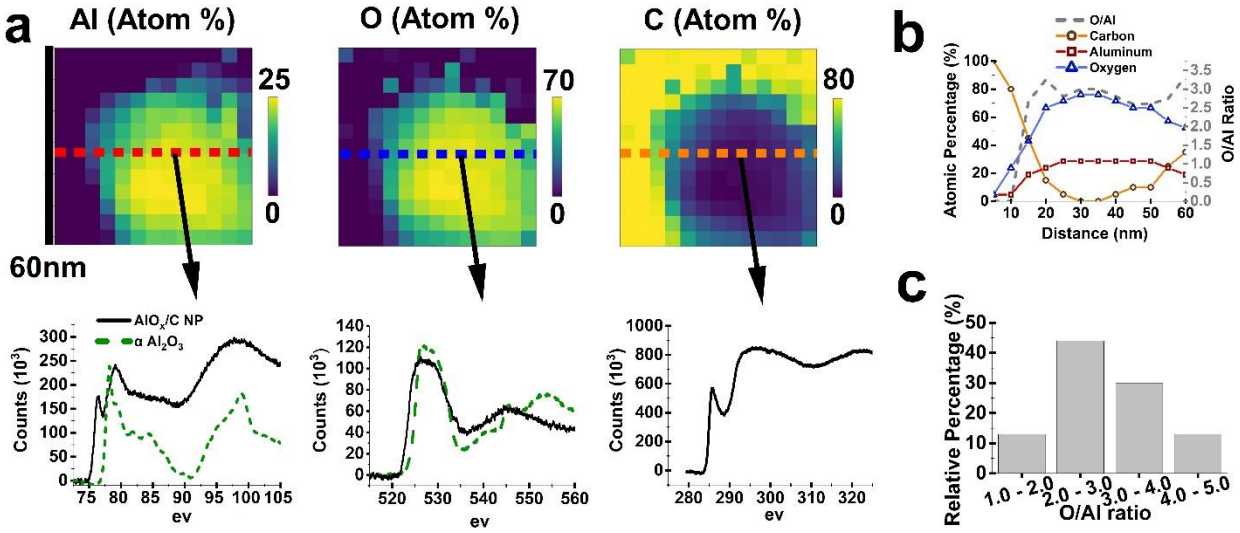

Figure 3.2) Compositional characterization of AlO_X/C NPs. **a)** Atomic percentage distributions (Top) for selected NP suspended in vacuum indicating ~ 70 at. % O, ~ 25 at. % Al, and <5 at. % C in the representative NP core area along with corresponding EELS Al-L_{23}, O-K, and C-K edge spectra (Bottom); **b)** Atomic distribution across EELS mapping of selected particle for corresponding atomic species of Al (Red), O (Blue) and C (Orange) as marked by respective colored lines (Top a); **c)** Statistical EELS analysis of randomly selected particles throughout the sample displaying their respective O/Al ratio with the bulk of their ratios falling between either 2.0-3.0(~42 %) or ~3.0-4.0 (~30 %).

The carbon matrix surrounding the AlO_x NPs is investigated via the C-K edge EEL spectrum in figure 3.2a, corresponding to the C (at. %) distribution around the from our NPs. It is noted that the spectrum does not match the standard graphitic-C ELNES and indicate the presence of amorphous carbon largely around the interfacial edges of the NP. Previous reports have identified similar EEL spectrum for amorphous and hydrogenated carbon in thin film studies arising from pyrolyzed organic solvents.[88,89] Detailed EELS mappings in figure 3.2a & b indicate elemental atomic percentages of ~70 at. % O and only ~25-30 at. % Al along with C comprising a negligible <5 at. % at the inner core of the AlO_x NPs. Corresponding cross-sectional atomic distributions of Al (red line), O (blue line) and C (orange line), as marked in figure 3.2a, are plotted in figure 3.2b, for the representative NP. Upon inspection, the estimated O:Al atomic ratios (gray dashed line) is found to vary between ~2.5 - 3.5 which is atypical of the stoichiometric O:Al atomic ratio of 1.5 for Al_2O_3, thereby substantiating our earlier postulation on the hyper-oxidized states of Al. Furthermore, the analyses indicate large distribution of O atoms (~65-70 at. %) inside the NP and the absence of any localized surface O, typically observed on pure Al NPs due to surface oxidations. In contrast, the small amounts of core C (<5 % at.) with the large distribution of interfacial C along the particle edge, as seen from figure 3.2a & b, point toward the possible role of C matrix in stabilizing these disordered and metastable AlO_x NPs, as also reported in recent works.[90]

Finally, based on previously developed EELS techniques for elemental quantification in amorphous nanomaterials,[91] statistical EELS data analyses were carried out over several (~23 NPs) a-AlO_x NPs in the composite samples (shown in figure 3.2c). The results indicate that the net O/Al ratios from the majority of the NPs were distributed either between ~2-3 (~42 %) or ~3-4 (~30 %). The existence of such hyperoxidized AlO_x structures above that of even x = 3 might not be implausible with recent theoretical DFT studies indicating negative formation energies for AlO_2, AlO_3 and even AlO_4 clusters that systemically decrease with increasing cluster sizes.[35] This, in turn, can explain the formation and stabilization of such unusual Al-oxide clusters in localized free energy minima while hovering above the lowest formation energy for α-Al_2O_3 crystals. The relatively small percentage (~10%) of O:Al ratio between ~1-2 is attributed to the presence of small amounts of amorphous Al_2O_3 (O:Al = 1.5), added to the contributions from the oxide shell formation on the minor percentage (<3-4 w%) of crystalline Al particles as revealed from the room temperature XRD data. The distributions of O:Al > 4 arising in figure 3.2c could also plausibly be explained from the additional O atoms bonded to the C near the interfacial edges of the NPs. The average O/Al ratio over the AlO_x NP set analyzed here is estimated to be ~2.91 which leads to the proposed stoichiometry of AlO_3 for the AlO_x structures under investigation here.

The lack of substantial reports on nano-scale stabilization of unique thermodynamic phases of AlO_x posed a critical challenge for this work to establish known structure-composition characterizations for the metastable AlO_x/C NCs. To that end, figures 3.3-3.4 report a series of surface and bulk spectroscopic analyses of the as-synthesized NCs via X-ray photoelectron spectroscopy (XPS), and solid-state ^{27}Al nuclear magnetic resonance (SSNMR) spectroscopy. The ^{27}Al NMR data in figure 3.3 indicates a large percentage of hexagonal Al structures (AlO_6 coordination), which is common for most Al_2O_3 samples[92,93]. However, unlike most NMR results from Al_2O_3 samples, the AlO_x/C NCs here indicate a high percentage of pentagonal Al structures (AlO_5 coordination) which can be interpreted as a generalized measurement of the extent of disorders in the AlO_x structures[94,95]. On rare occasions where such AlO_5 coordination has been reported for γ-Al_2O_3 phases, the relative percentage of AlO_6 coordinated structures remain below 70%[93,96]. This, in turn, provides a qualitative proof for our NC samples being distinctly different from the known stable Al_2O_3 polymorphs. It should be noted here that the occurrence of an SSNMR spectrum, similar to the one observed from the AlO_x/C NCs in question, have been reported for very thin (< 10 nm) amorphous Al_2O_3 films produced from atomic layer depositions[93-95], wherein the unique distribution of AlO_6, AlO_5 and AlO_4 coordinated peaks were assigned to the measure of instability and transitional disorders as is the case for our AlO_x/C nanostructures.

Full-scan survey XPS data in figure 3.4a identifies the large Al(2p) and Al(2s) peaks along with the O(1s) peak and a relatively weak C(1s) peak.[97] The Al(2p) peak deconvolutions in figure 3.4b reveal large Al-O stretching (~79 %) at ~74.8 eV along with the absence of any Al-Al bonds (marked in yellow in figure 3.4b) that supports our previous claims of negligible amount of pure Al. The lack of Al-Al bond contributions in the XPS analyses, in spite of the relatively small percentage of Al (<3 % wt.) resolved from XRD analyses, can be explained based on the ~5-10 nm probing depths for XPS analyses. This works well for analyzing the large percentage of NPs in <10 nm size ranges. However, the negligible amounts of the larger crystalline Al NPs (~70 nm sizes) carry relatively thick Al_2O_3 shells. This shell will likely consume most of the XPS probe depth resulting in the small weight percentage of Al being undetectable via XPS. Additionally, a relatively small percentage contribution from Al_2O_3 residues (13 %) at ~73.5 eV and weakly adsorbed surface species (<8%) at >76.5 eV was also observed. As also reported in earlier XPS studies, the latter could arise from a number of species with the most common being from surface

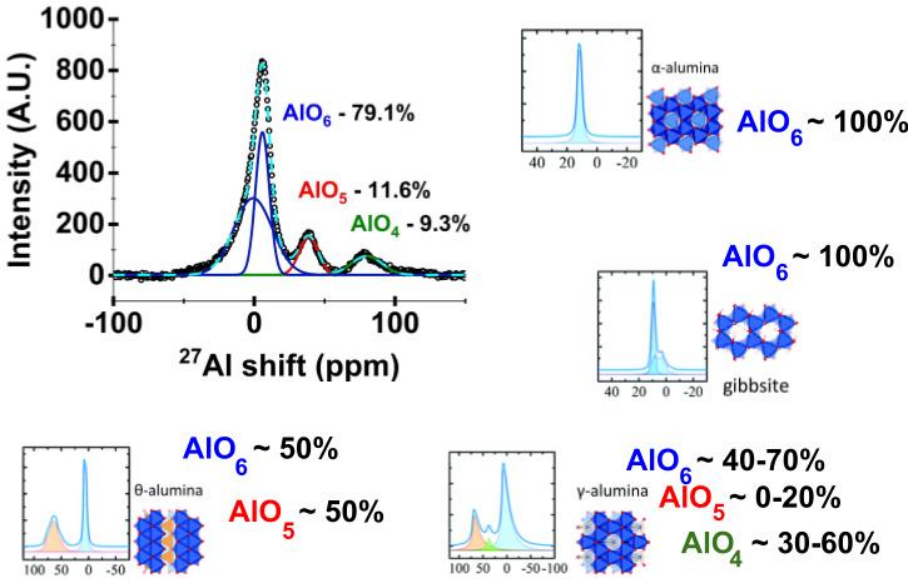

Figure 3.3) ^{27}Al NMR spectra with Al-O coordination percentages de-convoluted and compared to common alumina structures.

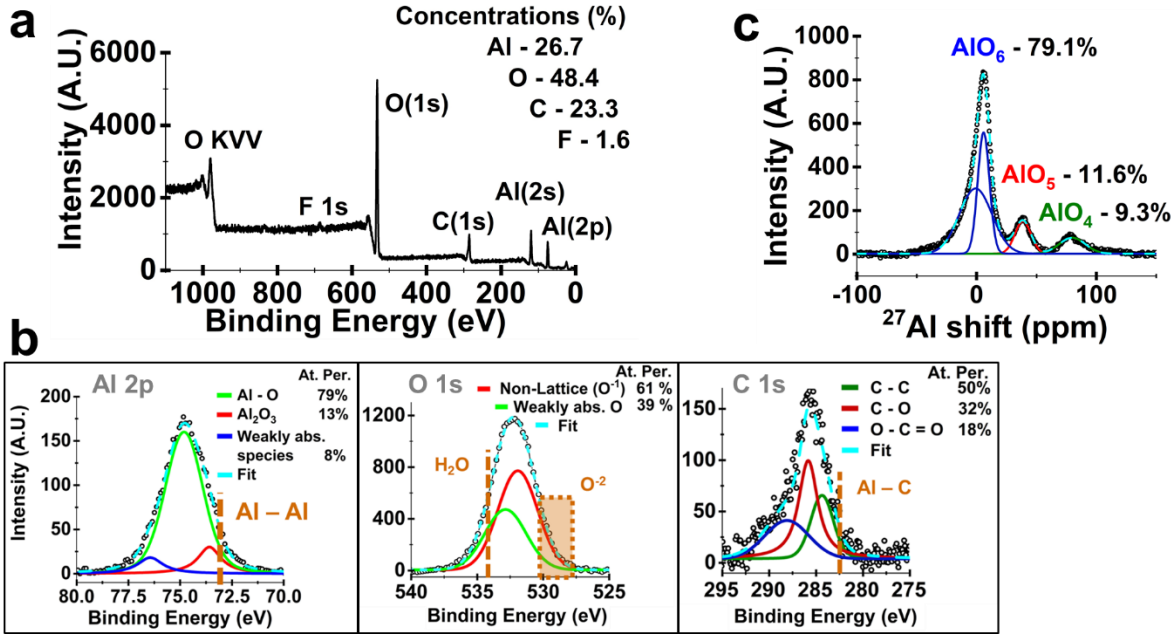

Figure 3.4) Structural characterization of AlO_X/C NCs via surface and bulk spectroscopic analyses. **a)** Full scan XPS survey indicating the contributing atomic concentrations of O (~48.4 at. %), Al (~26.7 at. %) and C (~23.3 at. %); **b)** Deconvoluted peak fits to high-resolution XPS spectra for Al 2p, O 1s and C1s peaks, with peak corresponding to adventitious carbon being shifted to 284.8 eV as a reference; **c)** ^{27}Al SSNMR for AlO_X/C NCs with the deconvoluted peak percentage distributions for AlO_6, AlO_5 and AlO_4 co-ordinations indicating large structural instability and disorder in the AlO_X NPs owing to the large percentage of AlO_5 coordination with respect to AlO_6 and AlO_4.

water absorption or Al-OH contributions from hydroxide groups.[98,99] Interestingly, the O(1s) peak fits reveal unusually high percentages (~61 %) of non-lattice oxygen species at ~532 eV and the near absence of the well-known lattice O^{2-} peaks in the 528.5-530.5 eV region.[100] The latter is known to typically arise from standard lattice-bound Al_2O_3 structures, where oxygen should be in -2 oxidation state. Previous XPS studies on metal oxide structures have attributed such non-lattice oxygen peaks plausibly to either oxygen vacancies or low coordinated O^- species[100-102] which would put the oxygen in -1 oxidation state, thereby corroborating our earlier predicted AlO_x structures (x~3.0) with Al in the +3 oxidation state. Moreover, the C(1s) peak position indicates the presence of both pyrolyzed and adventitious C, wherein the peak deconvolutions in figure 3.4b reveal the absence of any Al-C bonds at ~282.5-283 eV (marked in yellow in figure 3.4b), while allowing the identification of C-C (~50 at. %) at ~284.5 eV, C-O (~32 at. %) at ~286.5 eV and O-C=O (~18 at. %) at ~288 eV. Based on these observations and a previous study on carbonaceous layers on FeO_x surfaces, we posit here that the interfacial C matrix around the AlO_x NPs are plausibly bonded largely to the terminating O from the Al-O bonds.[103]

Quantitative elemental distributions from the XPS survey scan in figure 3.4a are estimated to be ~26.7 at. % Al, 48.4 at. % O, and 23.3 at. % C, respectively. Here it is noted that the broadened O(1s) peak centered at ~532.5 eV, enveloping both the non-lattice and weakly adsorbed oxygen peaks, makes it challenging to deconvolute the O atoms bonded to C or, associated with AlO_x and/or, any disordered Al_2O_3. Hence, after accounting for two (Al-O) bond contributions from each non-lattice Al_2O_3 molecule in the peak percentage for Al-O stretching, we estimate the O:Al ratio to be x~3.4. Within the margins of error, this value concurs well with our earlier EELS-based estimates for O/Al ratio in the ~2.5-3.5 range.

Related to the objective of characterizing of each material's structure was the detailed study on how these material's internal bonds are constructed. What is clear is that the outer surface is not encapsulated by an onion type formation of closed fullerene shell coating as with our previous work[29]. This leaves the question as to how the materials are able to resist oxidation without such a protective coating. The critical question here is whether the outer surface is terminated by oxygen which allow for further diffusion and finally oxidation or if the oxygen is terminated by carbon making the surface oxidation more difficult.

The current hypothesis is that the oxygen at the outer edge is in fact terminated by carbon; this may assist in the stabilization of these metastable materials. It has been shown through multiple DFT calculations that such metastable hyper-oxide nanostructures can be stabilized at nanoscale by diamond-like surfaces with interfacial C terminating oxygen coordination via M-O-

C bonds resulting in large negative electron-affinities (−2 to −3 eV).[90,104] These diamond-like surfaces can be visualized in figure 3.5, where the Al-O-C bonds are similar to what is believed to be seen in the XPS data for the synthesized AlO_x discussed earlier (Light grey – Al, red-O, and dark grey – C). It is our goal in this study to verify this assumption and if so, gain an experimental view of this stabilization process.

It has been found through detailed DFT calculations that interfacial metal-oxygen (M-O) bond arrangements terminating on diamond surfaces, a C-allotrope, can be significantly more stable than regular CO-M or, O-M at nanoscale.[104] This could support our postulated hypothesis that the interfacial pyrolyzed-C skin at the outermost particle surfaces terminates the exposed M-O bonds, thereby offering the general consensus on how the hyper-oxidized metastable MO_x NPs emanating from the high-energy LASiS processes are plausibly stabilized.

In order to gain a mechanistic insight into the role of interfacial structures driving the high -thermal stability (up to ~750-800^{o}C) in these metastable a-AlO_x/C NCs, sub-nm resolution aberration-corrected TEM (AC-HRTEM) image of the AlO_x/C interface is shown in figure 3.6c. The image immediately reveals a unique C monolayer skin (~0.4 nm thick) on the ultra-small (~5-15 nm) a-AlO_x NPs, as verified by the typical C-C lattice bond lengths of ~2.1-2.3 Å from atomic distance measurements (Inset in figure 3.6). Bearing in mind the high dissociation energies for diatomic covalent C-O (~11.2 eV) and C-C (~6 eV) bonds as compared to the ionic Al-O (~5 eV) bonds, the C skin bonded to the interfacial Al-O structures could plausibly explain the unusually enhanced stability of the ultra-small a-AlO_x NPs in the pyrolyzed C matrix. Such observations concur very well with recent DFT calculations for Al-oxide terminated diamond-like surfaces that reported on the stabilization of AlO_3 surfaces via Al-O-C bonds.[104] Such studies have indicated in the past that M-O-C bond arrangements are significantly more favorable than C-M terminations, especially when O is in the −1 oxidation state.[104,105] Hence, the studied AlO_x NPs here put forth an excellent experimental proof of such stabilization methods for metastable nanomaterials.

Direct solid-solid phase transition for the metastable a-AlO_x nanostructures into equilibrium crystalline α-Al_2O_3 NPs was investigated using high-temperature X-ray powder diffraction (HTXRD) measurements on the NCs (figure 3.7a). Temperature-dependent growth and evolution of the Al_2O_3 polymorphs (i.e., $\gamma/\theta-Al_2O_3$, $\alpha-Al_2O_3$) from the parent a-AlO_x phase are monitored via crystallite size growths (figure 3.7b) calculated from HTXRD data collected at 10^{o}C/min heating rate. Figure 3.7a indicates a negligible amount (<3-4 % wt.) of crystalline Al in the as-synthesized a-AlO_x/C NCs until ~650^{o}C, at which point the sample transforms into a purely amorphous phase that persists till about ~750-800^{o}C. Beyond ~750^{o}C, the first polymorphic

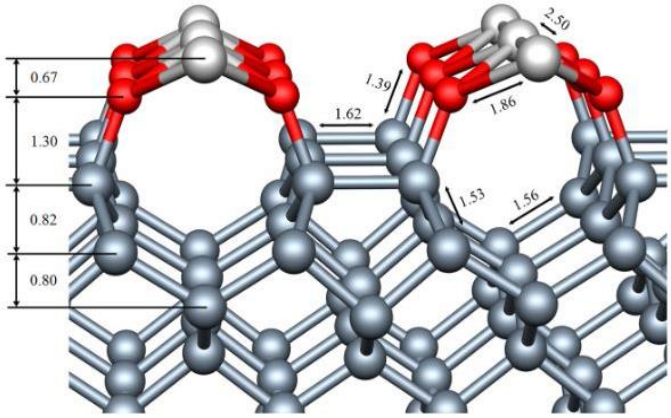

Figure 3.5) DFT calculations on the stabilization of AlO_2 via diamond-like carbon surfaces. Light grey – Al, red-O, and dark grey – C.

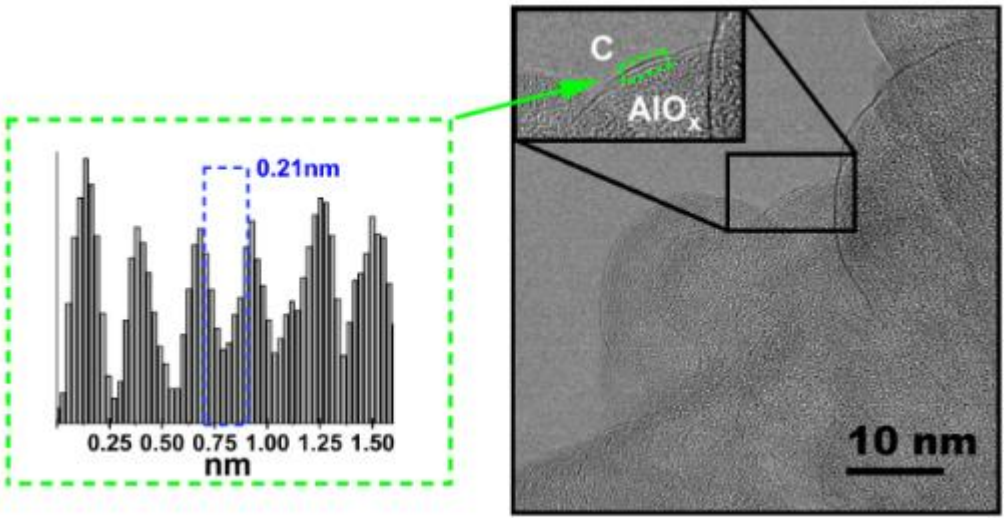

Figure 3.6) Sub-nm resolution aberration-corrected TEM (AC-HRTEM) image of the AlO_x/C interface showing a single monolayer of carbon at the outermost edge.

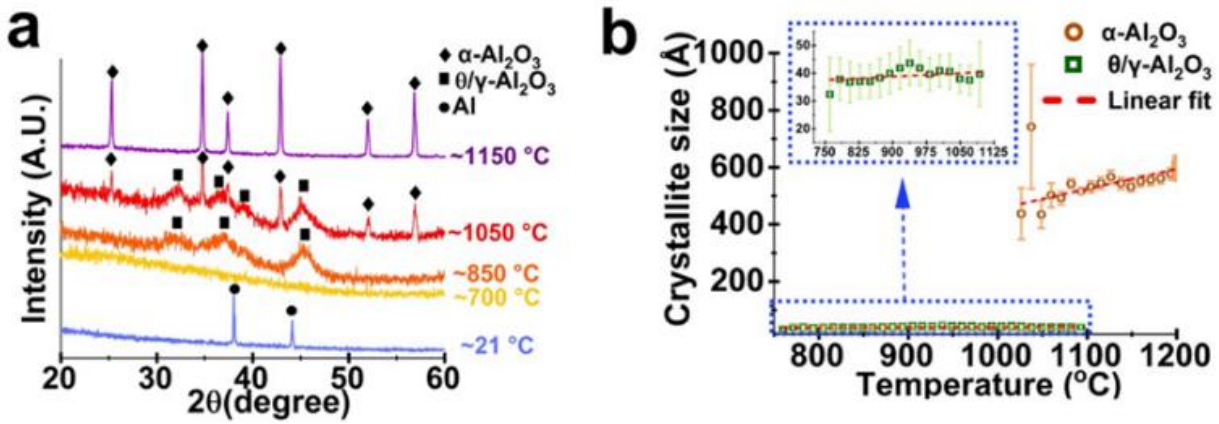

Figure 3.7) HTXRD characterizations along with crystallite growth studies for solid-solid phase transition of a-AlO_x → α-Al_2O_3 NPs indicating high stability of a-AlOx structures up to ~800-850°C; a) Temperature-dependent XRD analyses indicating transition from largely amorphous-AlOx to θ/γ-Al_2O_3 beyond ~800-850°C and finally, α-Al_2O_3 beyond ~1050-1100°C b) Crystallite size growth (Å) calculated from HTXRD data as a function of temperature.

crystalline phase of θ/γ-Al_2O_3 nucleates with a critical crystallite size of ~3.5 nm which undergoes steady growth until ~1100ºC (figure 3.7b inset). Subsequently, the clear emergence of α-Al_2O_3 peaks are observed between ~1050-1100ºC with a drastic jump in the crystallite sizes up to ~40-45 nm (figure 3.7b), wherein both crystalline α-Al_2O_3 and θ/γ-Al_2O_3 polymorphs co-exist. The final 100% crystallite weight conversion of α-Al_2O_3 is reached at ~1100ºC, after which the crystallites continue to coarsen well into ~60 nm. This also corroborates the recent findings on final decomposition products of similarly sized AlO_3 NPs at temperatures above ~1000°C.[38]

Combined thermogravimetric analyses-mass spectrometry (TGA-MS) measurements carried out to ~1000°C in inert N_2 atmosphere (see figure 3.8a) reveal the release of large amounts of trapped gases (CO_2, H_2O and O_2) during the solid-solid phase transition (4a-AlO_3 → 2α-Al_2O_3 + $3O_2$↑) studied by the HTXRD measurements earlier (figure 3.7a). Herein, the initial evaporation of the hydration layers between 0-200 °C is followed by both CO_2 and H_2O emissions between ~200 - 500°C from the decomposition of the pyrolyzed C matrices. Finally, a continued and uniform release of O_2 along with a relatively large spike in the CO_2 emissions is observed between ~800-1000°C of the burn region. This provides a crucial mechanistic understanding of the large O_2 release from the aforesaid instantaneous solid-solid phase transitions, prompted by the thermal decomposition of interfacial stabilizing C skins leading to the simultaneous release of the excess CO_2. Subsequent HRTEM examination of the final TGA burn byproducts in figure 3.8b (Inset for SAED patterns) indicates the final products to be highly crystalline α-Al_2O_3 particles with characteristic d-spacing of ~0.209 nm,[106] that supports our earlier HTXRD data in figure 3.7a. This also supports our earlier analysis of the volume contraction model which stipulated that the particle has to release gaseous oxygen while shrinking to increase density and convert to alumina.

Differential Scanning Calorimetry (DSC) was used to measure the heat flux with respect to a reference as a function of temperature for the AlO_x NCs. Figure 3.9 depicts a small heat rise initially between 0 and 600ºC, after which the AlO_x NC begins to melt and off-gas which correlates to an endothermal heat flux. The sample does exhibit a sharp exotherm starting at ~1200ºC, however, at such high temperatures it is likely this is due to oxygen trapped in the alumina DSC pan leaching into the AlO_x melt and reacting. It is for this reason we are mainly concerned with the range from ~600-1000ºC, where the AlO_x NCs are expected to react. This endothermic reaction is associated to a positive increase in the enthalpy of the system.

The preliminary energetic testing and characterizations of the AlO_x NP via LASEM at the DEVCOM ARL facilities have already demonstrated highly promising results showing fast reactivity compared to commercially passivated Al nanoparticles when used as energetic

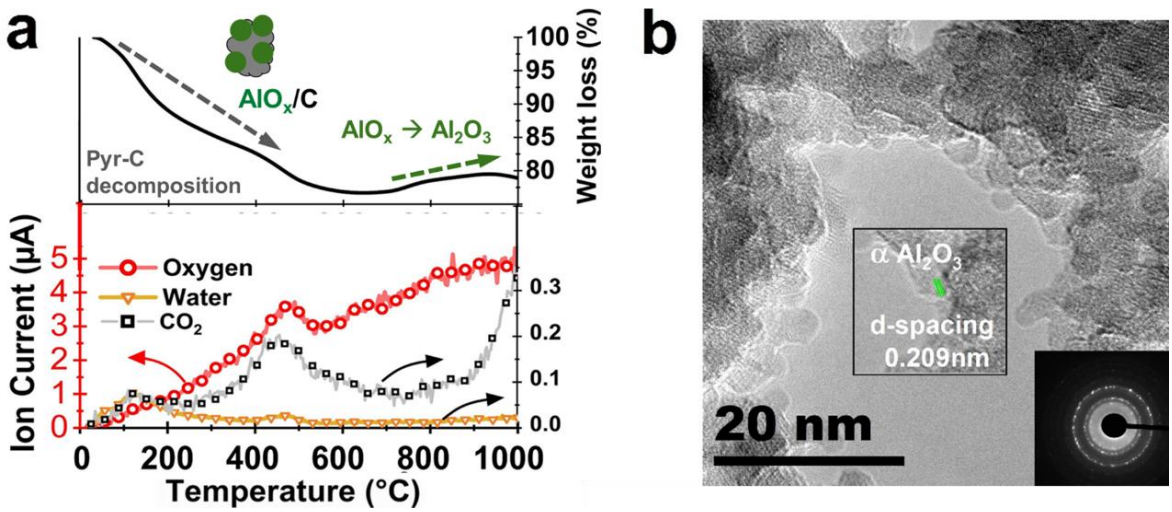

Figure 3.8) TGA-MS measurements revealing large trapped gas release during thermal decomposition of AlO_X/C NCs; **a)** TGA-MS data shows temperature-dependent release of O_2, CO_2, H_2O during the burning of AlO_X/C NCs leading to pyrolyzed-C decomposition up to ~~400-500ºC followed by continual release of O_2 and a sharp peak for CO_2 emissions beyond ~800-850ºC (as indicated schematically in top TGA figure); **b)** HRTEM images of the post-burn AlO_X/C NCs along with the SAED patterns (Bottom right inset box) indicate the final products to be highly crystalline α-Al_2O_3 with the known d-spacing of ~0.209 nm.

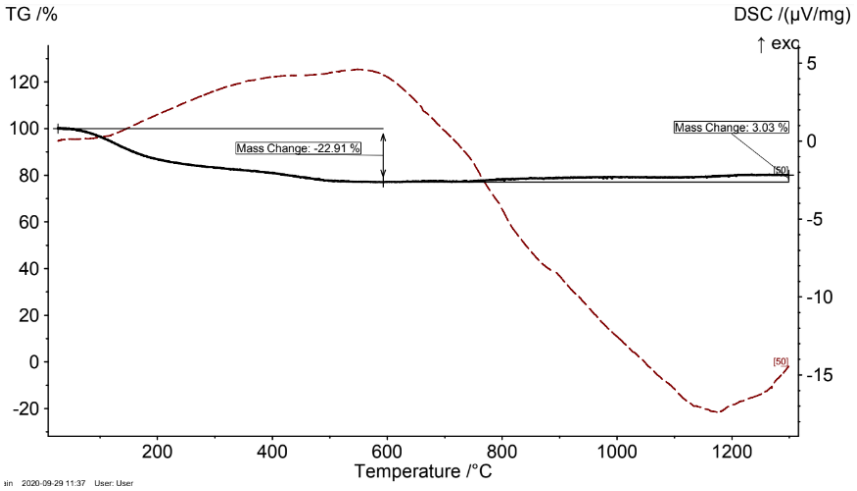

Figure 3.9) DSC for AlOx showing melting and off-gassing endotherm.

additives for solid propellants. Much of these results are published in the *Journal of DoD Research & Engineering (JDRE)*, categorized as distribution D (for release to Department of Defense employees and contractors only). Hence, these results cannot be discussed and/or, divulged for general public distribution. During this project, future collaborations with ARL scientists will continue to provide more comprehensive assessments for the energetic/pyrophoric behaviors of diverse classes of metastable MO_x samples.

3.3 Conclusion:

In conclusion, we have implemented LASiS as a facile yet elegant non-equilibrium technique to kinetically trap metastable hyper-oxidized AlO_x nanostructures that are uniquely phase-stabilized in carbonaceous matrices. Specifically, rapid energy dumping and liquid-phase quenching during LASiS has enabled the metastable freezing of highly disordered and amorphous a-AlO_x ($2.5< x \leq 3.5$) NPs (<5-10 nm sizes) within laser-pyrolyzed C matrix via a one-step, one-pot process. The remarkable stability of these a-AlO_x/C NCs under ambient conditions and, well into temperatures as high as ~750-800^{o}C is explained by the entrapment and stabilization of a-AlO_x NPs in ultra-thin and ordered interfacial C monolayer skins during their growth out of the LASiS-induced reactive plasma environments. Beyond ~750^{o}C, the a-AlO_x nanostructures undergo direct solid-solid phase transitions through various crystalline polymorphic phases of Al_2O_3 ($\gamma/\theta–Al_2O_3$) to ultimately form the equilibrium stable α-Al_2O_3 phase with final coarsened crystallite sizes ~60 nm. The architected stabilization of such a-AlO_x/C NCs via tailored interfacial C structures provides the rational roadmap for the design of disordered metastable materials that can undergo directed amorphous-to-crystalline (metastable-to-stable) solid-state phase transitions under desired thermal perturbations. Based on the observations reported here, one might posit that a plethora of such metastable nanomaterials are waiting to be discovered in the uncharted non-equilibrium phase space limited only by our imagination and techniques. Such disruptive materials discovery can offer a paradigm shift to the development of advanced batteries, solid-state oxygen generators, oxidizer additives in composite joining, or phase-change technologies for neuromorphic computing.

Chapter 4: Investigations into tuning the reaction kinetics and tailoring the compositions (x=O/Al) & structure (crystallinity) of a-AlO_x/C NCs

Disclosure:

This chapter is adopted from a manuscript Submitted to ACS Chemistry of Materials 2024. The full list of authors includes: Elijah Davis, Dibyendu Mukherjee, Claudia Rawn and Matthew G. Boebinger. The role of Elijah Davis was to design and perform all experiments, process and analyze all data, and prepare the manuscript for submission.

4.1 Introduction:

LASiS has a few non-independent synthesis parameters, including, laser flux, wavelengths, repetition rates, pulse duration, and solvent choice, duration of ablation, and solvent temperature, each of which affect the final phase, structure, and morphology of the as-synthesized nanoparticles. Thus, the technique offers the unique capabilities of simultaneously tailoring the structure-composition properties of the as-synthesized NCs, that include: 1) sizes/shapes and crystallinity by tuning laser parameters (fluence, solvent choice, solvent temperature) (within the cavitation bubble); and 2) composition, alloying/composite formation, and morphology by tuning solvent chemistry (temperature, solvent choice, sonication) at the liquid-bubble interface.

Controlling of the final size of the materials produced requires tuning as the final size of the NPs directly relates to their reactivity, with a size decrease increasing the NPs reactive area, internal pressure and size-dependent surface free energy reduction.[20] As a result, a decrease in particle size can be directly related to a decrease in the activation energy barrier (E_{ac}, J) described by the Arrhenius expression for the reaction rate constant: $k(T) = \alpha exp(E_{ac}/k_BT)$ that results in an exponential increase in the reaction rate. This can be seen in previous studies on Al NPs as ENMs, as shown in figure 16a below, where D_p <50 nm particle sizes exhibited a drastic decrease in the activation energy barrier as estimated from the slope of linear Arrhenius plots (ln(k) vs.1/T).[20,29] Based on these results, similar experimental calculations for the activation energies for the AlO_x NPs studied here will be discussed in a later section.

LASiS parameters such as ablation time, laser flux, solvent choice and temperature could affect the final size of the NPs. However, these parameters are not independent and result in other changes to the final NPs. Previous studies from our group on graphitic C coated Al NPs conducted with acetone and toluene as the LASiS solvent had concluded that both the laser flux (J/cm^2) at the target spot and solvent specific vapor pressure play significant roles in the particle's final sizes (see figure 4.1b).[29] The relatively higher vapor pressure of acetone than that for toluene results in enhanced solvent pyrolysis process that, in turn, produces more C to coat the Al NPs and deter the particle growth via coarsening/sintering. The particle sizes/number concentrations

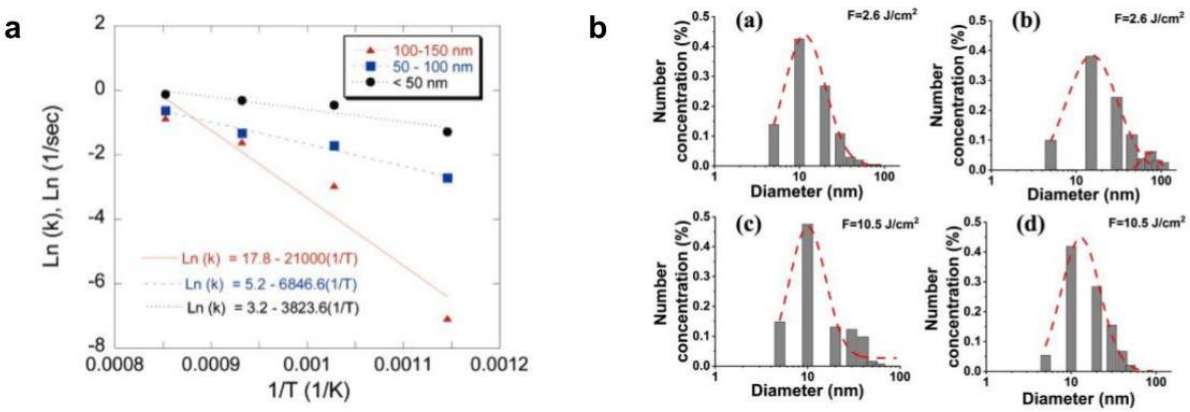

Figure 4.1) (a) Arrhenius plots for Al particles (ln (k) vs.1/T) for three separate size regimes where k is the reaction rate constant and T is the temperature (K); (b) Effect of laser fluence (F, J/cm^2) on the size distribution of C/Al NPs prepared via LASiS in (a & c) acetone and (b & d) in toluene.

will be tailored by altering laser flux, solvent choice and solvent parameters. Solvent temperature/pressure and effective laser beam waists traversing through the solvent can also significantly alter the pyrolysis process thereby allowing us to control the particle sizes and their number concentrations through the retardation in Al aggregation and collisions as discussed earlier. However, as laser flux and solvent choice will be important parameters in other aspects of the final NPs, other methods will be studied to determine their effectiveness. Altering the solvent pyrolysis may also be possible through varying the focal lengths of the focusing lens used to focus the beam onto the metal target. By altering the focal length, the energy density of the beam traversing the solvent can be changed resulting in a change in solvent pyrolysis.

The ***extent of crystallinity*** will be another key aspect of the metastable AlO_x NCs for study primarily due to the difference in amount of energy release between crystalline and amorphous SS-PCMs. Crystalline to crystalline SS-PCMs do not release a lot of stored energy so amorphous to the first crystallite sizes nucleated would presumable release more energy due to entropic compensation from disordered to ordered structues.[40] Similarly, the more disordered the amorphous structure the higher the relative trapped energy density within the bonds leading to even greater yields.

The composition of the m-AlO_x, or the ratio of Al:O, will determine the reactivity and stability of the studied ENMs. As mentioned earlier, only a few phases of metastable Al-oxides established via computational calculations have been found to be stable experimentally. The few Al_xO_y structures that were theoretically found to be stable are shown in in figure 4.2a along with their negative formation energies (E_f, eV) with varying cluster sizes.[45] For our ENM applications, it will obviously be most effective to stabilize a metastable phase with as small a negative value of E_f as possible that can allow the largest energy release upon transition to the stable Al_2O_3 state. Hence, tailoring the relative atomic ratios or the non-stoichiometric ratios in such Al_xO_y clusters by tuning the LASiS energy required to trap the desired state will be crucial in designing the energy dissipation process in the final ENMs. A broad understanding of how this reduction in flux affects the M/O ratios has been demonstrated in a previous study by altering the laser flux and comparing the relative plasma temperature with the resulting AlO_x formation computationally (figure 4.2b). The AlO_x formation was found to increase at lower flux.[44] The elemental composition for the m-AlO_x NPs can be tuned by altering the laser energy required to trap the desired compositions well as the ratios of the constituent elements (Al, C, O) from metal targets and solvents in the LASiS-induced plasma plume to participate in the formation of the specific molecules. The amount of ablated metal will depend on the fluence used for ablation as well as the laser pulse width

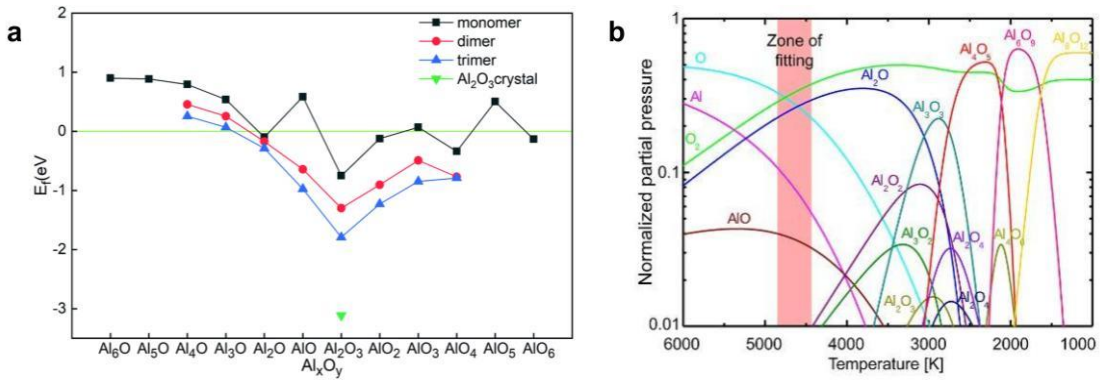

Figure 4.2) (a) Fragment formation energy of $A_{lx}O_y$ monomers, dimers, and trimers; (b) Evolution of the gas-phase composition from 6000 to1000 K.

wavelength and pulse duration. Bearing in mind that although the available M:O ratios in the LASiS system play a rule in the final material structures, the specific plasma conditions driven by the incoming laser flux determine the specific metastable MO_x that can be trapped regardless of the species concentrations present in the plasma. In previous studies, high oxygen content solvents such as methanol have been shown to largely form ground state fully oxidized NPs whereas solvents such as toluene produce more pure metallic and carbide-like structures.[63] The type of bonds within the solvent for each element may also affect this, with double and triple bonds being harder to break. Similarly, solvent temperature will also affect the C:O ratios as it affects the pyrolysis and re-crystallization processes. For a high-powered laser, these parameters may have little to no effect on the final products since the extremely high-T/high-P plasma plume created will overpower all the bond dissociation energies completely. However, in the low flux regime, the amount of energy available for breaking these bonds could significantly decrease to the point that the effective available energy for the target ablation could also get affected. Such synthesis protocols might be challenging to predict for highly complex LASiS process but can be addressed only through systematic execution of control experiments. By choosing different solvents with diverse thermochemical properties (i.e., densities, vapor pressure, specific heats, flashpoints, O, bond arrangements) and comparing the products, real-time correlations will be achieved during this research. Finally, the amount of dissolved oxygen from ambient conditions outside the solvent could also play a large role in the Al:O ratio in the final products.

Experimentally viable non-equilibrium synthesis routes remain elusive with most attempts employing ultra-fast quenching, physical/chemical deposition, high-pressure compression, and mechanical attrition techniques. The similarity in these systems being their non-equilibrium nature that increases the metal's internal entropy through rapid energy dumping and quenching before transitioning to a final stable oxide form. As of currently, LASiS is one of the few methods known that can effectively trap these forms of nanoscale metastable oxides; however, very little is known about the mechanistic underpinning of such trapping process in high-T/high-P plasmas. It has been long-postulated that the highly non-equilibrium LASiS processes can promote this kinetic trapping of metastable states, via rapid laser energy dumping and liquid-phase quenching, however this has rarely been seen experimentally except for a few sparse reports. Several attempts have been made to describe the exact plasma physics within the LASiS plume, many of which rely heavily on what is an already well known and established study of stable equilibrium plasma physics. However, the rapidly evolving out-of-equilibrium plasma dynamics during LASiS makes any rational experimental approach to investigating the complex plasma reaction pathways become immensely challenging. Bearing in mind that any computational model for such a

complex process will involve a massive undertaking, few efforts to date have tried to tackle this challenge experimentally by conducting in-situ LIBS to probe into the plasma during real-time LASiS operation to extract the evolution (birth and death) of various chemical species during the process. As shown in figure 4.3, the exact determination of the localized free energy minima that enables the kinetic trapping of these m-AlO_x NCs during the laser plasma-induced reaction process will be a grand challenge question for this proposed work. Herein, as seen in figure 4.4a, the first barrier is the activation energy (E_{ac1}) for the formation of AlO_x in the LASiS-induced plasma. This can be extracted by analyzing the plasma dynamics via in-operando LIBS to investigate the various plasma species evolution. The second barrier is the activation energy (E_{ac2}) required for the solid-solid phase transition to the final stable α-Al_2O_3 product. E_{ac2} will be investigated by carrying out reaction kinetics analyses using real-time phase transition of amorphous AlO_x to crystalline α-Al_2O_3.

4.2 Results and Discussions: Chemical kinetic analyses for solid-solid phase transition

Phase-stabilized structures of the amorphous and highly disordered m-AlO_x@C NCs, as synthesized via LASiS in our previous work, were studied here using HRTEM to carry out areal density measurements.[107] Having previously reported on the structure-composition properties of the m-AlO_x NPs trapped in a non-equilibrium phase and stabilized by C-shell monolayers, this work focuses on the material's phase change characteristics. Using HRTEM EELS, the electron-beam scattering probability (ppm/eV) as a function of the electron energy loss is estimated from the Al and O spectrum (figure 4.4b) for five different particles in relation to their respective sizes. The EELS spectra were then used to calculate the approximate number of Al and O atoms. By fitting a model of scattering probability vs eV to the raw data, the number of Al and O atoms for each particle could be extrapolated. Knowing both the number of atoms present as well as the particles respective size, the effective areal density of the NPs could be calculated and compared to that of standard Al_2O_3 NPs of the same particle size. The average areal density of Al atoms was found to be ~15000 atoms/nm^3, which is roughly 10 times less dense than its Al_2O_3 counterpart. Table 4.1 provides the average ratio for five NPs measured compared to the average Al_2O_3 NP areal volumetric density. The particles on average are ~ 6-7 times less dense than an Al_2O_3 NP of the same size.

The phase transition from θ/γ-Al_2O_3 to α-Al_2O_3 has been well studied throughout other publications, however, the study of an amorphous metastable material to its first semi-stable crystal structure has considerably less research to date.[108-110] For this reason, the focus of this

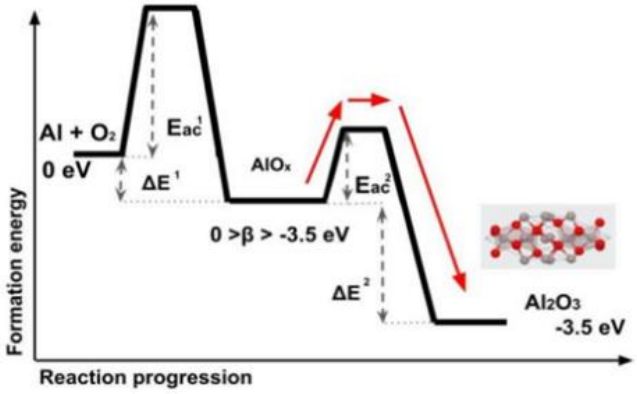

Figure 4.3) Formational energy depiction of reaction barriers of interest $E_{ac(1)}$ and $E_{ac(2)}$ as well as the net energy released ΔE(2).

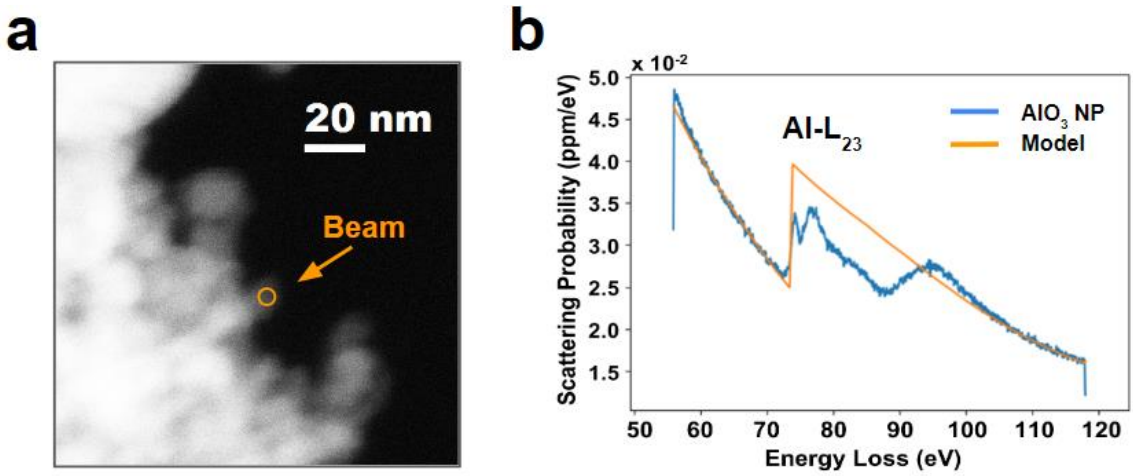

Figure 4.4) AlO_3 density measurements: a) Chosen NP for density measurement at the center of the AlO_3 NP indicated as "beam". b) EELS spectra for chosen particle marked in blue with model fit as orange.

Table 4.1) Measured size, atomic areal, volumetric density and volumetric density ratio for chosen AlO_3 NPs.

Particle size (nm)	Atoms/nm^2	Atoms/nm^3	Volumetric density ratio
13 ± 0.5	84	6.5 ± 0.2	2.3 ± 0.1
7 ± 1	9	1.3 ± 0.16	11.4 ± 1.6
11 ± 0.7	32	3.0 ± 0.17	5.0 ± 0.3
9 ± 1	60	6.7 ± 0.7	2.2 ± 0.2
12 ± 0.5	19	1.6 ± 0.1	9.2 ± 0.4

work is solely on the first phase transition from AlO_x/C to θ/γ-Al_2O_3. In our previous publication we observed that the AlO_x/C NCs began to transition from their initial amorphous phase to θ/γ-Al_2O_3 (700 $^oC < T < 900\ ^oC$) and finally to α-Al_2O_3 ($T > 900\ ^oC$).[107] During the initial transition to the semi-stable θ/γ-Al_2O_3, the material undergoes a disproportionation reaction, where AlO_x with an intermediate oxidation state (O^{1-}) converts to Al_2O_3 with a higher oxidation state (O^{-2}) and O_2 (g) with a lower oxidation state (0) as shown in the reaction equation below (EQ6). Equation 2 (EQ7) shows that the O anion must be -1 to charge balance AlO_x and equation 3 (EQ8) shows that the O anion must be -2 to charge balance Al_2O_3.

$$2AlO_{X\ (solid)} \rightarrow Al_2O_{3\ (solid)} + \frac{X}{2}O_{2\ (gas)} \qquad EQ6$$

$$2AlO_X\ charge\ balance: \qquad 2(+3) + 2X(-1) = 0\ for\ 3.0 \quad EQ7$$

$$Al_2O_3\ and\ O_{2\ (gas)}\ charge\ balance: \qquad 2(+3) + 3(-2)\ + 2(0) = 0 \quad EQ8$$

This makes the m-AlO_x@C phase transition fairly unique since the majority off SS-PCMs undergo oxidation or simply bond rearrangements resulting in matching oxidation states for both reactant and product. The only other disproportionation reactions in SS-PCMs are known to occur in peroxides phase transitions.[100,111]

In-situ high-temperature quantitative X-ray diffraction (HTXRD) studies are used to determine the detailed chemical kinetics analyses of solid-solid phase transitions of the highly disordered (amorphous) and metastable m-AlO_x (x~2.5-3.0) stabilized by ordered C-shells into the semi-stable θ/γ-Al_2O_3 phase via disproportionation reaction. HTXRD provides a characterization method that can probe the kinetics of phase transformations in real time by rapidly collecting diffraction data during heating under both non-isothermal and isothermal conditions. This allows for identification of metastable and non-equilibrium phases and kinetic pathways. The kinetic phase transition can be tracked by analyzing the increase in peak area which corresponds to crystallization. For isothermal experiments the evolution of crystallization can be tracked as a function of time for a particular temperature. The ensuing conversion rate, denoted as α, which can be experimentally measured as the peak area measured over time divided by the maximum crystalized area or $\alpha = A_{observed}/A_{max}$. Focusing on the strongest intensity visible theta/gamma peak, centered around ~45.5 2θ, as shown in Figure 4.5a, for five separate isothermal conditions, between 750 and 790 ^oC, HTXRD data were collected until the peak reached its maximum

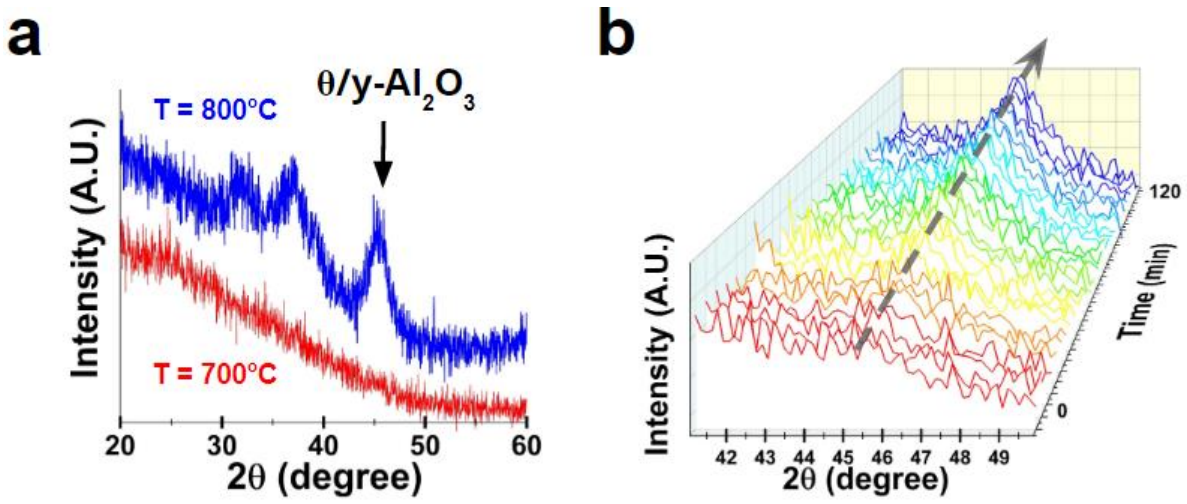

Figure 4.5) HTXRD measurements and analysis of AlO_3 nano composites: a) HTXRD taken at a temperature of ~700 ºC and ~800 ºC showing a broad peak for Gamma/theta alumina. b) Amorphous to Gamma/theta in-situ XRD heating measurement showing increase in peak through time for a set temperature of ~750ºC.

intensity and no longer increased. Figure 4.5b displays the emergence and increase in intensity as time progresses illustrating the material's amorphous to polycrystalline transition with the increase in intensity relating to the concentration of crystallites nucleated. Even after allowing for the appropriate time to achieve the maximum transformed to θ/γ-Al_2O_3 crystals, the peaks for all temperatures retain low relative intensity and high broadening. This is could be due to their polycrystalline nature with a small crystallite size of ~3-4 nm.[107]

In this case the α vs. time curve can be used to determine the kinetic model which best describes the kinetic phase transition. The most common kinetic models can be broken into four main categories, nucleation, geometrical contraction, diffusion, and reaction-order models shown in table 4.2.[112-114] In the case of most solid-state crystallization, the reaction is described by nucleation models or Avrami models. In the case of crystal nucleation, the reaction governing rate is driven by the nucleation rate at heterogeneities within the lattice known as nucleation sites. Nucleation models can be driven by exponential, linear, power or instantaneous equations and are therefore often quite fast in comparison to other transition models. For diffusion-controlled phase transitions, the mobility of constituents through the lattice is the rate limiting factor. In diffusion driven reactions such as metallic oxidation, the rate of product formation along the reaction wall decreases the mobility of constituents as the thickness of the product barrier layer increases. Phase boundary-controlled reactions such as geometric contraction models assume that nucleation of the phase change takes place at the surface and growth is rate limiting factor. Reaction order models are simplistic models that assume the reaction rate is proportional to concentration or number of reactants present and decrease as reactants convert to product.

The areas for the resulting peaks throughout each isothermal test condition were obtained by fitting each peak using the HighScore data analysis package then normalized to the largest peak area at the conclusion of each isothermal data collection. This gives us the effective extent of conversion for each isothermal temperature measured throughout time or α. Figure 4.6 shows α vs time for the lowest and highest isothermal temperatures. The total conversion time decreases as the temperature increases. The slope, with higher slopes correlating to faster conversion rates, increases as temperature increases, shown in Figure 4.7a, as more energy is input into the system promoting the phase transition.

By comparing the extent of conversion data to the possible conversion models a suitable phase transition model could be chosen.[112-114] In all cases, the volumetric contraction model, R3, fit most appropriately (figure 4.6) and compared for 750 and 790 ^{o}C in Figure 4.7a. The equation for the volumetric contraction model can be seen below, where f(α) is a mathematically derived

Table 4.2) Kinetic models for Nucleation, Geometric Contraction, Diffusion and Reaction Order models with Solid-State Rate and Integral Expressions

		$f(\alpha) = 1/k\,(d\alpha/dt)$	$g(\alpha) = 1/k\,(d\alpha/dt)$
Nucleation	½ Power law (P2)	$2\alpha^{1/2}$	$\alpha^{1/2}$
	⅓ Power law (P3)	$3\alpha^{2/3}$	$\alpha^{1/3}$
Geometric Contraction	Area contraction (R2)	$2(1-\alpha)^{1/2}$	$1-(1-\alpha)^{1/2}$
	Volume contraction (R3)	$3(1-\alpha)^{2/3}$	$1-(1-\alpha)^{1/3}$
Diffusion	2 Dimensional Diffusion (D2)	$-(1/\ln(1-\alpha))$	$((1-\alpha)\ln(1-\alpha))+\alpha$
	3 Dimensional Diffusion (D3)	$(3(1-\alpha)^{2/3})/(2(1-(1-\alpha)^{1/3}))$	$(1-(1-\alpha)^{1/3})^2$
	Ginstling-Brounshtein Diffusion (D4)	$3/(2((1-\alpha)^{1/3})-1)$	$1-(2/3)\alpha-(1-\alpha)^{2/3}$
Reaction Order	First Order	$(1-\alpha)$	$-\ln(1-\alpha)$
	Second Order	$(1-\alpha)^2$	$(1/(1-\alpha))-1$
	Third Order	$(1-\alpha)^3$	$\frac{1}{2}((1-\alpha)^{-2}-1)$

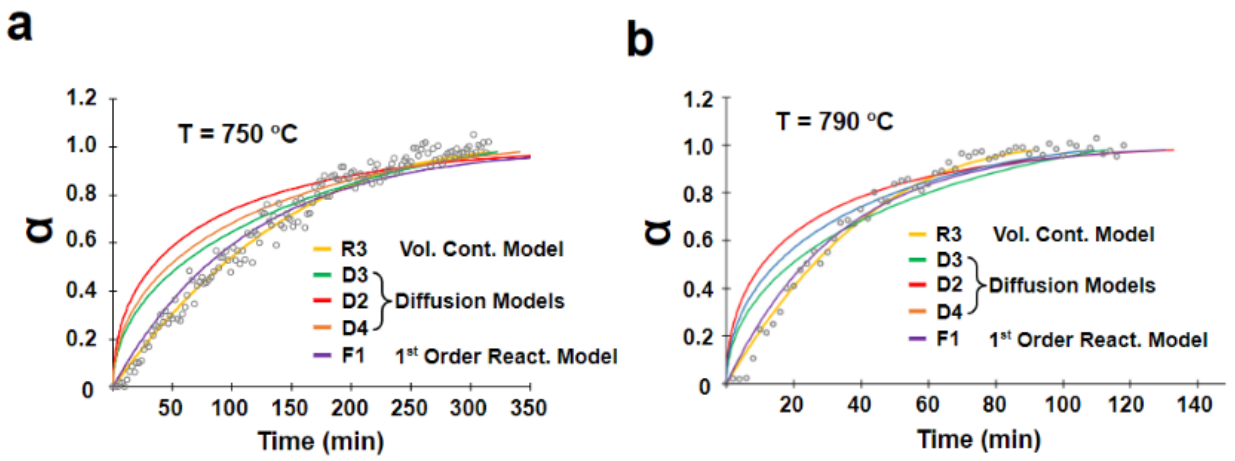

Figure 4.6) Conversion factor alpha (α) vs time. a) Alpha (α) vs time for an isothermal temperature of 750°C compared to known solid phase change models. b) Alpha (α) vs time for an isothermal temperature of 790°C compared to known solid phase change models.

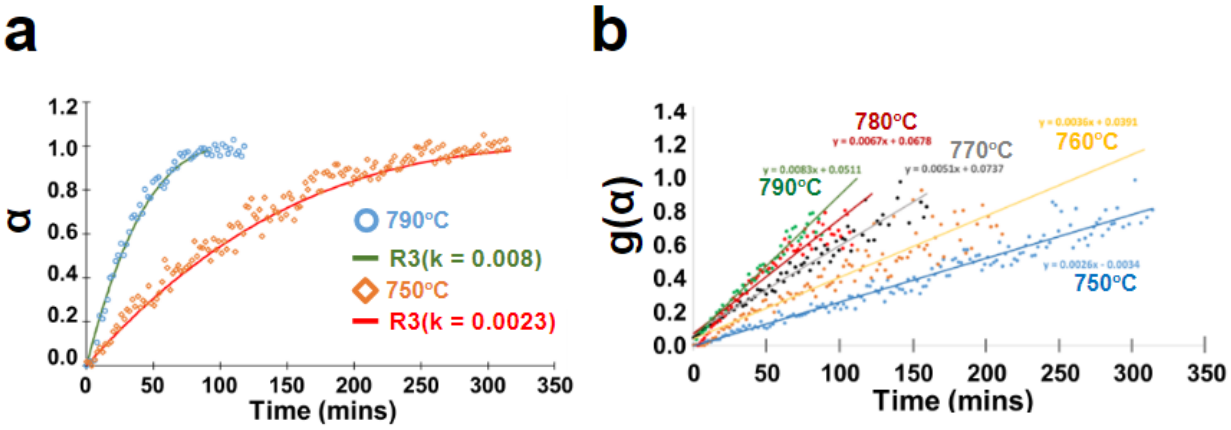

Figure 4.7) Isothermal kinetics analysis of AlO_X NCs: a) HTXRD measured at ~750°C and ~790°C compared to volumetric contraction model after fitting rate constants (k). b) data linearized using volumetric contraction model g(α).

representation (EQ9) of the reaction model and g(α) is the integral form of f(α) (EQ10). In the following equations dα/dt is the rate of conversion with respect to time where k is the conversion rate constant.[20] The calculated fits in Figure 4.7a were obtained by varying the k values to obtain the best agreement to the data resulting in, k = 0.0023 S^{-1} and k = 0.008 S^{-1}, for 750 and 790 ^{o}C, respectively.

$$f(\alpha) = 3(1-\alpha)^{2/3} = \frac{1}{k}\frac{d\alpha}{\mathrm{dt}} \qquad EQ9$$

$$g(\alpha) = 1-(1-\alpha)^{\frac{1}{3}} = kt \qquad EQ10$$

Once a suitable model is chosen, the two SS-PCMs parameters discussed earlier, the relative thermal energy storage and related kinetics, can be approximated. In the context of using the volumetric contraction model, coupled with the extreme porosity of the material, the AlO_x/C NPs will have to contract considerably to achieve the large change in density of the transitioned θ/γ-Al_2O_3 polycrystals. This can be seen in the size reduction from the ~ 10 nm NPs to the ~3-4 nm θ/γ-Al_2O_3 polycrystals. After determining the appropriate crystallization model, EQ5 with the data was used to calculate g(α) and compared to a linear fit, placed through the region of the data in Figure 4.7b where there is minimal scatter and the slope remains constant. The slope for each isothermal temperature represents the respective k value or reaction rate constant at that temperature, agreeing well with the reaction rate constants predicted using the function in Figure 4.7a.[20,112,114]

$$\frac{d\alpha}{\mathrm{dt}} = Aexp\left(-\frac{Ea}{RT}\right)f(\alpha) \qquad EQ11$$

With the reaction rate constant determined, the Arrhenius equation (EQ11) where A is the pre-exponential factor, Eα is the activation energy, R is the ideal gas constant and T is the isothermal temperature can now be used. The reaction activation energy barrier Eα could be approximated by comparing the natural log k with respect to the isothermal temperature of each reaction and taking the linear fit of the points. The resulting slope of the linear fit divided by the gas constant is equal to the average activation energy barrier or the perturbation energy needed to induce the phase transition. For the AlO_x/C NC the activation energy was found to be ~ 270 kJ/mol (figure 4.8a) approximately 8 times of that reported by Park et al., where NPs of similar

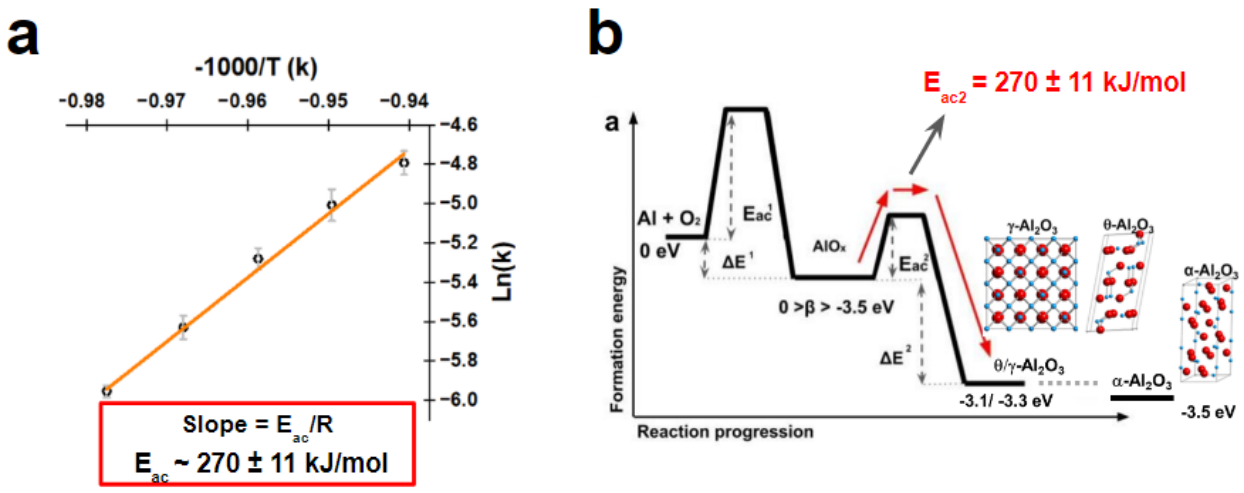

Figure 4.8) Activation energy plots for AlO_3 nano composites: a) Plot showing the average activation energy barrier needed to induce the phase transition. b) visual depiction of average activation energy barrier for AlO_X stuck in localized energy well.

sizes required only ~32 kJ/mol to induce diffusion driven oxidation, making the AlO_x NCs roughly as stable as a micron sized Al particle.[20] The extreme stability of the AlO_x/C NCs is likely due to the monolayer carbon atom shell stabilizing this metastable material discussed in Davis et. al. and as a result also increasing the material's activation energy.[107] Similar to figure 4.3, we can construct a precise depiction of the kinetic entrapment of the AlO_3 nano composite through the analysis of our experimental data depicted in figure 4.8b. E_{ac}^1 represents the amount of energy required to trap the metastable structure while E_{ac}^2 is the energy required to perturb the material enough to induce the SS-PC. Delta E^1 is the depth of the energy well that the material is trapped or the formation energy of the AlO_3 in the LASiS-induced plasma and Delta E^2 is the amount of energy release upon perturbation which in this case is the difference between the formation energies of AlO_3 and gamma alumina or ~ 2 eV/atom (193 kJ/mol).

To investigate the structural evolution during the high-temperature phase transition of the as-synthesized amorphous m-AlO_x phase in the NPs into the semi-stable θ/γ-Al_2O_3 polymorphic phase in-situ S/TEM imaging on a high-temperature stage was used at a fixed temperature of ~710 ^oC. The temperature was slowly increased in increments (~550 ^oC then ~710 ^oC) to ensure that the onset of the phase transition and crystallization to the intermediate θ/γ-Al_2O_3 phase was slow enough to be observed at ~710 ^oC (figure 4.9). This also ensured that once crystalized the intermediate semi-stable phase, observed in TEM images and confirmed via d-spacing measurements (figure 4.10), could be verified before the NPs could transition to the final phase α-Al_2O_3. Using in-situ TEM the volume changes for two separate spherical particles were tracked, as indicated in figure 4.9, wherein the starting amorphous volume of the particle was noted to be ~524 nm^3 (diameter ~ 10 nm). After ~20 seconds of isothermal heating at ~710 ^oC, the inspected particles are observed to have decreased to ~45 nm^3 (diameter ~ 4.4 nm), thereby undergoing a volume contraction of ~12×. This correlates well with our previous analysis of the areal density measurements for the AlO_x NPs which notably found the density to be ~10 times less dense than standard alumina. These results suggest that the initial metastable to semi-stable phase transition of amorphous m-AlO_x to crystalline θ/γ-Al_2O_3 must follow a volume contraction process wherein the size of the particle does in fact decrease in order for the densification to occur and facilitate the crystal growth.

Just after the visualized volume contraction, detailed inspection of the aforesaid NP in the final frame of figure 4.9 (time = 44 sec) via HRTEM revealed that the particle indicated a measurable d-spacing of ~0.3 nm (shown in figure 4.10a, b) which matches that of the (220) crystal orientation for the γ-Al_2O_3 polymorphic phase.

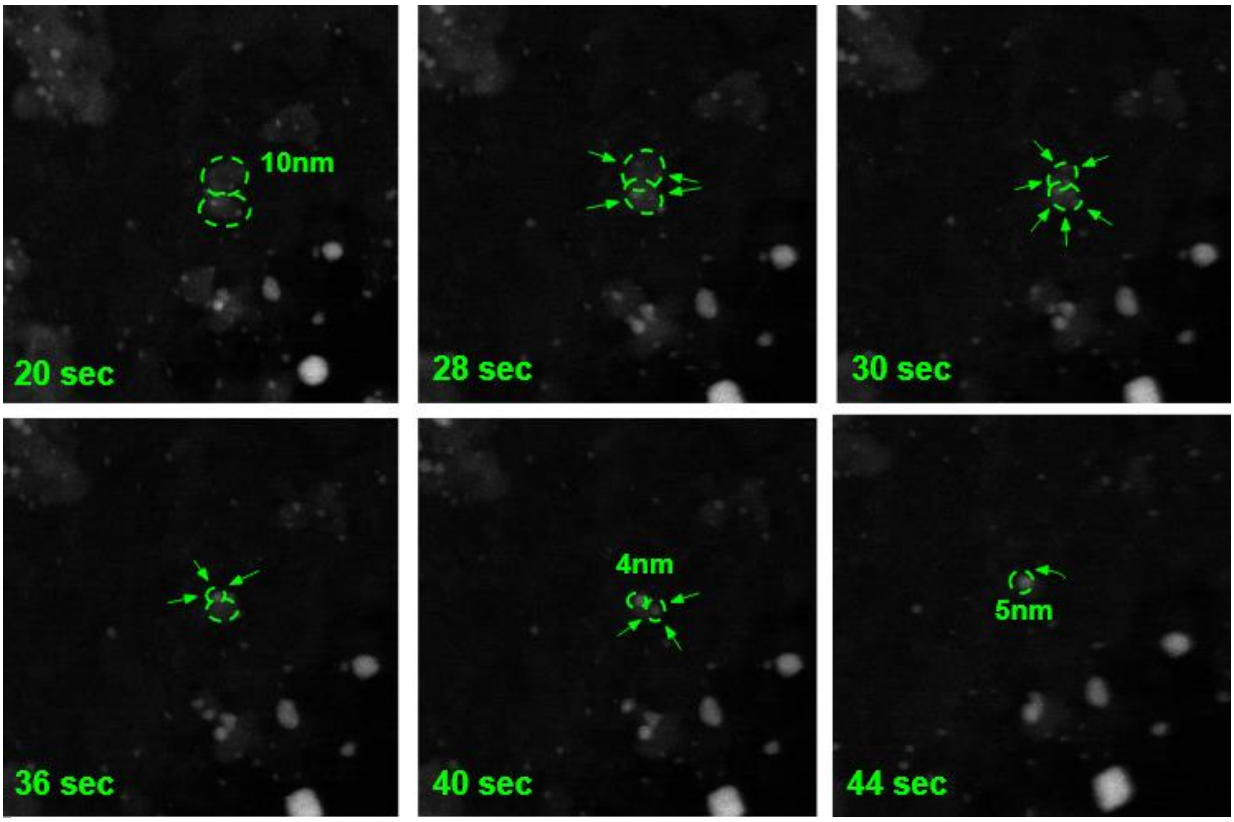

Figure 4.9) In-situ heating TEM showing the decrease in size of the AlO_X NPs during transition from amorphous to crystalline.

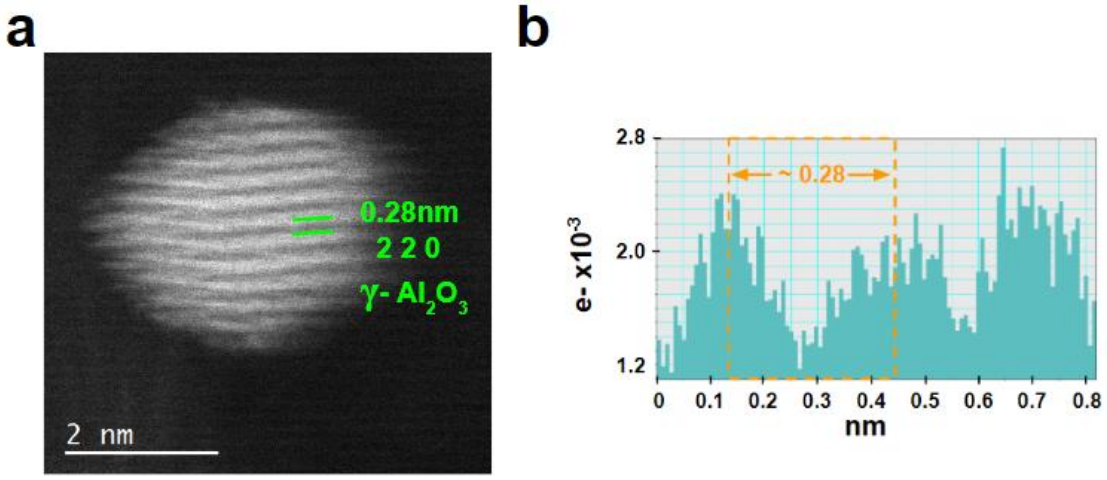

Figure 4.10) TEM analysis of NP shown in figure 4.9 post heating to ~810ºC: a) NP showing clear crystalline lattice spacings of roughly 0.28nm. b) Line plot of crystal lattice spacings for NP shown in (a).

The first assumption made about the structure of this unique meta-stable hyperoxide was that it should be fairly dense due to the stabilization method and the synthesis method. LASiS NPs are thrown into the surrounding solvent to rapidly quench and at this time almost instantaneously phase stabilize into the meta-stable structure observed. After quenching, the material is held at this state by an ultra-thin atomic monolayer of carbon at the NP's outer most edge due to the high dissociation energies of diatomic covalent C−O (~11.2 eV) and C−C (~6 eV) bonds.[90,104] It is for this reason that our initial hypothesis was that the AlO_3 NPs would be trapped in a form of high internal compression, with the carbon monolayer containing the internal metastable structure like a balloon. However, what we instead found was a highly porous material (~3.8 atoms/nm^3), several times less dense than common alumina. This could mean that as the NPs exit the plasma, they instead undergo rapid expansion before phase stabilizing due to their transition from an ultra-high pressure plasma to the vastly less pressurized ambient solvent. The pressure difference going from the plasma conditions to ambient solvent can be as high as GPa in magnitude.[65] Next, we focused on the phase transition model which would most accurately match our experimental data gathered during isothermal HTXRD.

Due to the starting composition and final product composition, we could confidently state that oxidation was not occurring during phase transition as tracked by isothermal HTXRD, so diffusion limited transformation models are not applicable. However, a phase transition boundary could be present which would resemble a diffusion transition. To rule this out a two-model system which would assume a fast nucleation followed by a slowed boundary layer diffusion driven transition was attempted. This would result in a two-reaction rate and a two-activation energy approximation. When compared to the data, however, the two-model system did not easily fit with the determined slopes at all isothermal temperatures and it was determined the three-dimensional contracting volume model fit better in all cases as the simplest and most direct method of transition. Even before the direct visualization of the volumetric shrinkage, the three-dimensional contracting volume model made logical sense given the reaction steps that would be needed during phase transition. The starting material in question, AlO_3, was known and was hyperoxidized and substantially less dense than the gamma alumina product material. This meant that the AlO_3 NPs would first need to release the excess trapped oxygen before shrinking to accommodate the denser gamma alumina lattice structure. This leads us to conclude that the released excess trapped oxygen and the nucleation of γ-Al_2O_3 crystals must be relatively quick when compared to the shrinkage of the starting NPs, otherwise those would be the transition rate determining processes.

The finding of such a high activation energy makes the AlO_3 nano composites an extremely stable form of solid energy storage. However, as discussed earlier, this could make it difficult to tap into the estimated ~2 eV/atom due to its high stability. Past works have focused primarily on the phase transition between the semi-stable θ/γ-Al_2O_3 phase alumina to ground state α-Al_2O_3. In this study we chose to focus solely on the metastable to semi-stable change, this was because not only has the formerly mentioned phase change been extensively studied but it is also the least energy releasing step of the process. In figure 4.8b we can see that the phase transition from θ/γ-Al_2O_3 to α-Al2O3 is a relatively weak formation energy difference, relinquishing at max ~0.4 eV/atom and a small activation energy making it unstable during storage. Current aluminum air (Al-air) batteries function using the reaction driven formation of $Al(OH)_3$ with the addition of a electrolyte, typically potassium hydroxide with a formation energy difference of ~ 2 eV/atom. The phase change material presented here has the potential to have similar energy densities to that of current Al-air batteries with the main difference being the reaction kinetics discussed throughout. Additionally, the oxygen release during reaction could allow for a secondary reaction with a conventional Al anode allowing for a closed loop, fully closed cell design. More study is required, though the potential for such revolutionary metastable nanocomposites could hold the key to advancing a plethora of new and emerging technologies.

4.3 Analysis of structural arrangements and disorder in metastable a-AlO_x/C NCs

To establish a more in-depth analysis of the AlO_x metastable structures, a series of experiments were undertaken involving atomic Pair Distribution Function (PDF) analyses from x-ray scattering experiments at several time-steps throughout the material's high temperature transition from metastable to semi-stable phases. By comparing the atomic bond arrangements and radii for the initial material to those recorded at each stage of heating throughout the transition process, the relative change in instability and disorder-order transition could be tracked during the material's phase change. Figure 4.11 shows an initial measurement using an Ag x-ray source to measure and calculate the material's PDF spectra. Using this as a starting point, we could proceed to measure and compare the initial average Al-O and Al-Al atomic radii to that of the sample at the beginning of their transition to γ/θ-Al_2O_3, intermediate and final state of conversion. This could enable us to estimate the internal atomic coordination shifts as the material transitions from meta-stable to semi-stable nanostructures. The first transition step was heat treated at ~550^{o}C for 3 hours then cooled to room temperature before measuring. At this stage, it was difficult to differentiate between possible carbon compounds and the Al-O and Al-Al bond

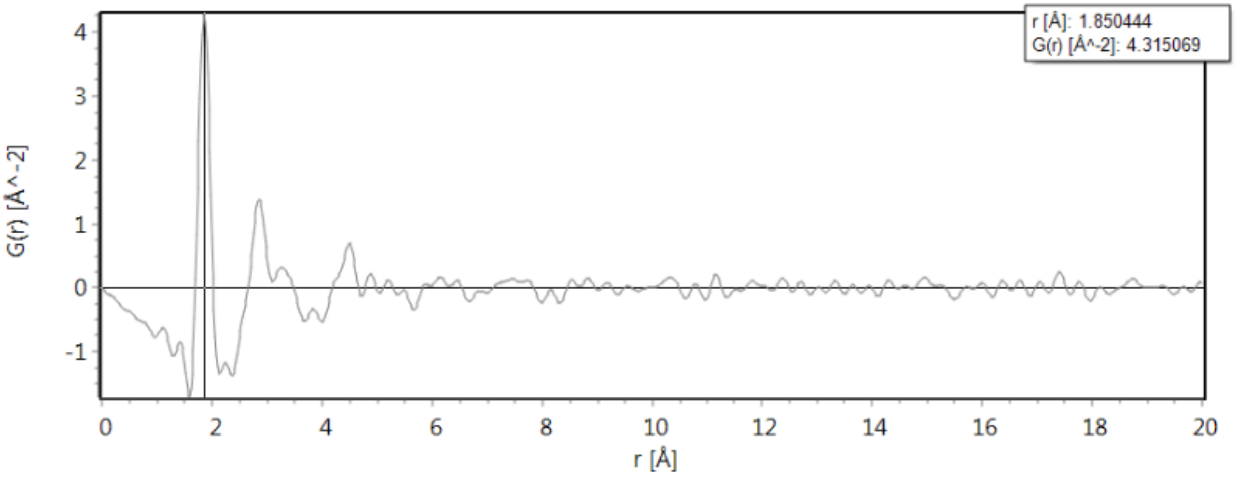

Figure 4.11) PDF of AlO_X NCs showing an average Al-O distance of ~0.185nm and a reasonable pairing of up to ~1nm resolution.

distances we were investigating. The ~550^{o}C transition served to help eliminate possible carbon contamination because at this temperature the a-AlO_x nanostructures would be unaffected, but the carbon structures should show a visible decrease in concentration comparatively. Next, we chose a transition step which would demonstrate a partial conversion of the a-AlO_x nanostructures. Bearing in mind the earlier section wherein we discussed the conversion kinetics of the a-AlO_x nanostructures, we could see that at a temperature of ~750^{o}C we could reliably undergo a particle conversion for between 50 to 250 minutes. The second transition step was heated to a temperature of ~750^{o}C for 2 hours to insure a nearly 50% conversion of the a-AlO_x nanostructures. Finally, third transition step was heated to ~810^{o}C for 2 hours to ensure a full conversion of the a-AlO_x nanostructures to the desired γ/θ-Al_2O_3.

In figure 4.12 we can see that initially the as-synthesized structure retains very little medium-range order indicating a highly disordered and amorphous material. For the first transition step, we can also see that the long-range order did not increase, which is to be expected as at low temperatures the AlO_x structure should not change. As the temperature increases in the second and third transition steps slightly higher long-range order can be differentiated, with the last transition step depicting the most long-range order. In the case of the last transition step, long-range order can be differentiated until roughly 50 Å, which is indicative of a low order polycrystal structure.

We began by refining and comparing individual fitting of the PDF data at the final temperature step 810 ^{o}C with suspected alumina and aluminum hydroxide structures. However, rather than undertaking the trial and error method, we instead converted the silver x-ray source to copper k-alpha and compared that to the γ/θ-Al_2O_3 bearing in mind our previous findings. In figure 4.13, the converted final temperature step 810 ^{o}C XRD pattern correlates fairly well with a known semi stable form of gamma alumina specifically γ-$Al_{2.14}O_{3.2}$.[115] This serves as a good verification, ensuring that the transition in question did not overshoot and begin converting to α-Al_2O_3.

With the polycrystalline structure at the final transition step we could now work backwards to obtain the PDF match as well as the contributing elemental bond lengths associated with each peak position. Figure 4.14a shows the PDF structure for the final transition step compared to the matched gamma alumina structure using XRD. The measured PDF peaks differ slightly from the matched structure whereas the XRD data seemed to match quite well. This could be due to a number of reasons, with the most plausible being a relatively high percentage of amorphous content belonging to another structure—which would explain why the fit begins to follow the matched γ-$Al_{2.14}O_{3.2}$ at longer order radii. By splitting the matched structure into its relative

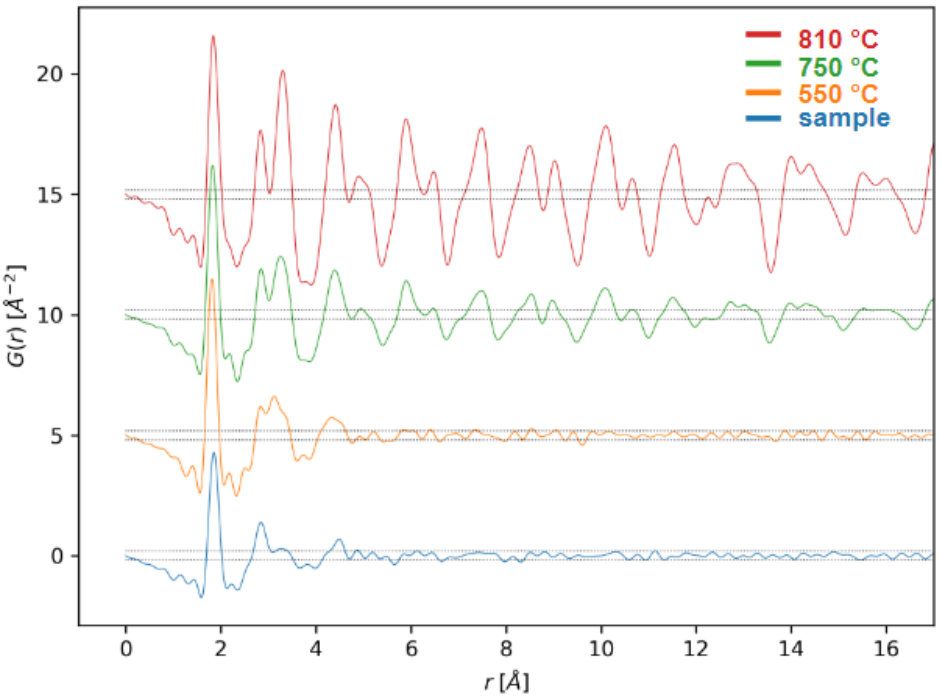

Figure 4.12) PDF of AlO_X NCs temperature evolution throughout transition steps 1-4 from room temperature to ~810ºC.

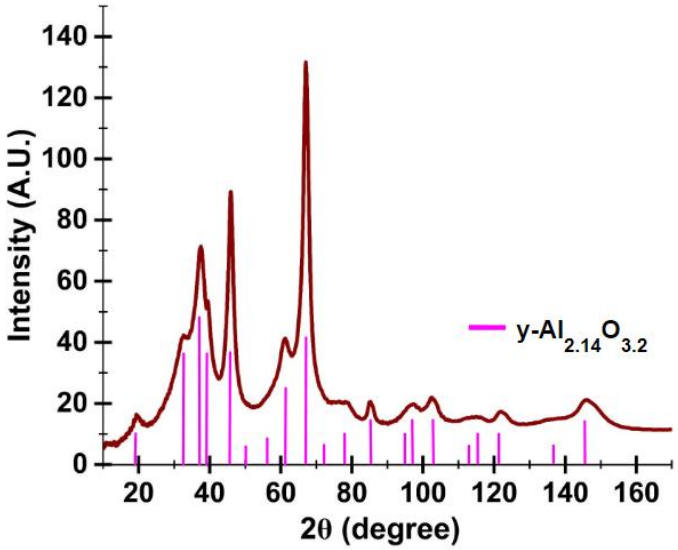

Figure 4.13) XRD match of PDF of the AlO_X NCs after ~810ºC.

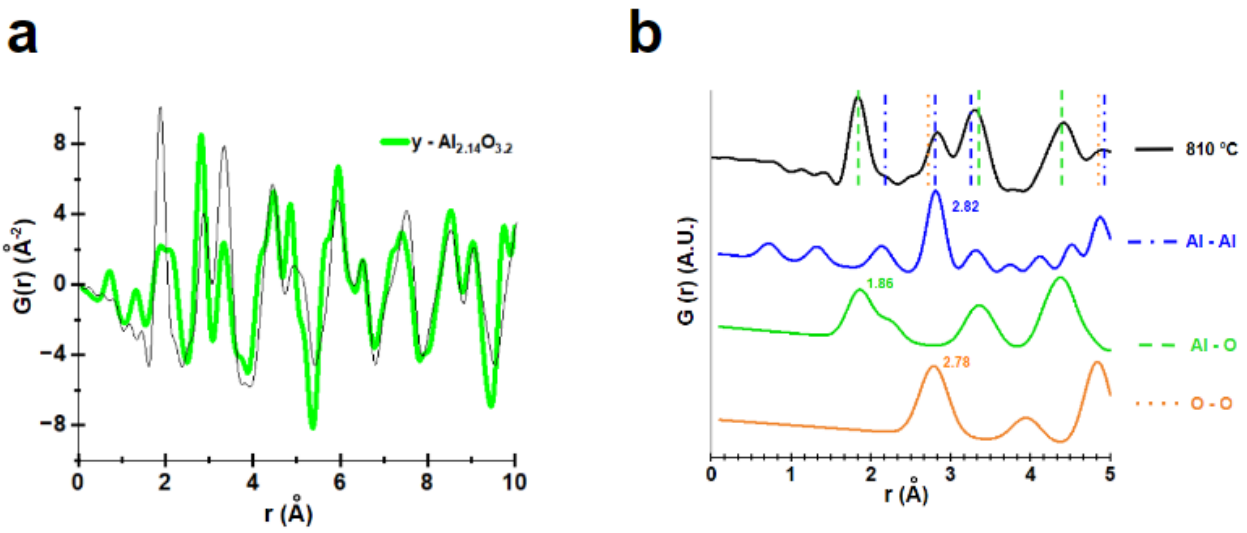

Figure 4.14) PDF analysis using XRD matched structure. a) PDF fit of the γ-Al $_{2.14}$O $_{3.2}$ structure compared to measured data at final transition step. b) PDF fit of the structures in (a) broken into its respective elemental bond pairs.

elemental bond couples seen in figure 4.14b, we could begin to decipher which elemental bond couples dissociate the fit due to the amorphous content. In the data plotted for the final transition step, the Al-O bonds at distance radii of ~1.86 Å show a significant increase in area when compared to the matched γ-$Al_{2.14}O_{3.2}$, which is met with a subsequent area decrease in the Al-Al radii peak at ~2.82 Å. It is unclear whether this is due to the presence of another amorphous alumina/hydroxide structure or if it is due to remaining unreacted AlO_x structures. It is also possible that the matched γ-$Al_{2.14}O_{3.2}$ structure exhibits more bimodal behavior in the low order radii whereas experimentally the peaks are closer resulting in one large peak instead of two smaller peaks.

Figure 4.15a shows the four transition steps compared with the matched elemental bond couples overlaid. As the transition step temperature increases, the peak intensity begins to narrow and we can see the emergence of a few of the longer order Al-O peaks particularly at radii of ~3.25 Å and ~4.4 Å while the Al-Al bond radii stay relatively constant. This could indicate that the Al-Al bonds do not alter much as the material phase transitions, but the Al-O bonds undergo vast change including coordination shifts and bond rearrangement. If we compare the Al-O first nearest neighbor radii in figure 4.15b we can see that the as synthesized sample starts very broad with a peak maxima at ~1.855 Å. Interestingly, at the first transition step of 550^{o}C, we observe a peak shift of ~0.043 Å to ~1.812 Å however, at this temperature it can be assumed that no structural change occurs within the AlO_x NPs and only carbon burn off is represented from initial sample to first transition step. This is likely due to some Al-Al bonds at ~2.1 Å from parasitic pure Al NPs discussed earlier which oxidize at 550 ^{o}C, shifting the peak slightly toward higher radii. Once that excess carbon and Al NPs were accounted for, the remaining two transition steps could be used to observe the shift in coordination. At the third transition step or 750^{o}C the partial transition results in a shift of ~0.02 Å from ~1.812 Å to ~1.83 Å. Finally, at the fourth transition step or 810 ^{o}C the full transition results in a further shift of ~0.01 Å from ~1.83 Å to ~1.84 Å. This can be explained as the metastable AlO_x structure, which from the SS-NMR data discussed earlier can be considered a mix of AlO_4, AlO_5 and AlO_6 coordinations, gradually transitioning into the primarily AlO_6 coordination structured γ-$Al_{2.14}O_{3.2}$. Using the ratio of the first nearest neighbor Al-O peak area to the bound Al-Al nearest neighbor peak area we can calculate an average coordination number which will be equal to the number of AlO_4, AlO_5 and AlO_6 coordinations present in the structure. The fourth and third transition steps have an average coordination ratio of ~5 and ~4.78 respectively. This matches quite well to a 40-60% AlO_6 and 60-40% AlO_4/AlO_5 coordination ratio mix. In the case of the first two transition steps however, the ratios are significantly higher—with

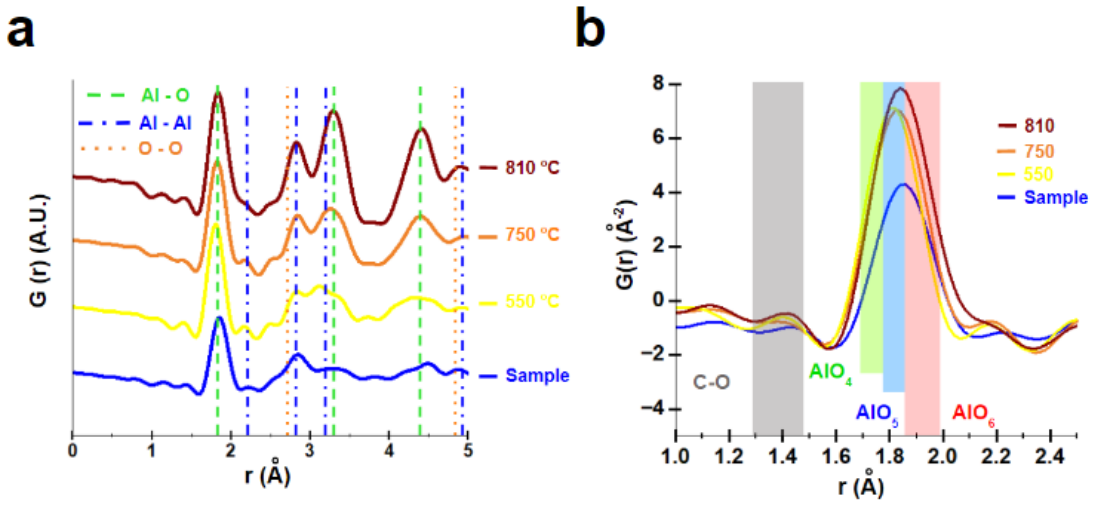

Figure 4.15) Comparison of PDF data at transition steps. a) Comparison of transition steps showing evolution of peak growth with respect to transition temperature. b) Comparison of transition steps showing evolution of Al-O bond pair peak with respect to transition temperature.

the ratio of the first and second transition steps being ~7.6 and ~8.2, respectively. Similarly to the XPS discussed in an earlier chapter, the ratio of Al-O and Al-Al peak area will also be dependent of the relative amount of each element in the composition.[107] In this case the AlO_x composition for the first two transition steps will have roughly twice the oxygen content of the final two transition steps—which results in a greater Al-O peak area. The increase between the first and second transition step coordination ratio is likely due to the C-O at ~1.4 Å creating an indiscernible cumulative increase in the Al-Al bond peak.

4.4 Structure-composition tailoring via LASiS parameters:

To study the experimentally tunable parameters of LASiS, we began by determining the O/Al ratio for the laser fluence at which we had made our initial AlO_x/C NCs discussed earlier. To analyze the AlO_x, a statistical EELS was undertaken wherein the Al to O ratio was estimated for ~25 different particles and compared to that of differing laser flux and pulse duration. Figure 4.16 shows TEM EELS spectra for the 5 ns laser comparing both ~0.15 and 0.2 J/cm^2/ns. After normalizing both spectra, the Al L_{23} edges showed similar relative intensity whereas the O K edges did not. The O K edge for the ~0.15 J/cm^2/ns case showed substantially more relative intensity; the calculated average scattering probability for the ~0.15 J/cm^2/ns case indicated a rough O/Al ratio of ~2.5 compared to the ~0.2 J/cm^2/ns case, which measured ~1.5. The Al L_{23} edge for the ~0.2 J/cm^2/ns case consequently also resembled Al_2O_3, with a peak at ~ 76.5eV.

Next, we investigated the tuning of the specific O to Al ratio for the AlO_x/C NCs. Initially, using two different pulse duration lasers, we set the energy density to match each other with the hypothesis that this was the driving force for the reactions needed to make the O to Al ratio. However, what we found was the resulting material was vastly different with O to Al ratios being higher in the 5 nanosecond case than the 9 nanosecond. We then went about matching the respective flux for each case instead, with the hypothesis being that it was the total amount of fluence dumped over time that is responsible for the production of the differing O to Al ratios. Following this assumption, in figure 4.17a, one can see that the general trend of both pulse durations matches with the highest relative O to Al ratio being around ~0.15 J/cm2/ns. Herein, our ongoing efforts are to correlate the O:Al ratio in the various tailored AlO_x compositions to the effective energetic properties of the respective ENM samples as measured by LASEM at the US ARL facilities. Figure 4.17b shows the result of changing the laser flux on the percent crystallinity for the AlO_x NCs. As discussed earlier, a small amount of parasitic crystalline Al forms during ablation which we have attributed to the higher energy regime in the center of the gaussian beam having enough fluence to blast off large chunks of Al. These large chunks do not take part in the

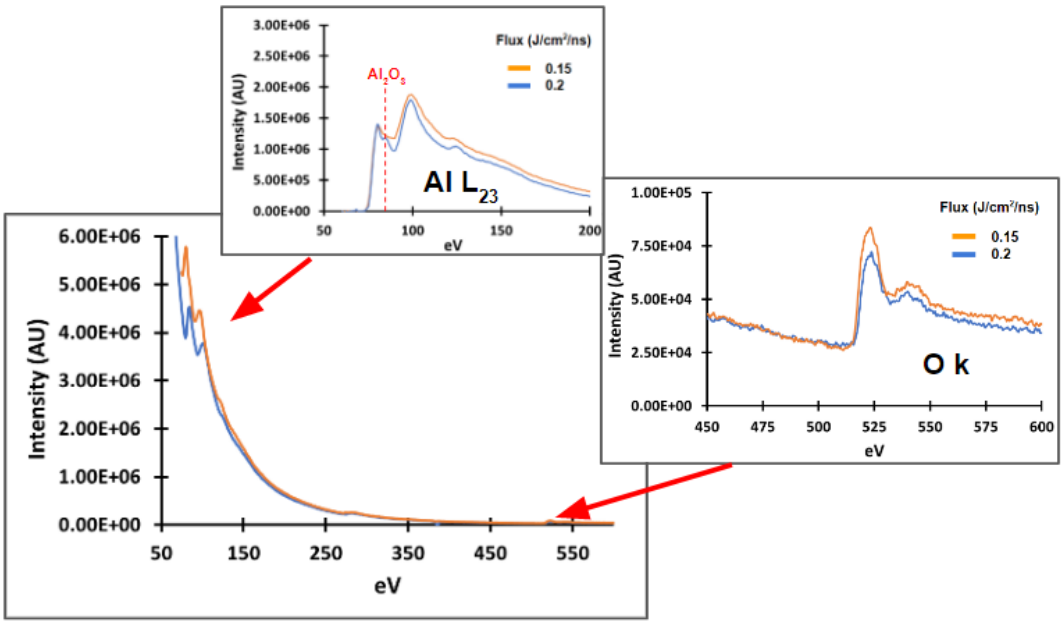

Figure 4.16) TEM EELS spectra for two separate energy densities showing a decrease in measured O/Al ratio when laser flux is increased.

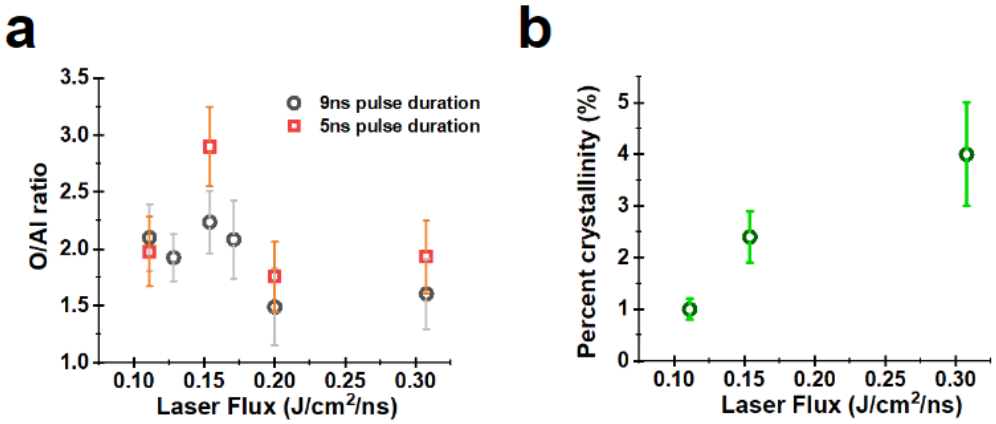

Figure 4.17) Tuning O/Al ratio and Al crystallinity using laser flux: a) Measured laser flux for two separate laser pulse durations vs the resulting O/Al ratios. b) Resulting Al crystallite percentage with differing laser flux.

plasma driven reactions that result in the AlO_x production and are rather just tossed into solution after cavitation bubble collapse. This parasitic crystalline Al phenomena seems to follow an arcing trend with more being produced as the flux increases due to a greater relative amount of the beam being above the critical chunking energy as the flux increases. We proposed that a hat top beam shaper could eliminate this parasitic crystalline Al production by spreading the high-power regime uniformly across the beam spot. This should also result in a smaller deviation of the resulting O/Al ratios allowing for greater tunability in the future. The extent of crystalline/amorphous structures for the final NPs can also be controlled by tuning solvent parameters since these structural arrangements also ensue once the particles exit the plume/cavitation bubble. Once the particles exit the cavitation bubble, they experience collisional growth until they reach a critical size and the liquid cooling or quenching takes place. The cooling times for the ensuing particles in the liquid will affect their crystallinity, with longer cooling times required for the nucleation and formation of crystallite planes. By tuning this cooling rate, it may be possible to not only control if the final NPs are crystalline or amorphous but also the specific type of crystallite phases the NPs form. This cooling rate may be tunable though the changing of both solvent density and temperature and hence, the choice of solvents (acetone, toluene, methanol, etc.).

Tunability and consistency between samples has long been a key issue with LASiS synthesis.[52,116] Bearing in mind figure 4.2, it is clear that the formation of the initial AlO_x clusters greatly depends on the input energy and resulting plasma temperature.[44,45] To address this problem, we wanted to implement a way to filter out low and high regions of laser flux. Typically, the laser in LASiS used for ablation is thought of as only a means of energy dumping to induce a high temperature plasma however, what we wanted to know was whether the profile of the laser beam played any role in the homogeneity of the NPs formed. The beam energy profile used for synthesis of the m-AlO_x NPs was a gaussian energy profile as shown in figure 4.18 (left). It can be seen that the energy varies drastically throughout the profile of the energy output, with the energy at the outer most edges being far too low to induce ablation-target coupling and the energy at the center of the beam being high enough for metal fracturing to occur, resulting primarily in the synthesis of pure Al NPs. At the relatively low flux that the AlO_x NPs are produced at, the plasma geometry functions more like a disk than a perfect sphere with high and low energy regions at the center and edge resulting from the gaussian energy profile. For this reason, we hypothesize that the correct energy for the synthesis of primarily AlO_x NPs is likely where the average flux across the greatest area of the gaussian energy profile resides. This means that the portion of the beam at the center and edges produce largely parasitic and undesirable contaminant structures resulting in the low homogeneity.

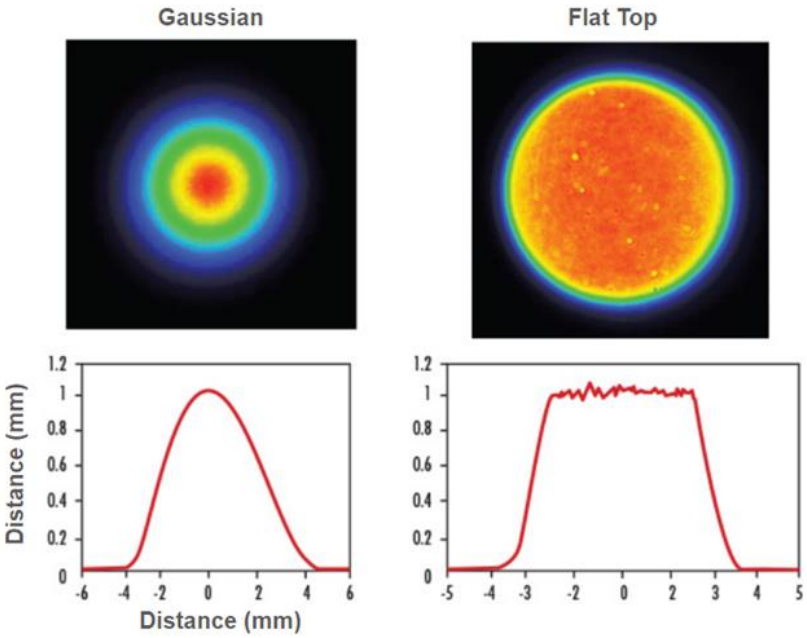

Figure 4.18) Gaussian vs Flat Top beam profile: Left) Gaussian input beam with gaussian power distribution across beam diameter. Right) Flat Top exit beam with a corrected average power equal across beam diameter.

Another key difference highlighted in figure 4.17a is a slight decrease in the measured average standard deviation between the 9 ns laser and the 5 ns laser O/Al ratio. The O/Al ratio was measured for roughly 25 different particles using HRTEM EELS at differing laser flux, and the standard deviation from the average O/Al ratio was calculated. The standard deviation for O/Al can be used to describe the homogeneity of the as-synthesized sample. What we noticed was that across nearly all sample cases, the 9 ns laser demonstrated a slightly lower average O/Al ratio standard deviation from an average of 0.32 to ~0.29 in the case of the 5 ns laser shown in figure 4.19. Upon closer inspection it was found that the power distribution of the 5 ns laser was significantly more gaussian than the 9 ns while in comparison the 9 ns had less centralized power distribution and had a more evenly distributed profile. This would support our earlier hypothesis, however, a more definitive study would be required. By introducing a flat top beam shaper into the laser beam line, the beam can be averaged out over the entire beam profile (figure 4.18 right) to a greater degree than what was observed in the 5 ns laser. The addition of the beam shaper should create a more even spread of flux resulting in an even spread of plasma temperature across the beam diameter. In turn, this even spread of plasma temperature should reduce the overall amount of undesirable contaminant structures and increase homogeneity throughout the samples, as discussed. A test case was synthesized at 0.15 J/cm^2/ns using the flat top beam shaper coupled with the gaussian 5 ns laser which resulted in a decrease in O/Al ratio standard deviation of ~ 43% from 0.35 to 0.2. However, although the standard deviation decreased, the average O/Al ratio also decreased from 2.9 to ~1.7. Although the increase in sample homogeneity did make for a good example of the hypothesis, it is likely that when using the beam shaper to alter the power distribution, the flux will also have to be increased to archive similar O/Al ratios as with the gaussian beam. More study will have to be conducted to find the right flux to compensate for this phenomenon.

4.5 Conclusion:

In conclusion, we have implemented HTXRD and HRTEM in analyzing the phase change of a metastable AlO_x NC to the slightly more globally stable alumina polymorph γ/θ-Al_2O_3. The premise for the phase change and the materials studied in this publication was briefly discussed in our previous publication. Using HRTEM EELS, we gathered spectral data for 5 separate NPs and compared their approximate O/Al atomic areal densities to calculated areal densities of Al_2O_3 of roughly the same size. The synthesized particles measured between 5 and 10 times less dense than standard Al_2O_3. The AlO_x/C NC was then examined using Isothermal XRD wherein the crystallization was tracked throughout time for temperatures ranging from 750^{o}C to 790^{o}C. The

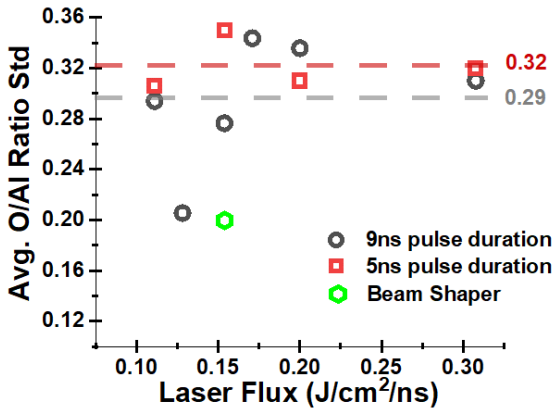

Figure 4.19) Tuning O/Al ratio standard deviation (Std) for 9 ns laser that demonstrated a lower Std across sampled NPs than the 5 ns laser. Flat top beam shaped decreased the standard deviation at 0.15 J/cm^2/ns

resultant phase extent of conversion was compared to known theoretical models with the tree dimensional constricting volume model matching best for all temperatures. Once linearized using the chosen model, the Arrhenius parameters were determined with the activation energy being significantly higher than that of similar sized Al particles. Using in-situ heating HRTEM to track the predicted shrinkage and visually confirm our model. During HRTEM heating the particle volumetric shrinkage ratio was measured to be roughly ~12 which was close to the volumetric density analysis which predicted that it would need to around 5 to 10 times smaller before being dense enough to crystalize to gamma alumina. Atomic Pair Distribution Function (PDF) analysis from x-ray scattering experiments were implemented to further understand the structural changes in metastable AlO_x NCs. Several transition steps were used to track the phase change including heating the NCs to ~550°C to eliminate carbon contamination, ~750°C for partial conversion, and ~810°C for full conversion to γ-Al_2O_3. The material's structure evolved from highly disordered to low-order polycrystalline as temperature increased. Changes in Al-O bonds indicated coordination shifts during each transition step which provided insights into the stability and structural changes of AlO_x nanocomposites during heating. We also demonstrated the tunability of the LASiS technique be altering the laser flux as well and pulse duration to archive differing Al to O ratios and percent crystallinity which is the first step to tuning the material's energetic behavior and amount of off gas during transition. Finally, we were able to increase the relative homogeneity of the synthesized material by implementing a flat top beam shape during ablation. The addition of the flat top beam shaper made for more uniform ablation and plasma conditions across the area of the beam, resulting in smaller deviation in measured O/Al ratios but also a decrease in overall O/Al ratio.

Chapter 5: Synthesis and structure-composition characterizations of other Fe and Al-based oxides/carbides/oxy-carbides synthesized via LASiS

Disclosure:

This chapter is adopted from a manuscript Submitted to Appl Surface Science 2023 (V658 P159682). The full list of authors includes: Elijah M. Davis, Erick L. Ribeiro, Saeed Kamali, Jianguo Wen, Charles Johnson, Jacqueline Johnson, Bamin Khomami, Dibyendu Mukherjee. The role of Elijah Davis was to design and perform all experiments, process and analyze all data, and prepare the manuscript for submission.

5.1 Introduction:

In our studies so far on the a-AlO_x nanostructures, extensive LASEM and TGA/DSC testing have indicated that while the a-AlO_x/C composites provide fast kinetics and energy release, they lack the long timescale heat release effects needed to function as effective solid fuels. To that end, the focus of the research presented in this chapter is directed toward exploring additional metal/ceramic (oxides, carbides, oxycarbides)-based ENMs that could be mixed with the pure Al or AlO_x composites to enable the tuning of their detonation/deflagration characteristics from high-speed detonation to large heat release. Specifically, we choose to focus here on the design and synthesis of known heat releasing thermite-based ENM reactions such as the Fe_2O_3/Al oxidation-reduction (redox) reaction and the oxidation of metal-carbides. The Fe_2O_3/Al redox reaction has been used throughout the energetics community for quite some time now. Based on the results presented in the previous chapters on the AlO_x system, one can assume that the phase transition reactions for the AlO_x/C NCs result in fast energy release manifested through the concurrent trapped gas release, rather than heat release as with most energetic materials. With this in mind, the goal here is to take advantage of the fast kinetics of AlO_x phase decomposition releasing oxidative gases (O_2, CO_2 etc), while interfacing them with parasitic Al as solid fuel, to promote chain reactions between the Al/Fe_2O_3 redox reaction and other Fe-carbide oxidation reactions. Using AlO_x and metal carbides to initiate the ignition of the propellent would facilitate a series of redox reactions between Al and Fe_2O_3 which would then generate sufficient heat and ignition energy to accelerate the otherwise sluggish Fe carbide to Fe_2O_3 oxidation reaction. These reactions will theoretically prompt a rapid energy release, followed by prolonged heat release. Similarly, Al-based carbides (Al_4C_3) have also been studied heavily throughout the past few decades as a method of producing prolonged heat release ENMs due to their increased energy density. The main problem that researchers encountered when implementing Al_4C_3 as ENMs though was the immense energy required to activate carbides-based ENMs. Oxycarbides

however are substantially less stable, can exist in amorphous and metastable states with varying Al:C:O compositions, and are in turn less difficult to activate. Mixing Al oxycarbides with the AlO_x NCs could enable the cascading initiation via AlO_x followed by the ignition and heat release via Al based oxycarbide/carbide NCs; albeit, to the best of our knowledge, such hypotheses have not been extensively tested through rigorous experiments. Additionally, the high dielectric strengths of carbides/oxycarbides and the well-known magnetic properties of Fe-oxides/carbides could further facilitate their activations via alternating magnetic field-induced heating using RF/microwave coupling without the need for direct thermal heating that can be beneficial for easy and safe deployment of munitions.

Hence, to test the hypothesis for the energetic behaviors of such metal/ceramic-interfaced metastable ENMs, we synthesized composite Fe_2O_3/Fe-carbide and Al oxycarbide NPs with tailored structure-composition properties that could pave the path for the next-generation of metastable ENMs for future weapons/munitions development. Fe-carbide NPs are well-known magnetic nanomaterials (MNMs) that can generate heat when subjected to directed alternating magnetic field to induce ignition rather than conventional electric or open flame stimulus. Interestingly, for the same reason, MNMs are also at the forefront of current medical research for a wide range of applications, ranging from magnetic hyperthermia (MHT) to thermally activated drug delivery for cryopreservation of transplant organs thereby finding civilian applications[117,118]. MHT could hold promise as a possible future cancer treatment of localized tumors, which would otherwise be difficult via current conventional methods. At the nanoscale, confined electronic interactions in magnetic materials lead to unique size/morphology-dependent properties such as superparamagnetism.[50,51] Iron (Fe) and Fe oxide-based NPs have been extensively studied in the past decade for their applications as MNMs owing to their well-known magnetic activities. While pristine unoxidized Fe and Fe-carbide remain amongst the materials comprising the highest magnetic activities, the magnetic properties of Fe-oxide are relatively weak.[50,119] Thus, Fe-carbides are an alluring alternative to Fe and Fe-oxide MNMs due to certain complementary characteristics, including high melting points and chemical stability, along with high saturation magnetization (~140 emu/g), dielectric constants,[119] and strong corrosion resistance. Added to this, the presence of the C-atoms endows them with significant mechanical strength and chemical inertness, while allowing these structures to exhibit carbon-related near-infrared (NIR) light-responsive performances. Specifically, Fe-carbide nanostructures are able to convert the absorbed light energy into ultrasound and heat under near-infrared irradiation, which in turn can be immediately extended to photoacoustic tomography (PAT), and photothermal therapy (PTT) applications.[120]

However, most ultra-small (<10-15 nm) Fe-carbide NPs are inherently difficult to synthesize and stabilize, since the majority of the synthetic routes require high temperature and high pressure conditions; moreover, once prepared, it is difficult to suppress the surface oxidation of the Fe-carbide layers to Fe-oxides.[50,121] To that end, the stabilization and passivation of the nanostructured Fe/Fe-carbide cores are of paramount importance to maintain its functionality. Specifically, core–shell NPs have received a great deal of interest in recent years. This interest includes a number of different types of core–shell NPs that range from native oxide shell formation on a parent metal to hybrid alloy shells and more recently carbonaceous glassy or graphitic shells.[29] In the case of native oxide shells, some passivation of the parent metal at the core can be achieved, however multiple shortcomings accompany this type of core-shell structure. Oxide core–shell NPs often result in a large ratio of the total volume consisting of an inert oxide, depending upon the shell thickness, and relatively low chemical stability due to oxygen diffusion through the shell.[122,123] It is for this reason that alternatives to oxide shell type core–shell NPs are in high demand throughout a plethora of scientific fields. Alternatives are, hence, shell types capable of limiting oxygen diffusion and providing high chemical stability, while protecting the core material. Glassy or graphitic shell core–shell NPs provide an attractive alternative to oxide shells due to their high chemical stability combined with such traits as low diffusion, high electron transfer and possible surface functionalization. Currently, few chemical synthesis routes exist that are capable of producing such glassy or graphitic shell type core-shell NPs reliably to allow their implementations in the aforesaid studies.[124] Some of the more common methods employed for MNM syntheses include liquid-phase chemical syntheses, hydrothermal routes and thermal decomposition processes, that are typically capable of producing MNMs with superior size and compositional control, thereby making them the preferred routes for the synthesis of Fe-oxides such as Fe_3O_4.[125,126] However, the former methods are limited to production of equilibrium or near-equilibrium oxides and incapable of synthesizing the Fe@C and Fe_3C@C structures, as aimed in this work.

To that end, this study has employed our patented in-house LASiS technique in the ablation of a Fe target submerged in organic solvent liquid medias to synthesize various core-shell Fe@Fe_2O_3, Fe@C and Fe_3C@C NPs as effective MNMs[68,127]. Recent years have seen a surge in the use of LASiS for the facile and rapid synthesis of various metal/metal oxide and composite NPs with varying structures and compositions due to its ease of use and tunability. In the past, we have successfully demonstrated the versatility of LASiS in synthesizing diverse classes of complex nanomaterials; these include intermetallic/metal oxide nanocomposites/nanoalloys,[59,69,70,128-130] metal-organic frameworks (MOFs),[62] and MOF-derived

hybrid NCs[61] as electrocatalysts and supercapacitor materials as well as more recently, C-coated Al[29] and amorphous Al-oxide in a metastable and hyperoxidized state (AlO_x; x>1.5)[107] as energetic additives and solid-state gas generators. Yet, only a handful of past studies have been conducted using LASiS to produce both Fe@Fe_2O_3 and Fe@C graphitic shell-Fe core NPs with most relying on liquid-phase ablation containing metal salt precursors in a solution rather than the simultaneous target ablation and laser-induced solvent pyrolysis, as described in this work.[131,132] The latter method allows for easy scale-up for bulk production of MNMs, while enabling interfacial carbon passivation due to the laser ablation of metal targets being able to nucleate large amounts of NPs, whose surfaces then act as seeding sites for heterogenous nucleation of carbon structures from the laser-induced pyrolysis of organic solvents. Of the few reports, past studies have observed some similar Fe-oxide/Fe-carbide structures have also been observed using laser ablation of Fe targets in ethanol with the mechanism for the formation of these nanostructures being attributed to the ultra-high temperature of the laser-induced plasma combined with the carbon from the solvent and a lack of oxygen.[63,133,134] Once synthesized the particles' magnetic response is typically judged in a number of ways including visually with a simple magnetic response method or ^{57}Fe Mössbauer spectroscopy.[132,135,136] Mössbauer spectroscopy becomes an important tool for such studies as it can not only be used to determine if there are magnetic structures present but it can also, through identification of magnetic hyperfine patterns, be used to determine the specific Fe species.[137-139]

5.2 Fe oxide and Fe carbide results and discussion:

Detailed TEM image shown in figure 5.1a provides a direct visualization of the sample synthesized via LASiS using acetone as the solvent choice. It was observed that the sample consists of 20 - 40 nm spherical nanoparticles (NPs) dispersed in a carbonaceous matrix along with smaller amorphous (< 4nm) NPs embedded throughout. Upon closer inspection, high-resolution TEM in figure 5.1c indicates that the large particles in question are core-shell structures with the core being crystalline coated by an amorphous shell. The outer shell consists of iron oxide, most likely indicating the formation of Fe@Fe_2O_3 core@shell NPs with no graphitic or glassy carbon planal lines found within the shell. SAED patterns shown in figure 35b, for the area depicted in figure 5.1a, indicate the presence of both FCC and BCC Fe structures.

In the case of toluene used as the solvent (figure 5.2), the synthesized NPs indicate a clear change in their sizes and structures with a large number of amorphous NPs residing in the smaller 2-10 nm size ranges. Additionally, it was noted that the large pure Fe@Fe_2O_3 core–shell NPs

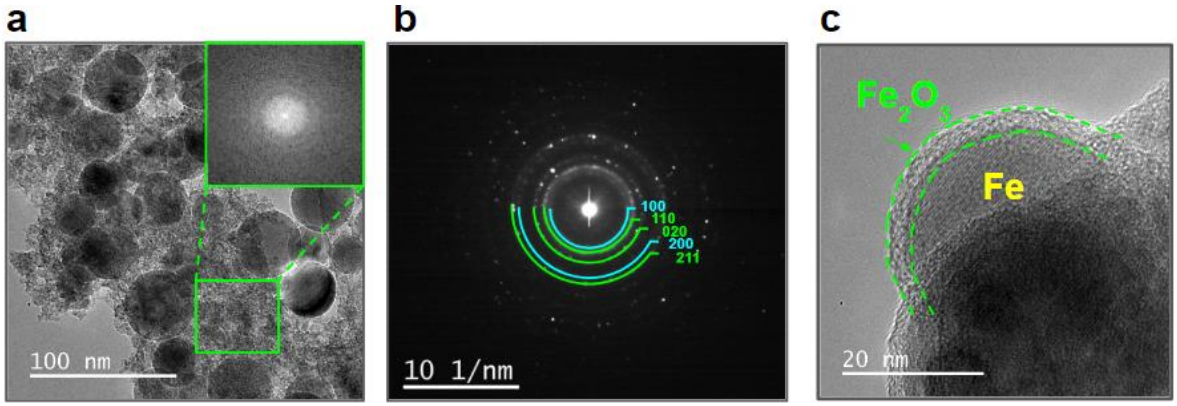

Figure 5.1) TEM examination of the Fe in acetone case. a) large field view of overall particle distribution with FFT of smaller amorphous particles. b) SAED of particle distribution shown in (a). with blue indicating BCC and green indicating FCC structures. c) Crystalline Fe particle found during closer inspection.

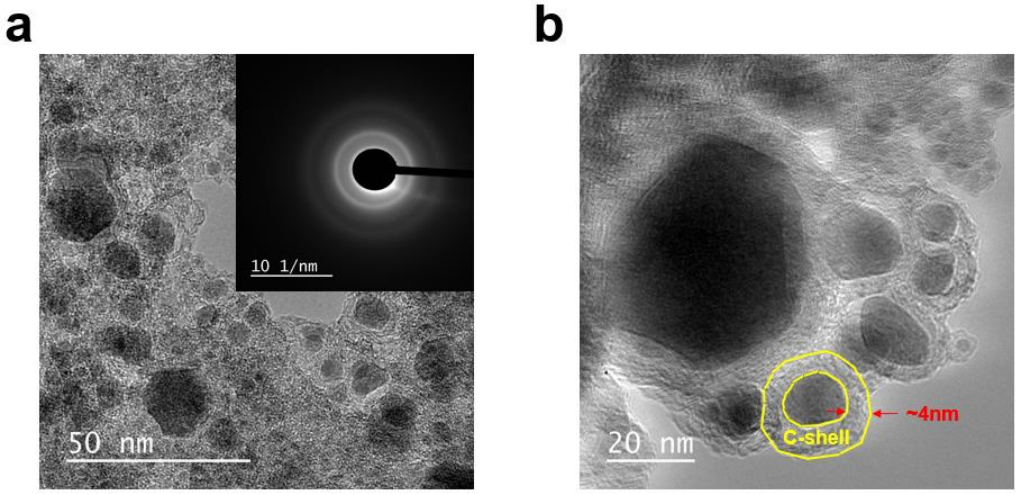

Figure 5.2) TEM examination of the Fe in non-heated toluene case. a) large field view of overall particle distribution; inset is amorphous SAED of particle distribution shown in (a). b) Amorphous Fe particle with ~4 nm thick carbon shell.

responsible for the crystalline SAED patterns were not present in this case as compared to the previous sample synthesized in acetone. The particles produced in the toluene seemed to exhibit two distinct ranges in terms of their size distribution, namely (i) large 20-40 nm amorphous NPs and (ii) small 2-10 nm amorphous particles (figure 5.2a). The larger size regime particles were coated in thick (~ 4 nm) non-ordered glassy carbon shells instead of the Fe_2O_3 shells seen in the previous sample (figure 5.2b). The smaller size regime NPs were again embedded in a carbon matrix.

In an effort to increase the crystallinity and concentration of graphitic shell coated Fe NPs, the same synthesis process was carried out via LASiS under toluene heated during the ablation process to an equilibrium temperature of ~95°C. By adjusting this parameter, the hypothesis was that the increased solvent temperature would promote rapid formation of carbonaceous products, leading to an excess formation of graphitic shells on the NPs due to heterogeneous nucleation arising from the rapid pyrolysis of the organic solvent.[29,140,141] This rapid pyrolysis of the solvent is likely to be a result of beam interactions during its travel through the solvent.[140,142] The results of this parameter change indicate that LASiS of the Fe targets under heated toluene leads to the production of large quantities of a polymerized carbon matrix (PCM) entirely engulfing the produced NPs seen in figure 5.3a and figure 5.3b. The production of this polymerized film is not unexpected as similar structures have been obtained by LASiS performed without a metallic seed target.[140,142] The Fe-based NPs produced in heated toluene consisted of two separate size ranges: large 20-40 nm particles, as well as small agglomerations of ultra-small (< 5 nm) amorphous particles, similar to the ambient toluene case. However, our initial hypothesis that the increase in solvent temperature would lead to an increase in the amount of crystallinity within the NPs due to longer coarsening times during equilibration in the solvent is not substantiated. Investigations using localized SAED measurements, as shown in figure 5.3b (inset), yielded negligible effect in crystallinity making it difficult to determine the exact core composition of the shell-core NPs. A notable difference observed between the two toluene cases was an increase in the ordering and average thickness of the carbon coating with most particles having a coating thickness of around 5 nm, as shown in figure 5.3a. This would indicate that solvent temperature has a significant implication of the type of carbon shell formed and the extent of ordering.

To provide a more in-depth investigation into the structure of the as-synthesized NPs, we utilized X-ray diffraction (XRD) with a Co X-ray source to reduce the fluorescence. As shown in figure 5.4a, for the syntheses carried out under acetone at ambient temperature conditions, the resulting XRD pattern indicated purely amorphous structures. For the samples prepared under

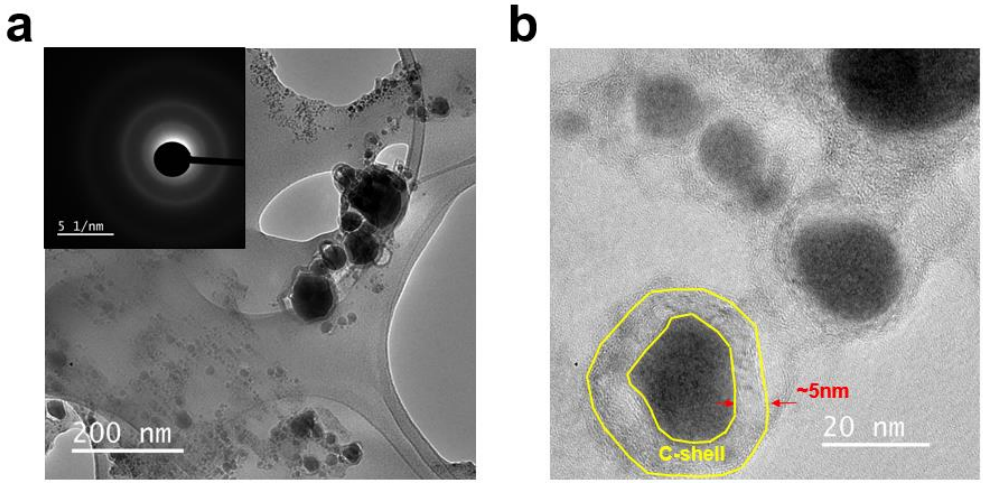

Figure 5.3) TEM examination of the Fe in heated toluene case. a) large field view of overall particle distribution engulfed in a polymerized carbon matrix; inset is amorphous SAED of particle distribution shown in (a). b) Amorphous Fe particle with ~5 nm thick carbon shell.

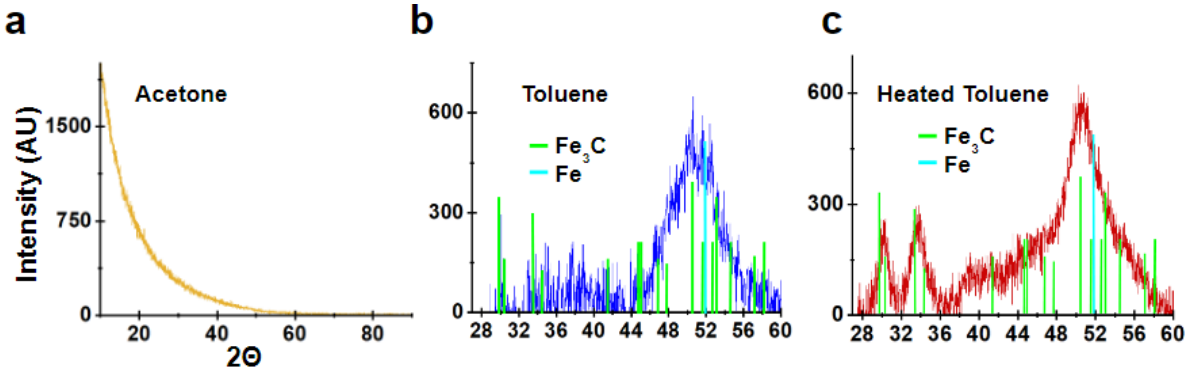

Figure 5.4) XRD of the Fe samples for all three cases using a cobalt source to reduce florescence. a) Acetone Fe case showing no relative crystallinity. b) Non-heated toluene Fe case showing possible peaks for both Fe_3C and Fe structures c) Heated toluene Fe case showing possible peaks for both Fe_3C structures as well as Fe.

toluene, the XRD patterns in figures 5.4b-c indicate a broad distribution of weak peaks of crystalline iron carbide structures along with the possible presence of minor amounts of crystalline Fe. It should be noted that the peaks for Fe_3C and Fe_2C, as well as Fe_7C_3 and Fe_5C_2, can all provide possible matches as a result of the broadened peak centered at ~ 50.5° 2θ. This made it slightly more challenging to conclusively determine the exact compositions of the composite nanostructures synthesized here. With this in mind, one plausible explanation for the low intensity broad peak for the XRD in figures 5.4b-c for the toluene samples could be either the size or degree of crystallinity of mixed Fe-carbide (Fe_xC_y) particles. Specifically, this could be attributed to the size of the larger Fe-carbide particles (~20 nm) or, the particles in question being polycrystalline in nature with small discontinuous measurable crystallites.[143-146] One notable difference between the heated and non-heated toluene cases was the visible sharpening of the broad ~ 50.5° 2θ peak as well as the emergence of two additional peaks at ~ 30° and 34° 2θ. This is likely due to an increase in measurable crystalline Fe-carbide in the heated toluene case.

For further inspection of these mixed Fe-carbide/Fe-oxide structures, TEM EELS was utilized for possible identification of known near-edge structures from the investigated particles. The EELS spectra for the ultra-small NPs, shown in figure 5.5a, present a residual carbon peak coordination which is similar to that of amorphous carbon, indicating that these NPs are not coated by a graphitic-type shell and rather only encapsulated by the carbon-based polymer matrix. In the case of the larger particles, shown in figure 5.5b, the carbon EELS spectrum arrangement exhibited similar characteristic π* and σ* peaks to that of hydrogenated diamond-like carbon reported from graphitic coatings.[88,89] The L_3 to L_2 ratio for Fe in the smaller particles (figure 5.5a) was found to be slightly lower than that reported for regular amorphous Fe_2O_3 at ~3.9.[147-151] However, upon further inspection of the O K-edge EELS spectrum for the same particle, both peaks a* and b* were present indicating the characteristic peaks for amorphous Fe_2O_3 within the smaller particles.[152] In contrast, the O K-edge EELS spectrum for the larger particle shown in figure 5.5b confirmed a complete lack of oxygen within the particle with the ~532 eV window being completely void of any residual O peak. Additionally, the L_3 to L_2 ratio for the Fe-edge spectrum for the larger particles are calculated to be ~2.5, which is similar to previously reported value for pure Fe EELS spectra.[147-151]

Finally, to assess the magnetic response of the as-synthesized nanocomposite samples for their application as MNMs, we carried out a series of ^{57}Fe Mössbauer spectroscopy measurements; this aided us in investigating the phase compositions for each of the as-synthesized composite Fe cases. All centroid shifts, δ, are given with respect to metallic α-iron at

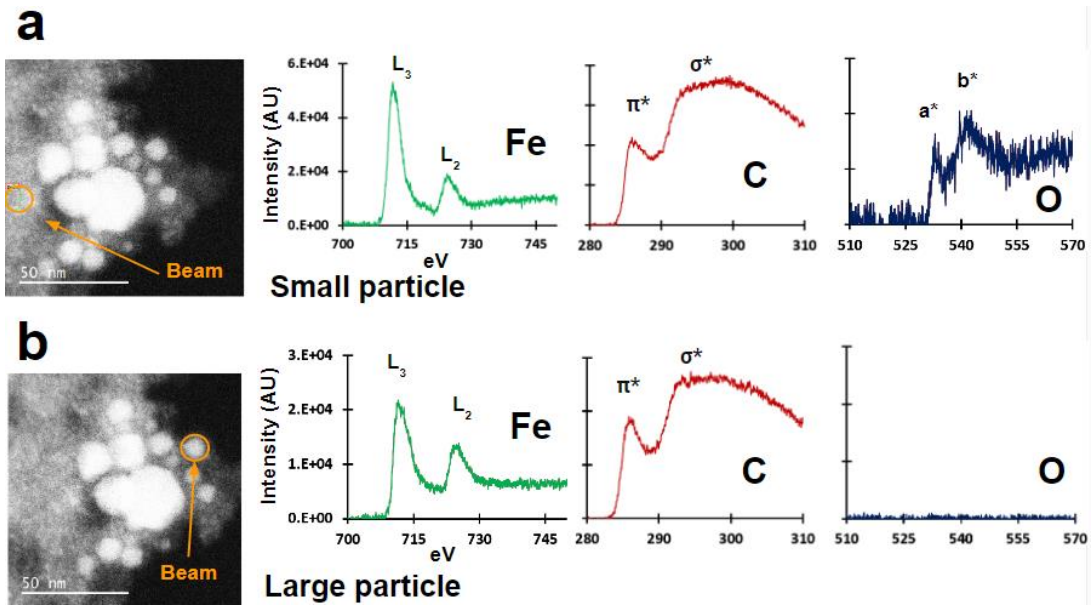

Figure 5.5) TEM EELS elemental analysis of the heated toluene case. a) EELS analysis of the Fe, C, and O spectral peaks for a chosen within the large regime of ~40 nm. b) EELS analysis of the Fe, C, and O spectral peaks for a chosen within the small regime of <5 nm.

room temperature. The Mössbauer spectra for the acetone case indicates an unresolved two-line pattern, which is best fitted with two doublets, as shown in figure 5.6a. The hyperfine parameters for both doublets are characteristic for that of a high spin Fe^{3+} from Fe-oxide structures, closely resembling γ-Fe_2O_3 phase.[153,154] The spectrum for the samples synthesized under toluene at room-temperature and heated conditions, as indicated in figures 5.6b & c respectively, are best fit with one singlet, one doublet, and two sextets. The singlet, having a δ value of -0.08 mm/s, is most probably the signal from Fe atoms in the austenite phase (FCC),[155,156] while the doublet had characteristic values for high spin Fe^{3+} with an intensity <15%. This is likely the amorphous structures seen in both the toluene and heated toluene cases. The first sextet indicated a B_{hf} value of close to 33 T and a δ value close to 0.0 mm/s (seen in table 5.1). This component most reasonably could be from unreacted Fe clusters.[157,158] Finally, the second sextet had a B_{hf} value of around 21 T and a δ value of 0.19 mm/s. This signal is most plausibly from an Fe_3C compound, as reported earlier.[137,159] The finding of these Fe_3C compounds correspond with the earlier XRD findings for the two toluene samples which concluded that the relative percentage of crystalline Fe-carbide structures, when compared to the amorphous phases in the material, was very low when detected using XRD, suggesting some form of semi-crystalline or amorphous Fe-carbides was also present. This might also suggest that some of the amorphous structures shown earlier in figures 5.2b and 5.3b may in fact be carbon-doped as a result of the carbon shell formations. For the samples synthesized under heated toluene, the relative magnetic responses from Fe-based compounds indicate an increase from ~60 to ~70%. This increase in magnetic response is due to an increase in the relative intensity of the Fe-carbide type compounds, from the ~40 % wt. (unheated toluene samples) to ~53% wt. (heated toluene samples). This increase in potential Fe_3C-type compounds could be a result of the increase in graphitic shell thickness seen in figure 5.3b as well as the presence of the PCM acting as a protective coating against the formation of $Fe@Fe_2O_3$ core–shell particles. The remaining ~26% and ~17%, in the toluene and heated toluene cases respectively, consisted of Fe oxide structures likely from the smaller size regime discussed earlier.

Figure 5.7 shows both the NC samples prepared under toluene and acetone measured at varying temperatures of 295 K and 6 K with table 5.2 displaying the applied hyperfine parameters at 6 K for both samples. Interestingly, the toluene sample shown in figures 5.7a & b indicated little variation in the Mössbauer response with change in temperature, however the acetone case (figures 5.7c&d) demonstrated a significant change in the hyperfine structure. Herein, the hyperfine parameters corresponding to Q_2 and Q_3 components arise from the ultra-small (<4-5nm) Fe-oxide NPs in a superparamagnetic state.[135] The next two components are most probably

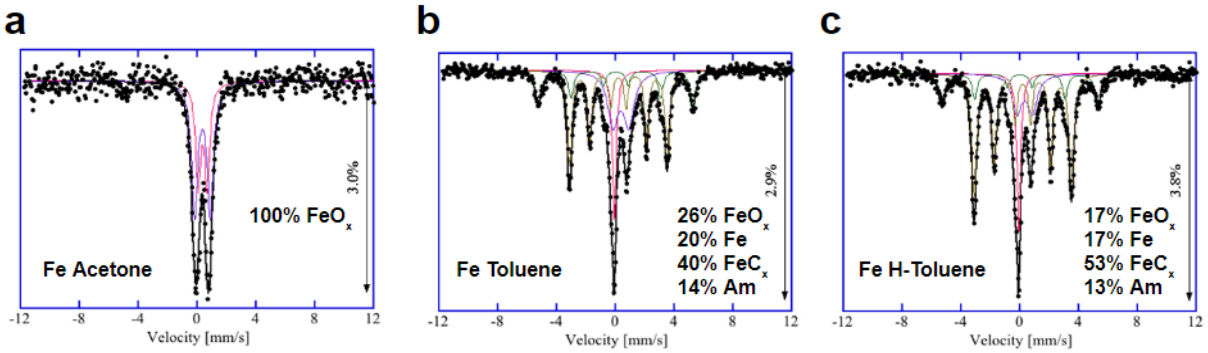

Figure 5.6) ^{57}Fe Mössbauer spectroscopy measured at room-temperature of Fe ablated in acetone (a), Fe ablated in toluene (b), and Fe ablated in heated toluene.

Table 5.1) ^{57}Fe Mössbauer spectroscopy hyperfine parameters measured at ambient temperature.

	Components	Q_1	Q_2	Q_3	Q_5	Q_{5a}
Acetone	δ (mm/s)		0.36	0.35		
	ε/(ΔE_Q) (mm/s)		0.62	1.06		
	B_{hf} (T)					
	Γ (mm/s)		0.42	0.50		
	I (%)		39	61		
Toluene	δ (mm/s)	-0.08		0.36	0.01	0.19
	ε/(ΔE_Q) (mm/s)			1.08	0.00	0.00
	B_{hf} (T)				32.6	20.7
	Γ (mm/s)	0.31		0.85	0.37	0.32
	I (%)	14		26	20	40
Heated Toluene	δ (mm/s)	-0.08		0.31	0.00	0.19
	ε/(ΔE_Q) (mm/s)			1.04	0.01	0.01
	B_{hf} (T)				32.9	20.6
	Γ (mm/s)	0.30		0.80	0.36	0.33
	I (%)	13		17	17	53

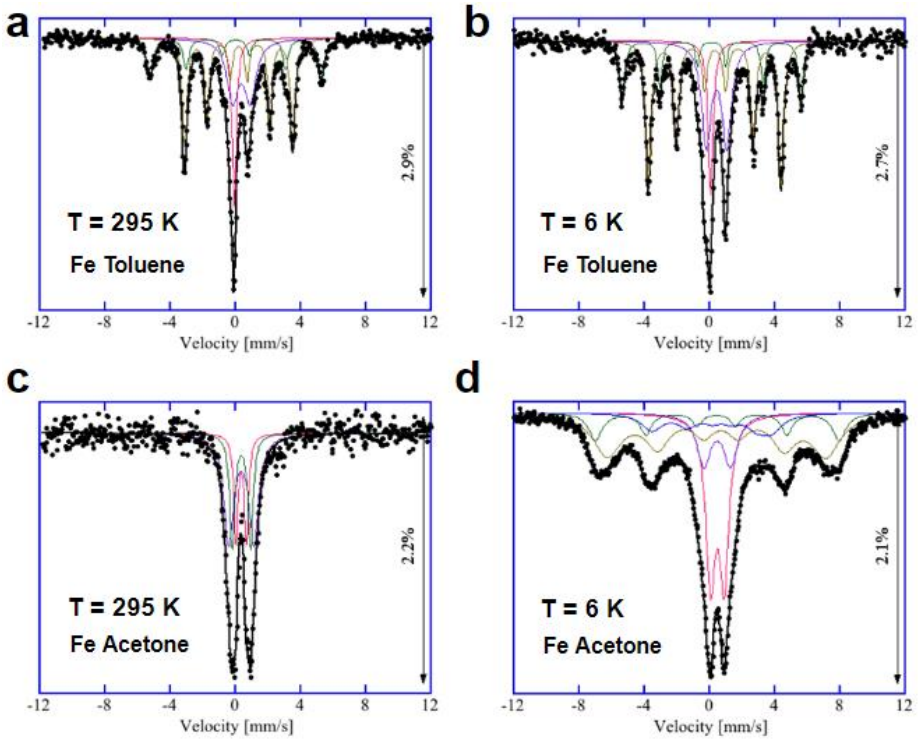

Figure 5.7) ^{57}Fe Mössbauer spectroscopy measured at both ambient temperature and 6K for comparison. Fe ablated in toluene measured at 295 K (a), Fe ablated in toluene measured at 6K (b), Fe ablated in acetone measured at 295 K (c), Fe ablated in acetone measured at 6K (d).

Table 5.2) ^{57}Fe Mössbauer spectroscopy hyperfine parameters measured at 6 K temperature.

	Components	Q_1	Q_2	Q_3	Q_5	Q	Q
Acetone	δ (mm/s)		0.47	0.46	0.43	0.55	0.43
	ε/(ΔE_Q) (mm/s)		0.84	1.64	0.03	-0.13	-0.32
	B_{hf} (T)				46.4	41.6	22.8
	Γ (mm/s)		0.71	1.02	0.70	1.49	1.29
	I (%)		26	11	12	39	12
Toluene	δ (mm/s)	0.05		0.42	0.11	0.32	
	ε/(ΔE_Q) (mm/s)			1.25	0.00	0.00	
	B_{hf} (T)				34.0	25.2	
	Γ (mm/s)	0.37		0.71	0.29	0.39	
	I (%)	11		28	18	43	

maghemite in a magnetically blocked state. This change in magnetic response is likely due to the relaxation in the superparamagnetic state due to lowering the temperature. This is in contrast to the toluene cases, indicating the resultant particles for the acetone case show a large amount of pure Fe with some percentage of Fe_2O_3 iron-oxide, likely from the smaller size regime identified in the TEM EELS. However, with the lack of such peaks appearing in the toluene case, it would seem the smaller size regime particles are too low in concentration to warrant such a response. Based on the aforesaid detailed materials characterizations at different length scales, we could currently conclude that the high-energy laser plasma driven non-equilibrium LASiS-based synthesis route plausibly results in a complex Fe-oxide/Fe-carbide nanocomposite. Furthermore, LASiS carried out under heated toluene results in considerable graphitic C-shells on the NPs.

5.3 Aluminum Oxycarbide and Aluminum carbide results and discussion:

Similar to the work done with Fe, in an effort to increase the concentration of crystalline Al in the samples for use as the solid fuel component within our fuel/oxidizer mixes, differing solution temperatures were examined. As with the Fe_2O_3/Fe-carbide containing cascade reaction discussed earlier, the theory behind the mixing of our AlO_x NC with an Al-carbide solid fuel could enable an initial ignition from the AlO_x NCs followed by a small amount of heat release from the parasitic Al, this time from both the AlO_x NC as well as the Al carbide NC, which would be enough to ignite the Al carbide and in turn provide a form of prolonged heat release. The synthesis of the Al carbide NC intended for use as solid fuel additives to our AlO_x NC will be discussed throughout the following section.

Figure 5.8 shows XRD for differing temperatures and solvents. For the acetone cases, when the temperature of the solvent was dropped significantly below ambient temperature to ~ 0^{o}C, the amount of crystalline aluminum produced appears to decrease with barely any intensity remaining. Although the exact concentration of crystallinity was not measured, by comparing similar samples we can qualitatively say that a very small amount of crystallinity is present in the low temperature acetone case because of the vast decrease in peak intensity. In the case of the heated acetone (~ 80 ^{o}C) the amount of visible crystallinity was again low. One notable difference between the two samples was the emergence of a graphite peak in the lower 2θ range for the heated acetone case. This would indicate an increase pyrolysis of the organic solvent at increased temperatures.[29,140,141] For the samples prepared using toluene as the liquid, all three showed varying amounts of Al-carbide formation with the heated toluene case displaying the most

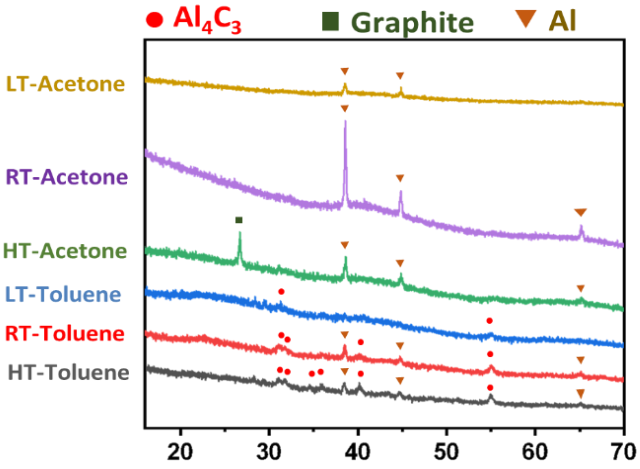

Figure 5.8) XRD for Al made under differing LASiS temperatures.

prominent XRD peaks. Our earlier hypothesis discussed in the Fe work above still holds, with an increase in solvent temperature leading to an increase in the amount of crystallinity within the NPs due to longer coarsening times during equilibration in the solvent. We can also see that in the case of both the heated and ambient temperature toluene, some pure crystalline Al is still produced.

At this point our focus becomes tasked on the production of a sample that will best complement the AlO_x ENMs, enabling a large amount of trapped heat release for a prolonged period when ignited by the AlO_x NCs. Carbides deliver excellent heat conductivity as well as slow, controlled heat release, making them an ideal option for the task at hand. We focused on the heated toluene case due to its notable amount of Al-carbide. Using HR-TEM for closer inspection of the heated toluene case we could see in figure 5.9 that the sample consisted largely of ~10 - 30 nm pristine Al-carbide particles with a measured interatomic spacing of ~0.28 nm. Additionally, the Al-carbide NPs in question were coated in up to 4 nm of graphitic shells. In a previous work we demonstrated that these shells could protect and enable increase reactivity due to the immense internal pressures release upon ignition.[29]

Upon closer inspection via TEM EELS mapping shown in figure 5.10, we can see that not all of the particles examined for the heated toluene case consisted of pure Al-carbide. In the case of the NP shown in figure 5.10, the elemental mapping depicts an elemental composition of ~ 25 – 30 % Al, ~ 60 – 65 % O, and ~ 10 – 20 % C—indicating the presence of both Al-carbide as well as some form of Al oxycarbide.

5.4 Conclusion:

We have reported the use of LASiS under both acetone and toluene to synthesize $Fe@Fe_2O_3$ core–shell NPs as well as glassy carbon coated $Fe_3C@C$ NPs. For both solvents used, the synthesized materials showed little to no crystalline Fe with NPs residing in two separate size regimes namely, larger 20-40 nm core-shell structures of $Fe@Fe_3O_4$ and $Fe_3C@C$ NPs along with ultra-small amorphous NPs, mostly in the 2-10 nm size range. In all cases, the smaller size regime particles could only be identified as some form of mixed FeO_x composites. Specifically, LASiS carried out under acetone as the solvent mainly resulted in $Fe@Fe_2O_3$ core–shell NPs with maghemite (γ-Fe_2O_3) as the dominant iron oxide structures. In contrast, ablation carried out under toluene as the solvent produced largely core-shell NP structures comprising Fe_3C cores coated by several glassy carbon shells ($Fe_3C@C$). To investigate the effect of solvent temperatures on the formation of Fe_3C-type structures and carbon shell formation, LASiS was carried out under toluene heated up to ~95 ^oC resulting in an increase in Mössbauer response for Fe_3C structures

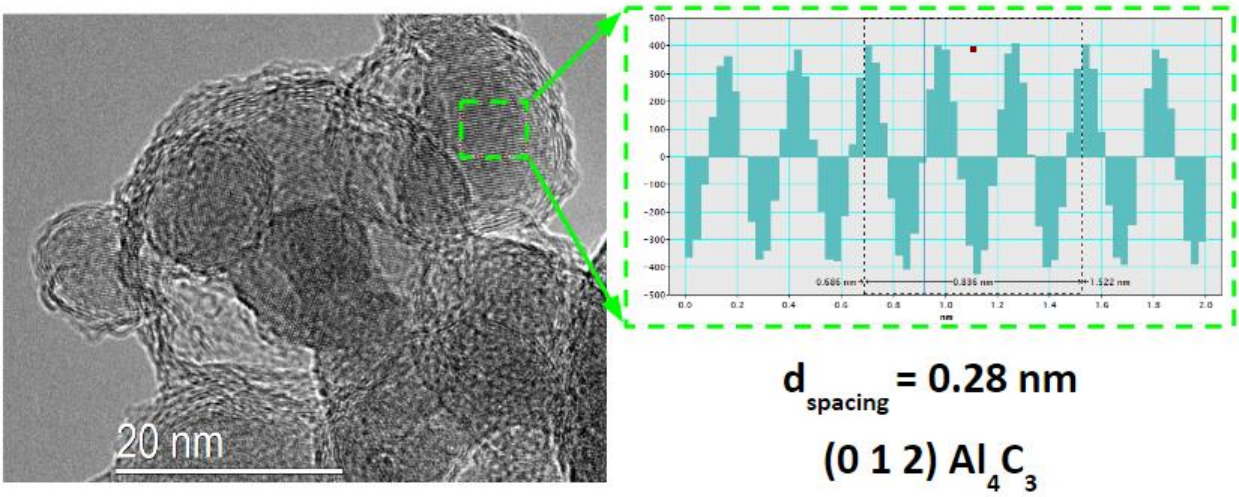

Figure 5.9) HRTEM showing highly crystalline Al4C3 with glassy C-shell coatings.

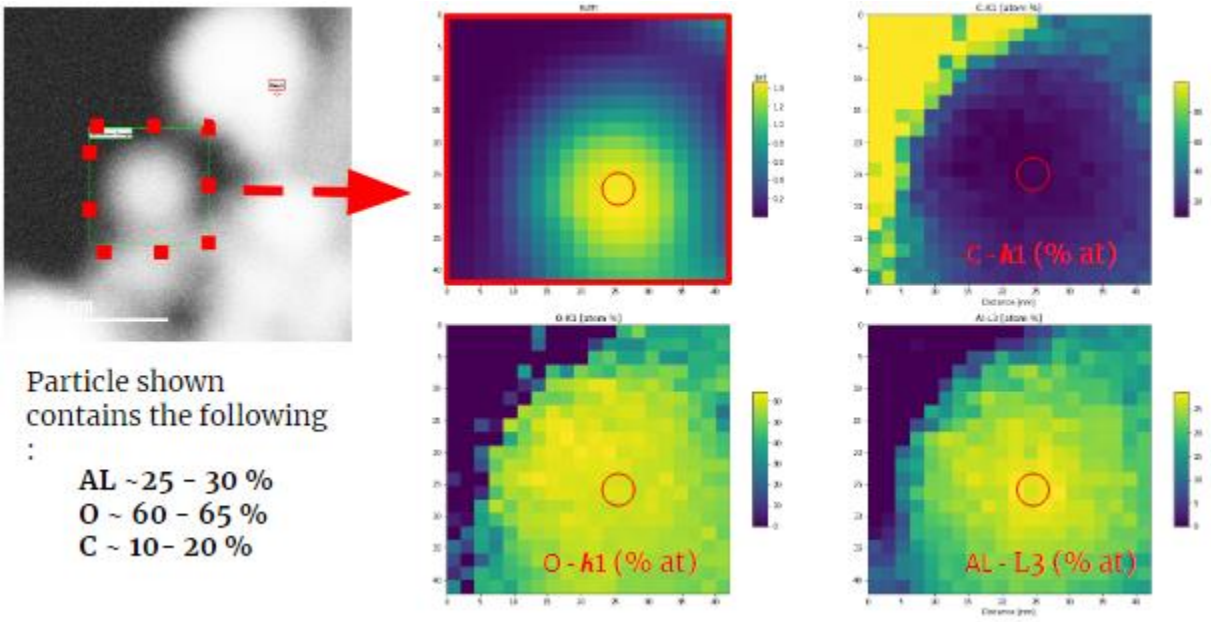

Figure 5.10. HRTEM EELS mapping for oxycarbide Al particle.

as well as an increase in glassy carbon shell thicknesses. The hyperfine parameters from Mossbauer spectroscopy indicated doublets for samples synthesized under acetone that were characteristic of a high spin Fe^{3+} from γ-Fe_2O_3 phases. In contrast and concurrent to our observations from structural characterizations, the Mossbauer spectral data for the samples prepared under toluene (both heated and room temperature conditions) indicated a singlet, a doublet, and two sextet peaks. These were characteristics of mixed compositions comprising pure Fe atoms in austenite phase (FCC), high spin Fe^{3+} (<15%) from small amorphous Fe-oxide structures as well as, significant amounts of Fe_3C structures—especially for the heated toluene case study. Herein, the glassy carbon shells not only passivate the core Fe_3C structures, thereby protecting them from surface oxidation during their application as potential MNM materials, but also provide the necessary non-toxic and biocompatible coating for medical applications. Additionally, such coatings paired with strong magnetic properties make them an ideal material for the magnetic activation of ENMs. Finally, we also discussed the synthesis of similar Al-based carbides as well as Al-based oxycarbides using similar techniques.

Chapter 6: Summary and Future Outlook

6.1 Summary of Work Throughout:

This work presents a comprehensive study on the synthesis, stabilization, and potential applications of metastable nanostructured metal-oxide phases, with a focus on hyperoxidized aluminum nanocomposites. Throughout the research, LASiS technique is employed as an innovative synthesis method to overcome the longstanding challenges in kinetically trapping and stabilizing such non-stoichiometric and amorphous Al-oxide structures at the nanoscale. LASiS involves a high-energy laser to thermally vaporize liquid-confined metal targets, creating extremely high temperature and pressure plasma plumes. These conditions result in the formation of NPs within a cavitation bubble, which are subsequently quenched and stabilized upon exiting and rapidly cooling in the surrounding liquid. Using the LASiS technique we were able to kinetically trap amorphous metastable hyper-oxidized AlO_x nanostructures that are uniquely phase-stabilized in carbonaceous matrices. Specifically, rapid energy dumping and liquid-phase quenching during LASiS has enabled the metastable freezing of highly disordered and amorphous a-AlO_x ($2.5< x \leq 3.5$) NPs (<5-10 nm sizes) within a laser-pyrolyzed C monolayer. The presence of this interfacial carbon monolayer around the NPs was shown to provide a crucial role in stabilizing these disordered structures exhibiting remarkable stability at elevated temperatures until undergoing solid-solid phase change (SS-PC) at temperatures exceeding 750°C. During SS-PC, the a-AlO_x NCs first transition to γ/θ–Al_2O_3 then eventually form stable α-Al_2O_3 while releasing excess trapped gases like O_2 and CO_2. High-temperature XRD (HTXRD) and Atomic Pair Distribution Function (PDF) analysis were used to understand the structural changes in metastable AlO_x NCs. Isothermal HTXRD was performed, wherein the crystallization was tracked and compared to known theoretical models with the three dimensional constricting volume model matching best for all temperatures. PDF analysis from x-ray scattering experiments throughout multiple transition steps were used to track the phase change to γ-Al_2O_3, during which the material's structure evolved from highly disordered to low-order polycrystalline as temperature increased. Changes in Al-O bonds indicated coordination shifts during each transition step provided insights into the stability and structural changes of AlO_x nanocomposites during heating. The potential tunability of the LASiS technique was also shown to achievable through altering the laser flux and pulse duration, resulting in differing Al to O ratios and percent crystallinity—which is the first step to tuning the material’s energetic behavior and amount of off gassing during the solid-solid phase transition. The ability to kinetically trap and stabilize these metastable nanomaterials has significant implications for their potential use as solid-state gas generator additives. These materials can bypass the diffusion limitations typically associated with first-generation aluminum-based energetic nanomaterials.

Additionally, the work also explores the synthesis of other Fe/Al-based carbides, oxides, and oxycarbides, which demonstrate promising properties as functional additives and oxidizers for solid fuels. We reported the use of LASiS under both acetone and toluene to synthesize $Fe@Fe_2O_3$ core–shell NPs as well as glassy carbon coated $Fe_3C@C$ NPs. For both solvents used, the synthesized materials showed little to no crystalline Fe with NPs residing in two separate size regimes, namely, larger 20-40 nm core-shell structures of $Fe@Fe_3O_4$ and $Fe_3C@C$ NPs along with ultra-small amorphous NPs, mostly in the 2-10 nm size range. Specifically, LASiS carried out under acetone as the solvent mainly resulted in $Fe@Fe_2O_3$ core–shell NPs with maghemite (γ-Fe_2O_3) as the dominant iron oxide structures. In contrast, ablation carried out under toluene as the solvent, the NPs produced were largely core-shell structures comprising Fe_3C cores coated by several glassy carbon shells ($Fe_3C@C$). LASiS carried out under toluene heated to ~95 ^oC resulted in an increase in Fe_3C structures as well as an increase in glassy carbon shell thicknesses. Mossbauer spectroscopy indicated characteristics of mixed compositions comprising pure Fe atoms in austenite phase (FCC), high spin Fe^{3+} (<15%) from small amorphous Fe-oxide structures as well as significant amounts of Fe_3C structures, especially for the heated toluene case study. Herein, the glassy carbon shells not only passivate the core Fe_3C structures, thereby protecting them from surface oxidation during their application as potential MNM materials, but also provide the necessary non-toxic and biocompatible coating for medical applications. Additionally, such coatings paired with high magnetic properties make them an ideal material for the magnetic activation of ENMs. Finally, we also discussed the synthesis of similar Al-based carbides as well as Al-based oxycarbides using similar techniques. TEM elemental mapping depicts an elemental composition of ~ 25 – 30 % Al, ~ 60 – 65 % O, and ~ 10 – 20 % C, indicating the presence of both Al-carbide as well as some form of Al oxycarbide. By implementing the kinetically-trapped metastable a-AlO_x phase with excess of trapped oxygen as an activator/oxidizer additive in the metal/ceramic systems, we could designing a composite fuel-activator/oxidizer mix. The result is a lowered activation energy and eliminating the need for an additional oxidizer material, thereby lowering the volume of solid propellants and delivering a higher energy density material for advanced rocket propulsion delivery systems. The research described paves the way for future investigations into other such metastable nanomaterials awaiting discovery in the non-equilibrium phase space and presents a significant advancement in the field of materials science. The ability to kinetically trap and stabilize such metastable nanomaterials has the potential for applications not just as solid-state gas generator additives and energetic materials, but a host of other technologies awaiting discovery and research in the future.

6.2 Proposed Work and Future Outlook:

The initial work that has been conducted in this study including HTXRD, SS-NMR, and X-ray scattering PDF delivers an excellent starting knowledge for these materials, however it is nothing but the tip of the iceberg for properties that were not explored. One suggestion would be the further identification of PDF peaks using neutron scattering paired with computational methods such as Density Functional Theory (DFT) and molecular dynamics simulations to predict and validate the experimental findings. These models could help in understanding the stabilization pathways of metastable materials and aid in the possible design of new nanocomposites.

The finding of the single monolayer carbon skin around each nano particle was a surprising solution to the otherwise cryptic explanation as to how such metastable materials could exist in nature. Using neutron scattering paired with computational methods could greatly evolve our understanding of this phenomenon and further shed light on its rule in the material's bond arrangements and stabilization mechanism. A key suggestion would be in-situ LIBS to probe into the plasma during real-time LASiS operation to extract the evolution (birth and death) of various chemical species during the process paired with machine learning techniques to analyze large datasets from experiments and simulations, identifying patterns and optimizing synthesis protocols. This would allow for real time analysis of the plasma conditions that result in the synthesis of these metastable materials. Additionally, implementing Gas chromatography (GC) measurements to estimate the amount of oxidative gas (O_2, CO_2, etc.) released from the a-AlO_x samples upon their disorder-order phase transition would be very helpful for a stoichiometric O-balance. Chapter 4 discussed the tuning of the disorder and Al to O ratio using the laser fluence and beam shapers, utilizing GC we will also be able to quantifiably provide additional data beyond that of the statistical EELS for tuning the structure-composition properties of the a-AlO_x/C NCs. The GC measurements for each of the samples produced under different laser flux conditions will be correlated to the Al:O ratio in each sample to demonstrate the trend in oxygen production when the off gas is measured during their phase transition at ~750-800 °C. This will allow us to optimize material synthesis for the maximum disorder to order transition and off gas amount. Furthermore, the amount of oxidative trapped gas release from the a-AlO_x phase transition will provide the necessary data for the stoichiometric O-balance in the ENM formulations for the Al-AlO_x (fuel-oxidizer) mixes for complete and efficient oxidation.

One of the main purposes of this work was to showcase the methods and techniques that could be easily applied to other such metastable oxide phases. The potential application for leveraging the unique structural and energetic properties of these other metastable oxide phases

could be innumerable. Other application areas for the metastable NCs in technological areas beyond energetic materials include unique battery technologies, memory storage devices, and materials for neuromorphic computing, to name a few. Finally, the current small-scale batch by batch synthesis process for the bench-top LASiS set-up can only produce these materials in small amounts (<100 mg/batch) that needs to be significantly scaled up for these metastable materials technologies to find industrial-scale implementation in real-world scenarios. At the current scales of material production, it would be valuable to partner with the niche industries in advanced materials manufacturing to translate our laboratory findings into commercial products, thereby ensuring that the research has a tangible impact on technology and society in the future. These recommendations aim to enhance the understanding and practical use of metastable nanostructured materials, driving innovation in materials science and engineering. The proposed research could be used to address fundamental challenges and unlock the full potential of LASiS-synthesized metastable NCs, pushing the boundaries of what is possible with metastable nanostructured materials and unlocking new opportunities across various scientific and technological fields.

References

1 Richards, R. & Bonnemann, H. in *Nanofabrication Towards Biomedical Applications* (ed Josef Hormes Challa S. S. R. Kumar, Carola Leuschner) (Wiley-VCH, 2005).

2 Alivisatos, A. P. Semiconductor clusters, nanocrystals, and quantum dots. *science* **271**, 933-937 (1996).

3 Brus, L. E. Electron–electron and electron-hole interactions in small semiconductor crystallites: The size dependence of the lowest excited electronic state. *The Journal of chemical physics* **80**, 4403-4409 (1984).

4 van der Heijden, A. E. D. M. *et al.* Processing, application and characterization of (ultra)fine and nanometric materials in energetic compositions. *Aip Conf Proc* **845**, 1121-1126 (2006).

5 Park, K., Lee, D., Rai, A., Mukherjee, D. & Zachariah, M. R. Size-resolved kinetic measurements of aluminum nanoparticle oxidation with single particle mass spectrometry. *Journal of Physical Chemistry B* **109**, 7290-7299, doi:10.1021/jp048041v (2005).

6 Dreizin, E. L. Metal-based reactive nanomaterials. *Progress in Energy and Combustion Science* **35**, 141-167, doi:10.1016/j.pecs.2008.09.001 (2009).

7 El-Sayed, M. A. Some interesting properties of metals confined in time and nanometer space of different shapes. *Accounts of chemical research* **34**, 257-264 (2001).

8 An, K. & Somorjai, G. A. Size and Shape Control of Metal Nanoparticles for Reaction Selectivity in Catalysis. *ChemCatChem* **4**, 1512-1524, doi:https://doi.org/10.1002/cctc.201200229 (2012).

9 Sun, W. *et al.* The thermodynamic scale of inorganic crystalline metastability. *Science advances* **2**, e1600225 (2016).

10 Rondinone, A. J., Pawel, M., Travaglini, D., Mahurin, S. & Dai, S. Metastable tetragonal phase CdWO4 nanoparticles synthesized with a solvothermal method. *Journal of colloid and interface science* **306**, 281-284 (2007).

11 Zhou, X., Torabi, M., Lu, J., Shen, R. & Zhang, K. Nanostructured Energetic Composites: Synthesis, Ignition/Combustion Modeling, and Applications. *ACS Appl. Mater. Interfaces* **6**, 3058-3074, doi:10.1021/am4058138 (2014).

12 Prakash, A., McCormick, A. V. & Zachariah, M. R. Tuning the reactivity of energetic nanoparticles by creation of a core-shell nanostructure. *Nano Lett.* **5**, 1357-1360, doi:10.1021/nl0506251 (2005).

13 Mukherjee, D., Rai, A. & Zachariah, M. R. Quantitative laser-induced breakdown spectroscopy for aerosols via internal calibration: Application to the oxidative coating of aluminum nanoparticles. *Journal of Aerosol Science* **37**, 677-695, doi:10.1016/j.jaerosci.2005.05.005 (2006).

14 Mukherjee, D., Wang, M. & Khomami, B. Impact of particle morphology on surface oxidation of nanoparticles: A kinetic Monte Carlo based study. *Aiche Journal* **58**, 3341-3353, doi:10.1002/aic.13740 (2012).

15 Xu, F. *et al.* Superior reactivity of ferroelectric Bi2WO6/aluminum metastable intermolecular composite. *Chemical Engineering Science* **247**, 116898, doi:https://doi.org/10.1016/j.ces.2021.116898 (2022).

16 Sun, J., Pantoya, M. L. & Simon, S. L. Dependence of size and size distribution on reactivity of aluminum nanoparticles in reactions with oxygen and MoO3. *Thermochimica Acta* **444**, 117-127, doi:https://doi.org/10.1016/j.tca.2006.03.001 (2006).

17 Wang, H., Kline, D., Rehwoldt, M., Biswas, P. & Zachariah, M. in *AIAA SCITECH 2022 Forum AIAA SciTech Forum* (American Institute of Aeronautics and Astronautics, 2021).

18 Prakash, A., McCormick, A. V. & Zachariah, M. R. Synthesis and reactivity of a super-reactive metastable intermolecular composite formulation of Al/KMnO4. *Adv Mater* **17**, 900-+ (2005).
19 Xu, J. *et al.* Controlling the energetic characteristics of micro energy storage device by in situ deposition Al/MoO3 nanolaminates with varying internal structure. *Chemical Engineering Journal* **373**, 345-354, doi:https://doi.org/10.1016/j.cej.2019.04.205 (2019).
20 Park, K., Lee, D., Rai, A., Mukherjee, D. & Zachariah, M. R. Size-Resolved Kinetic Measurements of Aluminum Nanoparticle Oxidation with Single Particle Mass Spectrometry. *The Journal of Physical Chemistry B* **109**, 7290-7299, doi:10.1021/jp048041v (2005).
21 Davari, S. A. & Mukherjee, D. Kinetic Monte Carlo simulation for homogeneous nucleation of metal nanoparticles during vapor phase synthesis. *AIChE Journal* **64**, 18-28, doi:10.1002/aic.15887 (2018).
22 Li, Y., Kalia, R. K., Nakano, A. & Vashishta, P. Size effect on the oxidation of aluminum nanoparticle: Multimillion-atom reactive molecular dynamics simulations. *Journal of Applied Physics* **114**, 134312, doi:10.1063/1.4823984 (2013).
23 Wu, B. *et al.* Fast reaction of aluminum nanoparticles promoted by oxide shell. *Journal of Applied Physics* **126**, 144305, doi:10.1063/1.5115545 (2019).
24 Rai, A., Park, K., Zhou, L. & Zachariah, M. R. Understanding the mechanism of aluminium nanoparticle oxidation. *Combustion Theory and Modelling* **10**, 843-859, doi:10.1080/13647830600800686 (2006).
25 Mukherjee, D., Prakash, A. & Zachariah, M. R. Implementation of a discrete nodal model to probe the effect of size-dependent surface tension on nanoparticle formation and growth. *Journal of Aerosol Science* **37**, 1388-1399, doi:https://doi.org/10.1016/j.jaerosci.2006.01.008 (2006).
26 Mukherjee, D., Sonwane, C. G. & Zachariah, M. R. Kinetic Monte Carlo simulation of the effect of coalescence energy release on the size and shape evolution of nanoparticles grown as an aerosol. *The Journal of Chemical Physics* **119**, 3391-3404, doi:10.1063/1.1580098 (2003).
27 Chowdhury, S., Sullivan, K., Piekiel, N., Zhou, L. & Zachariah, M. R. Diffusive vs Explosive Reaction at the Nanoscale. *J. Phys. Chem. C* **114**, 9191-9195, doi:10.1021/jp906613p (2010).
28 Pantoya, M. L. *et al.* in *Defense Applications of Nanomaterials* Vol. 891 *ACS Symposium Series* Ch. 16, 227-240 (American Chemical Society, 2005).
29 Davari, S. A. *et al.* Graphitic coated Al nanoparticles manufactured as superior energetic materials via laser ablation synthesis in organic solvents. *Applied Surface Science* **473**, 156-163 (2019).
30 Kappagantula, K. S., Farley, C., Pantoya, M. L. & Horn, J. Tuning Energetic Material Reactivity Using Surface Functionalization of Aluminum Fuels. *The Journal of Physical Chemistry C* **116**, 24469-24475, doi:10.1021/jp308620t (2012).
31 Wieszczycka, K. *et al.* Surface functionalization – The way for advanced applications of smart materials. *Coordination Chemistry Reviews* **436**, 213846, doi:https://doi.org/10.1016/j.ccr.2021.213846 (2021).
32 Ke, X. *et al.* Surface functionalized core/shell structured CuO/Al nanothermite with long-term storage stability and steady combustion performance. *Materials & Design* **140**, 179-187, doi:https://doi.org/10.1016/j.matdes.2017.11.068 (2018).
33 Sun, J. & Simon, S. L. The melting behavior of aluminum nanoparticles. *Thermochimica Acta* **463**, 32-40, doi:10.1016/j.tca.2007.07.007 (2007).
34 Henz, B. J., Hawa, T. & Zachariah, M. R. On the role of built-in electric fields on the ignition of oxide coated nanoaluminum: Ion mobility versus Fickian diffusion. *Journal of Applied Physics* **107**, 024901, doi:10.1063/1.3247579 (2010).

35 Sun, W. *et al.* The thermodynamic scale of inorganic crystalline metastability. *Science Advances* **2**, e1600225, doi:10.1126/sciadv.1600225.
36 Stein, A., Keller Steven, W. & Mallouk Thomas, E. Turning Down the Heat: Design and Mechanism in Solid-State Synthesis. *Science* **259**, 1558-1564, doi:10.1126/science.259.5101.1558 (1993).
37 Gopalakrishnan, J. Chimie douce approaches to the synthesis of metastable oxide materials. *Chemistry of Materials* **7**, 1265-1275 (1995).
38 Li, Z. *et al.* Aluminum Oxide Nanoparticle Films Deposited from a Nonthermal Plasma: Synthesis, Characterization, and Crystallization. *ACS Omega* **5**, 24754-24761, doi:10.1021/acsomega.0c03353 (2020).
39 Scaramuzza, S., Agnoli, S. & Amendola, V. Metastable alloy nanoparticles, metal-oxide nanocrescents and nanoshells generated by laser ablation in liquid solution: influence of the chemical environment on structure and composition. *Physical Chemistry Chemical Physics* **17**, 28076-28087, doi:10.1039/c5cp00279f (2015).
40 Fallahi, A., Guldentops, G., Tao, M., Granados-Focil, S. & Van Dessel, S. Review on solid-solid phase change materials for thermal energy storage: Molecular structure and thermal properties. *Applied Thermal Engineering* **127**, 1427-1441, doi:https://doi.org/10.1016/j.applthermaleng.2017.08.161 (2017).
41 Blatter, A. & von Allmen, M. Reversible Amorphization in Laser-Quenched Titanium Alloys. *Physical Review Letters* **54**, 2103-2106, doi:10.1103/PhysRevLett.54.2103 (1985).
42 Raj, C. R., Suresh, S., Bhavsar, R. R. & Singh, V. K. Recent developments in thermo-physical property enhancement and applications of solid solid phase change materials. *Journal of Thermal Analysis and Calorimetry* **139**, 3023-3049, doi:10.1007/s10973-019-08703-w (2020).
43 Pogatscher, S., Leutenegger, D., Schawe, J. E. K., Uggowitzer, P. J. & Löffler, J. F. Solid–solid phase transitions via melting in metals. *Nature Communications* **7**, 11113, doi:10.1038/ncomms11113 (2016).
44 Lam, J., Amans, D., Dujardin, C., Ledoux, G. & Allouche, A.-R. Atomistic Mechanisms for the Nucleation of Aluminum Oxide Nanoparticles. *The Journal of Physical Chemistry A* **119**, 8944-8949, doi:10.1021/acs.jpca.5b05829 (2015).
45 Hai, P. & Wu, C. A comparative DFT study of the oxidation of Al crystals and nanoparticles. *Physical Chemistry Chemical Physics* **23**, 24004-24015, doi:10.1039/D1CP03241K (2021).
46 Brower, K. L. Structural and Trapping Characteristics of a New Al Defect in Vitreous Silica. *Physical Review Letters* **41**, 879-881, doi:10.1103/physrevlett.41.879 (1978).
47 Laurens, G., Amans, D., Lam, J. & Allouche, A.-R. Comparison of aluminum oxide empirical potentials from cluster to nanoparticle. *Physical Review B* **101**, 045427, doi:10.1103/PhysRevB.101.045427 (2020).
48 Thakur, P., Sharma, V. & Thakur, N. Study of energy release in Fe2O3/Al nano-thermite with graphene as an additional fuel. *Physica B: Condensed Matter* **610**, 412803, doi:https://doi.org/10.1016/j.physb.2020.412803 (2021).
49 Xu, J. *et al.* Tuning the Ignition Performance of a Microchip Initiator by Integrating Various Al/MoO3 Reactive Multilayer Films on a Semiconductor Bridge. *ACS Applied Materials & Interfaces* **9**, 5580-5589, doi:10.1021/acsami.6b14662 (2017).
50 Zhu, K. *et al.* Magnetic Nanomaterials: Chemical Design, Synthesis, and Potential Applications. *Accounts of Chemical Research* **51**, 404-413, doi:10.1021/acs.accounts.7b00407 (2018).
51 Ma, Z., Mohapatra, J., Wei, K., Liu, J. P. & Sun, S. Magnetic Nanoparticles: Synthesis, Anisotropy, and Applications. *Chemical Reviews* **123**, 3904-3943, doi:10.1021/acs.chemrev.1c00860 (2023).

52 Liang, S.-X., Zhang, L.-C., Reichenberger, S. & Barcikowski, S. Design and perspective of amorphous metal nanoparticles from laser synthesis and processing. *Physical Chemistry Chemical Physics* **23**, 11121-11154, doi:10.1039/d1cp00701g (2021).
53 Mukherjee, D. Compositions, systems and methods for producing nanoalloys and/or nanocomposites using tandem laser ablation synthesis in solution-galvanic replacement reaction. US patent (2019).
54 Mukherjee, D. Compositions, systems and methods for producing nanoalloys and/or nanocomposites using tandem laser ablation synthesis in solution-galvanic replacement reaction. US patent (2021).
55 Hu, S., Melton, C. & Mukherjee, D. A facile route for the synthesis of nanostructured oxides and hydroxides of cobalt using laser ablation synthesis in solution (LASIS). *Phys. Chem. Chem. Phys.* **16**, 24034-24044, doi:10.1039/c4cp03018d (2014).
56 Hu, S. *et al.* A facile and surfactant-free route for nanomanufacturing of tailored ternary nanoalloys as superior oxygen reduction reaction electrocatalysts. *Catalysis Science & Technology* **7**, 2074-2086, doi:10.1039/c7cy00073a (2017).
57 Hu, S. *et al.* Correction: A facile and surfactant-free route for nanomanufacturing of tailored ternary nanoalloys as superior oxygen reduction reaction electrocatalysts. *Catalysis Science & Technology* **7**, 3163-3163, doi:10.1039/c7cy90063e (2017).
58 Hu, S., Goenaga, G., Melton, C., Zawodzinski, T. A. & Mukherjee, D. PtCo/CoO x nanocomposites: Bifunctional electrocatalysts for oxygen reduction and evolution reactions synthesized via tandem laser ablation synthesis in solution-galvanic replacement reactions. *Applied Catalysis B: Environmental* **182**, 286-296, doi:10.1016/j.apcatb.2015.09.035 (2016).
59 Hu, S., Tian, M., Ribeiro, E. L., Duscher, G. & Mukherjee, D. Tandem laser ablation synthesis in solution-galvanic replacement reaction (LASiS-GRR) for the production of PtCo nanoalloys as oxygen reduction electrocatalysts. *Journal of Power Sources* **306**, 413-423, doi:10.1016/j.jpowsour.2015.11.078 (2016).
60 Hu, S. *et al.* Hybrid nanocomposites of nanostructured Co3O4 interfaced with reduced/nitrogen-doped graphene oxides for selective improvements in electrocatalytic and/or supercapacitive properties. *RSC Advances* **7**, 33166-33176, doi:10.1039/c7ra05494g (2017).
61 Ribeiro, E. L. *et al.* MOF-derived PtCo/Co3O4 nanocomposites in carbonaceous matrices as high-performance ORR electrocatalysts synthesized via laser ablation techniques. *Catalysis Science & Technology* **11**, 3002-3013, doi:10.1039/d0cy02099k (2021).
62 Ribeiro, E. L., Davari, S. A., Hu, S., Mukherjee, D. & Khomami, B. Laser-induced synthesis of ZIF-67: a facile approach for the fabrication of crystalline MOFs with tailored size and geometry. *Materials Chemistry Frontiers* **3**, 1302-1309, doi:10.1039/C8QM00671G (2019).
63 Amendola, V. & Meneghetti, M. What controls the composition and the structure of nanomaterials generated by laser ablation in liquid solution? *Phys. Chem. Chem. Phys.* **15**, 3027-3046, doi:10.1039/c2cp42895d (2013).
64 Amendola, V. *et al.* Coexistence of plasmonic and magnetic properties in Au89Fe11 nanoalloys. *Nanoscale* **5**, 5611-5619, doi:10.1039/C3NR01119D (2013).
65 Yang, G. W. Laser ablation in liquids: Applications in the synthesis of nanocrystals. *Progress in Materials Science* **52**, 648-698, doi:https://doi.org/10.1016/j.pmatsci.2006.10.016 (2007).
66 Amendola, V. & Meneghetti, M. Laser ablation synthesis in solution and size manipulation of noble metal nanoparticles. *Physical Chemistry Chemical Physics* **11**, 3805-3821, doi:Doi 10.1039/B900654k (2009).

67 Miotello, A. & Kelly, R. Laser-induced phase explosion: new physical problems when a condensed phase approaches the thermodynamic critical temperature. *Applied Physics a-Materials Science & Processing* **69**, S67-S73, doi:10.1007/s003399900296 (1999).
68 Mukherjee, D. & Hu, S. Compositions, Systems and Methods for Producing Nanoalloys, and/or Nanocomposites using tandem Laser Ablation Synthesis in Solution-Galvanic Replacement Reaction. USA patent US 10,326,146 B2 (2019).
69 Hu, S., Goenaga, G., Melton, C., Zawodzinski, T. A. & Mukherjee, D. PtCo/CoOx nanocomposites: Bifunctional electrocatalysts for oxygen reduction and evolution reactions synthesized via tandem laser ablation synthesis in solution-galvanic replacement reactions. *Applied Catalysis B: Environmental* **182**, 286-296, doi:http://dx.doi.org/10.1016/j.apcatb.2015.09.035 (2016).
70 Hu, S., Melton, C. & Mukherjee, D. A facile route for the synthesis of nanostructured oxides and hydroxides of cobalt using laser ablation synthesis in solution (LASIS). *Physical Chemistry Chemical Physics* **16**, 24034-24044 (2014).
71 Gottfried, J. L. Laboratory-Scale Method for Estimating Explosive Performance from Laser-Induced Shock Waves. *Propellants, Explosives, Pyrotechnics* **40**, 674-681, doi:https://doi.org/10.1002/prep.201400302 (2015).
72 Gottfried, J. L. & Bukowski, E. J. Laser-shocked energetic materials with metal additives: evaluation of chemistry and detonation performance. *Appl. Opt.* **56**, B47-B57, doi:10.1364/AO.56.000B47 (2017).
73 Esposito, V. & Castelli, I. E. Metastability at defective Metal oxide interfaces and nanoconfined structures. *Advanced Materials Interfaces* **7**, 1902090 (2020).
74 Liu, C. *et al.* A Metastable Crystalline Phase in Two-Dimensional Metallic Oxide Nanoplates. *Angewandte Chemie* **131**, 2077-2081 (2019).
75 Huang, J.-C. *et al.* A simple approach to achieve a metastable metal oxide derived from carbonized metal–organic gels. *Chemical Communications* **55**, 4475-4478 (2019).
76 Latimer, K., Dwaraknath, S., Mathew, K., Winston, D. & Persson, K. A. Evaluation of thermodynamic equations of state across chemistry and structure in the materials project. *npj Computational Materials* **4**, 40 (2018).
77 Allemand, A., Guerin, C., Besnard, C., Billard, R. & Le Petitcorps, Y. A comparison between a new Ultra Fast Pressureless Sintering (UFPS) technology and Spark Plasma Sintering (SPS) for Barium AluminoSilicate metastable phase. *Journal of the European Ceramic Society* **41**, 1524-1529, doi:https://doi.org/10.1016/j.jeurceramsoc.2020.09.054 (2021).
78 Badding, J., Parker, L. & Nesting, D. High pressure synthesis of metastable materials. *Journal of Solid State Chemistry* **117**, 229-235 (1995).
79 Amendola, V. *et al.* Coexistence of plasmonic and magnetic properties in Au89Fe11 nanoalloys. *Nanoscale* **5**, 5611, doi:10.1039/c3nr01119d (2013).
80 Dehnavi, V., Liu, X. Y., Luan, B. L., Shoesmith, D. W. & Rohani, S. Phase transformation in plasma electrolytic oxidation coatings on 6061 aluminum alloy. *Surface and Coatings Technology* **251**, 106-114, doi:10.1016/j.surfcoat.2014.04.010 (2014).
81 Firmansyah, D. A. *et al.* Microstructural Behavior of the Alumina Shell and Aluminum Core Before and After Melting of Aluminum Nanoparticles. *The Journal of Physical Chemistry C* **116**, 404-411, doi:10.1021/jp2095483 (2012).
82 Bouchet, D. & Colliex, C. Experimental study of ELNES at grain boundaries in alumina: intergranular radiation damage effects on Al-L23 and O-K edges. *Ultramicroscopy* **96**, 139-152, doi:10.1016/s0304-3991(02)00437-0 (2003).
83 Fritz, S. *et al.* Correlating the nanostructure of Al-oxide with deposition conditions and dielectric contributions of two-level systems in perspective of superconducting quantum circuits. *Scientific Reports* **8**, doi:10.1038/s41598-018-26066-4 (2018).

84 Park, J., Heo, S., Chung, J. & Park, G.-S. Electron Energy Loss Spectroscopy Characterization of TANOS (TaN/Al2O3/Si3N4/SiO2/Si) Stacks. *Microscopy and Microanalysis* **19**, 109-113, doi:10.1017/s1431927613012440 (2013).
85 Jiang, N. & Spence, J. C. H. In situ EELS study of dehydration of Al(OH)3 by electron beam irradiation. *Ultramicroscopy* **111**, 860-864, doi:10.1016/j.ultramic.2010.11.004 (2011).
86 Ayoola, H. O. *et al.* Origin and Suppression of Beam Damage-Induced Oxygen-K Edge Artifact from γ-Al2O3 using Cryo-EELS. *Ultramicroscopy* **219**, 113127, doi:10.1016/j.ultramic.2020.113127 (2020).
87 Bloch, L., Kauffmann, Y. & Pokroy, B. Size Effect on the Short Range Order and the Crystallization of Nanosized Amorphous Alumina. *Crystal Growth & Design* **14**, 3983-3989, doi:10.1021/cg500580c (2014).
88 Ponsonnet, L. *et al.* EELS analysis of hydrogenated diamond-like carbon films. *Thin Solid Films* **319**, 97-100, doi:10.1016/s0040-6090(97)01094-8 (1998).
89 Mangolini, F., Li, Z., Marcus, M. A., Schneider, R. & Dienwiebel, M. Quantification of the carbon bonding state in amorphous carbon materials: A comparison between EELS and NEXAFS measurements. *Carbon* **173**, 557-564, doi:10.1016/j.carbon.2020.11.021 (2021).
90 Zhang, M. *et al.* In-situ conversion of amorphous carbon to graphene enhances the oxidation resistance of dendritic copper powder. *Diamond and Related Materials* **120**, 108695 (2021).
91 Tian, M., Dyck, O., Ge, J. & Duscher, G. Measuring the areal density of nano-materials by electron energy-loss spectroscopy. *Ultramicroscopy* **196**, doi:10.1016/j.ultramic.2018.10.009 (2018).
92 Marti, R. M., Sarou-Kanian, V., Moran, C. M., Walton, K. S. & Hayes, S. E. NMR Crystallography of Aluminum Carbide: Impurities in the Reagent and Improved 27Al NMR Tensors. *The Journal of Physical Chemistry C* **124**, 7238-7243, doi:10.1021/acs.jpcc.9b11579 (2020).
93 Chandran, C. V. *et al.* Alumina: discriminative analysis using 3D correlation of solid-state NMR parameters. *Chemical Society Reviews* **48**, 134-156, doi:10.1039/c8cs00321a (2019).
94 Lee, S. K., Park, S. Y., Yi, Y. S. & Moon, J. Structure and Disorder in Amorphous Alumina Thin Films: Insights from High-Resolution Solid-State NMR. *The Journal of Physical Chemistry C* **114**, 13890-13894, doi:10.1021/jp105306r (2010).
95 Lee, S. K. & Ahn, C. W. Probing of 2 dimensional confinement-induced structural transitions in amorphous oxide thin film. *Scientific Reports* **4**, doi:10.1038/srep04200 (2015).
96 Samain, L. *et al.* Structural analysis of highly porous γ-Al2O3. *Journal of Solid State Chemistry* **217**, 1-8, doi:10.1016/j.jssc.2014.05.004 (2014).
97 van den Brand, J., Snijders, P. C., Sloof, W. G., Terryn, H. & de Wit, J. H. W. Acid−Base Characterization of Aluminum Oxide Surfaces with XPS. *The Journal of Physical Chemistry B* **108**, 6017-6024, doi:10.1021/jp037877f (2004).
98 Moulder, J. F., Stickle, W. F., Sobol, W. M. & Bomben, K. D.
99 Olefjord, I., Mathieu, H. J. & Marcus, P. Intercomparison of surface analysis of thin aluminium oxide films. *Surface and Interface Analysis* **15**, 681-692, doi:https://doi.org/10.1002/sia.740151108 (1990).
100 Dupin, J.-C., Gonbeau, D., Vinatier, P. & Levasseur, A. Systematic XPS studies of metal oxides, hydroxides and peroxides. *Physical Chemistry Chemical Physics* **2**, 1319-1324, doi:10.1039/A908800H (2000).
101 McCafferty, E. & Wightman, J. P. Determination of the concentration of surface hydroxyl groups on metal oxide films by a quantitative XPS method. *Surface and Interface*

Analysis **26**, 549-564, doi:https://doi.org/10.1002/(SICI)1096-9918(199807)26:8<549::AID-SIA396>3.0.CO;2-Q (1998).
102 Lee, S. Y., Kim, J., Park, A., Park, J. & Seo, H. Creation of a Short-Range Ordered Two-Dimensional Electron Gas Channel in Al₂O₃/In₂O₃ Interfaces. *ACS Nano* **11**, 6040-6047, doi:10.1021/acsnano.7b01964 (2017).
103 Miller, D. J., Biesinger, M. C. & McIntyre, N. S. Interactions of CO2 and CO at fractional atmosphere pressures with iron and iron oxide surfaces: one possible mechanism for surface contamination? *Surface and Interface Analysis* **33**, 299-305, doi:10.1002/sia.1188 (2002).
104 Beattie, J. M. A., Goss, J. P., Rayson, M. J. & Briddon, P. R. Electron-affinity and surface-stability of aluminium-oxide terminated diamond surfaces. *Diamond and Related Materials* **94**, 137-145, doi:https://doi.org/10.1016/j.diamond.2019.02.009 (2019).
105 Tiwari, A. *et al.* Unexpected change in the electron affinity of diamond caused by the ultra-thin transition metal oxide films. *EPL (Europhysics Letters)* **108**, doi:10.1209/0295-5075/108/46005 (2014).
106 Brito, P., Pinto, H. & Kostka, A. The crystallographic template effect assisting the formation of stable α-Al2O3 during low temperature oxidation of Fe–Al alloys. *Corrosion Science* **105**, 100-108, doi:10.1016/j.corsci.2016.01.007 (2016).
107 Davis, E. M., Duscher, G., Wen, J. & Mukherjee, D. Laser-Induced Trapping of Metastable Amorphous AlOx/C (2.5 < x ≤ 3.5) Nanocomposites: Implications for Use as Solid Phase Gas Generators. *ACS Applied Nano Materials* **6**, 10977-10985, doi:10.1021/acsanm.3c00473 (2023).
108 Stølen, S., Glöckner, R. & Grønvold, F. Nearly stoichiometric iron monoxide formed as a metastable intermediate in a two-stage disproportionation of quenched wüstite. Thermodynamic and kinetic aspects. *Thermochimica Acta* **256**, 91-106, doi:https://doi.org/10.1016/0040-6031(94)02166-L (1995).
109 Ren, X., Zhao, M., Feng, J. & Pan, W. Phase transformation behavior in air plasma sprayed yttria stabilized zirconia coating. *Journal of Alloys and Compounds* **750**, 189-196, doi:https://doi.org/10.1016/j.jallcom.2018.03.011 (2018).
110 Brazhkin, V. V. Metastable phases, phase transformations, and phase diagrams in physics and chemistry. *Physics-Uspekhi* **49**, 719 (2006).
111 Luo, Y., Tan, W., Suib, S. L., Qiu, G. & Liu, F. Dissolution and phase transformation processes of hausmannite in acidic aqueous systems under anoxic conditions. *Chemical Geology* **487**, 54-62, doi:https://doi.org/10.1016/j.chemgeo.2018.04.016 (2018).
112 Khawam, A. & Flanagan, D. R. Solid-State Kinetic Models: Basics and Mathematical Fundamentals. *The Journal of Physical Chemistry B* **110**, 17315-17328, doi:10.1021/jp062746a (2006).
113 Salasin, J. R. & Rawn, C. In-Situ Kinetic Investigation of Calcium Aluminate Formation. *Ceramics* **1**, 175-197 (2018).
114 Gotor, F. J., Criado, J. M., Malek, J. & Koga, N. Kinetic Analysis of Solid-State Reactions: The Universality of Master Plots for Analyzing Isothermal and Nonisothermal Experiments. *The Journal of Physical Chemistry A* **104**, 10777-10782, doi:10.1021/jp0022205 (2000).
115 Zhou, R.-S. & Snyder, R. L. Structures and transformation mechanisms of the η, γ and θ transition aluminas. *Acta Crystallographica Section B: Structural Science* **47**, 617-630 (1991).
116 Barcikowski, S. & Compagnini, G. Advanced nanoparticle generation and excitation by lasers in liquids. *Phys. Chem. Chem. Phys.* **15**, 3022-3026, doi:10.1039/c2cp90132c (2013).

117 Matsumi, Y. *et al.* Hyperthermia generated by magnetic nanoparticles for effective treatment of disseminated peritoneal cancer in an orthotopic nude-mouse model. *Cell Cycle* **20**, 1122-1133, doi:10.1080/15384101.2021.1919441 (2021).
118 Manuchehrabadi, N. *et al.* Improved tissue cryopreservation using inductive heating of magnetic nanoparticles. *Science Translational Medicine* **9**, eaah4586, doi:10.1126/scitranslmed.aah4586 (2017).
119 Wang, X. *et al.* Iron carbides: Magic materials with magnetic and catalytic properties. *Journal of Magnetism and Magnetic Materials* **489**, 165432, doi:https://doi.org/10.1016/j.jmmm.2019.165432 (2019).
120 Wang, J. & Hou, Y. Iron Carbide Nanostructures: An Emerging Material for Tumor Theranostics. *Accounts of Materials Research* **3**, 89-99, doi:10.1021/accountsmr.0c00018 (2022).
121 Wang, H. H., Li, G. Q., Ma, J. H. & Zhao, D. The stability, characteristics and magnetic properties of iron carbide from an oolitic hematite. *RSC Advances* **7**, 44456-44462, doi:10.1039/c7ra07886b (2017).
122 Masoudi, A. *et al.* Long-term investigation on the phase stability, magnetic behavior, toxicity, and MRI characteristics of superparamagnetic Fe/Fe-oxide core/shell nanoparticles. *International Journal of Pharmaceutics* **439**, 28-40, doi:https://doi.org/10.1016/j.ijpharm.2012.09.050 (2012).
123 Signorini, L. *et al.* Size-dependent oxidation in iron/iron oxide core-shell nanoparticles. *Physical Review B* **68**, 195423, doi:10.1103/PhysRevB.68.195423 (2003).
124 Sergiienko, R. *et al.* Synthesis of Fe-filled carbon nanocapsules by an electric plasma discharge in an ultrasonic cavitation field of liquid ethanol. *Journal of Materials Research* **21**, 2524-2533, doi:10.1557/jmr.2006.0316 (2006).
125 Pang, Y. L., Lim, S., Ong, H. C. & Chong, W. T. Research progress on iron oxide-based magnetic materials: synthesis techniques and photocatalytic applications. *ceramics International* **42**, 9-34 (2016).
126 Gul, S., Khan, S. B., Rehman, I. U., Khan, M. A. & Khan, M. I. A Comprehensive Review of Magnetic Nanomaterials Modern Day Theranostics. *Frontiers in Materials* **6**, doi:10.3389/fmats.2019.00179 (2019).
127 Mukherjee, D. & Hu, S. Compositions, systems and methods for producing nanoalloys and/or nanocomposites using tandem laser ablation synthesis in solution-galvanic replacement reaction. US patent US 11,127,956 B2 (2021).
128 Hu, S. *et al.* A facile and surfactant-free route for nanomanufacturing of tailored ternary nanoalloys as superior oxygen reduction reaction electrocatalysts. *Catalysis Science & Technology* **7**, 2074-2086, doi:10.1039/c7cy00073a (2017).
129 Mokhtarnejad, M., Ribeiro, E. L., Mukherjee, D. & Khomami, B. 3D printed interdigitated supercapacitor using reduced graphene oxide-MnOx/Mn3O4 based electrodes. *RSC Advances* **12**, 17321-17329, doi:10.1039/D2RA02009B (2022).
130 Seol, M.-L. *et al.* All-Printed In-Plane Supercapacitors by Sequential Additive Manufacturing Process. *ACS Applied Energy Materials* **3**, 4965-4973, doi:10.1021/acsaem.0c00510 (2020).
131 Kariman, B. S., Aghamir, F. M. & Yousefi, H. R. Synthesis of Au/Fe3O4 Magnetic Nanoparticles by Laser Ablation in Organic Solvents. *Journal of Cluster Science* **26**, 1373-1388, doi:10.1007/s10876-014-0820-3 (2015).
132 Moussa, S., Atkinson, G. & El-Shall, M. S. Laser-assisted synthesis of magnetic Fe/Fe2O3 core: carbon-shell nanoparticles in organic solvents. *Journal of Nanoparticle Research* **15**, 1470, doi:10.1007/s11051-013-1470-3 (2013).
133 Amendola, V., Riello, P. & Meneghetti, M. Magnetic Nanoparticles of Iron Carbide, Iron Oxide, Iron@Iron Oxide, and Metal Iron Synthesized by Laser Ablation in Organic

Solvents. *The Journal of Physical Chemistry C* **115**, 5140-5146, doi:10.1021/jp109371m (2011).
134 Amagasa, S., Nishida, N., Kobayashi, Y. & Yamada, Y. Effect of laser irradiation on iron carbide nanoparticles produced by laser ablation in ethanol. *Hyperfine Interactions* **238**, doi:10.1007/s10751-017-1454-2 (2017).
135 Kamali-M, S., Ericsson, T. & Wäppling, R. Characterization of iron oxide nanoparticles by Mössbauer spectroscopy. *Thin Solid Films* **515**, 721-723, doi:https://doi.org/10.1016/j.tsf.2005.12.180 (2006).
136 Joos, A., Rümenapp, C., Wagner, F. E. & Gleich, B. Characterisation of iron oxide nanoparticles by Mössbauer spectroscopy at ambient temperature. *Journal of Magnetism and Magnetic Materials* **399**, 123-129, doi:https://doi.org/10.1016/j.jmmm.2015.09.060 (2016).
137 Liu, X.-W. *et al.* Mössbauer Spectroscopy of Iron Carbides: From Prediction to Experimental Confirmation. *Scientific Reports* **6**, 26184, doi:10.1038/srep26184 (2016).
138 Amelse, J. A., Grynkewich, G., Butt, J. B. & Schwartz, L. H. Moessbauer spectroscopic study of passivated small particles of iron and iron carbide. *The Journal of Physical Chemistry* **85**, 2484-2488, doi:10.1021/j150617a015 (1981).
139 Chuev, M. A. Mössbauer Spectroscopy of Magnetic Nanoparticles: A Historical Perspective and State of the Art. *Crystallography Reports* **65**, 387-392, doi:10.1134/s1063774520030098 (2020).
140 Frias Batista, L. M., Nag, A., Meader, V. K. & Tibbetts, K. M. Generation of nanomaterials by reactive laser-synthesis in liquid. *Science China Physics, Mechanics & Astronomy* **65**, doi:10.1007/s11433-021-1835-x (2022).
141 Ramadhan, A. *et al.* Synthesis of hydrogen- and methyl-capped long-chain polyynes by intense ultrashort laser pulse irradiation of toluene. *Carbon* **118**, 680-685, doi:10.1016/j.carbon.2017.03.096 (2017).
142 Frias Batista, L. M. *et al.* How Pulse Width Affects Laser Ablation of Organic Liquids. *The Journal of Physical Chemistry B* **127**, 6551-6561, doi:10.1021/acs.jpcb.3c03708 (2023).
143 Muhammed Shafi, P. & Chandra Bose, A. Impact of crystalline defects and size on X-ray line broadening: A phenomenological approach for tetragonal SnO₂ nanocrystals. *AIP Advances* **5**, 057137, doi:10.1063/1.4921452 (2015).
144 Suvorova, E. I. & Buffat, P. A. Size effect in X-ray and electron diffraction patterns from hydroxyapatite particles. *Crystallography Reports* **46**, 722-729, doi:10.1134/1.1405856 (2001).
145 Londoño-Restrepo, S. M., Jeronimo-Cruz, R., Millán-Malo, B. M., Rivera-Muñoz, E. M. & Rodriguez-García, M. E. Effect of the Nano Crystal Size on the X-ray Diffraction Patterns of Biogenic Hydroxyapatite from Human, Bovine, and Porcine Bones. *Scientific Reports* **9**, doi:10.1038/s41598-019-42269-9 (2019).
146 Weber, R., Fell, C. R., Dahn, J. R. & Hy, S. Operando X-ray Diffraction Study of Polycrystalline and Single-Crystal Li_xNi_{0.5}Mn_{0.3}Co_{0.2}O₂. *Journal of The Electrochemical Society* **164**, A2992-A2999, doi:10.1149/2.0441713jes (2017).
147 Knappett, B. R. *et al.* Characterisation of Co@Fe3O4 core@shell nanoparticles using advanced electron microscopy. *Nanoscale* **5**, 5765, doi:10.1039/c3nr33789h (2013).
148 Mann, D. K. *et al.* Electrocatalytic water oxidation over AlFe₂B₂. *Chemical Science* **10**, 2796-2804, doi:10.1039/c8sc04106g (2019).

149 Cavé, L., Al, T., Loomer, D., Cogswell, S. & Weaver, L. A STEM/EELS method for mapping iron valence ratios in oxide minerals. *Micron* **37**, 301-309, doi:https://doi.org/10.1016/j.micron.2005.10.006 (2006).
150 Hufschmid, R. *et al.* Nanoscale Physical and Chemical Structure of Iron Oxide Nanoparticles for Magnetic Particle Imaging. *physica status solidi (a)* **216**, doi:10.1002/pssa.201800544 (2018).
151 Almeida, T. P. *et al.* Visualized effect of oxidation on magnetic recording fidelity in pseudo-single-domain magnetite particles. *Nature Communications* **5**, 5154, doi:10.1038/ncomms6154 (2014).
152 Bischoff, J. & Motta, A. T. EFTEM and EELS analysis of the oxide layer formed on HCM12A exposed to SCW. *Journal of Nuclear Materials* **430**, 171-180, doi:https://doi.org/10.1016/j.jnucmat.2012.06.017 (2012).
153 Auerbach, H., Giammanco, G. E., Schünemann, V., Ostrowski, A. D. & Carrano, C. J. Mössbauer Spectroscopic Characterization of Iron(III)–Polysaccharide Coordination Complexes: Photochemistry, Biological, and Photoresponsive Materials Implications. *Inorganic Chemistry* **56**, 11524-11531, doi:10.1021/acs.inorgchem.7b00686 (2017).
154 Rodriguez, J. H. *et al.* Mössbauer Spectroscopy of the Spin-Coupled Fe3+−Fe2+ Center of Reduced Uteroferrin. *The Journal of Physical Chemistry* **100**, 6849-6862, doi:10.1021/jp9532529 (1996).
155 Rhodes, S. *et al.* Iron encapsulated carbon nanotube composites embedded in alumina with enhanced magnetic properties. *Journal of Physics and Chemistry of Solids* **161**, 110455, doi:https://doi.org/10.1016/j.jpcs.2021.110455 (2022).
156 Aydin, A., Guler, E., Aktas, H. & Gungunes, H. Mössbauer studies on athermal martensite formation in an fe-ni-mn alloy. *Bulletin of Materials Science* **25**, 359-360, doi:10.1007/BF02708009 (2002).
157 Tanaka, T., Nasu, S., Huang, B., Ishihara, K. N. & Hideo Shingu, P. Mössbauer spectroscopy of nanocrystalline pure iron prepared by mechanical milling. *Nuclear Instruments and Methods in Physics Research Section B: Beam Interactions with Materials and Atoms* **76**, 195-196, doi:https://doi.org/10.1016/0168-583X(93)95177-7 (1993).
158 Desmarais, J. *et al.* Fe Mössbauer isomer shift of pure iron and iron oxides at high pressure-An experimental and theoretical study. *The Journal of Chemical Physics* **154**, 214104, doi:10.1063/5.0048141 (2021).
159 David, B. *et al.* Powders with superparamagnetic Fe3C particles studied with Mössbauer spectrometry. *Journal of Physics: Conference Series* **217**, 012097, doi:10.1088/1742-6596/217/1/012097 (2010).

Appendix: Publications and Conference Presentations

Published:

1. E. M. Davis, G. Duscher, J. Wen, D. Mukherjee‡, **(2023)** *"Laser-induced trapping of metastable amorphous-AlO_x/C (2.5< x ≤3.5) nanocomposites."* **ACS Applied Nanomaterials, 6 (13),** 10977 **(Impact Factor: 5.9)** https://doi.org/10.1021/acsanm.3c00473
2. E. M. Davis, J. L. Gottfried, G. Duscher, D. Mukherjee‡, **(2022)** "*Laser-induced trapping of metastable nanocomposites as high-performance energetic additives."* **Journal of DoD Research & Engineering, 5 (4)** 67. *[LIMITED DISTRIBUTION peer-reviewed journal]*
3. E. L. Ribeiro, E. M. Davis, M. Mokhtarnejad, S. Hu, D. Mukherjee‡, B. Khomami‡, **(2021)** *"MOF-derived PtCo/Co_3O_4 nanocomposites in carbonaceous matrices as high-performance ORR electrocatalysts synthesized via laser ablation techniques."* **Catalysis Science & Technology, 11**, 3002. **(Impact Factor: 5.7)** ***Selected for front cover*.** https://doi.org/10.1039/D0CY02099K
4. E. M. Davis, E. Ribeiro, S. Kamali, J. Wen, C. Johnson, J. Johnson, B. Khomami, D. Mukherjee‡, **(2023) "***Fe-carbide/Fe-oxide-based Nanocomposites Synthesized as Magnetic Nanomaterials via Laser Ablation Synthesis in Solution (LASiS)."* **Applied Surface Science, 658, 159682. (Impact Factor: 6.7)**

   https://doi.org/10.1016/j.apsusc.2024.159682

Submitted:

1. E. M. Davis, Claudia Rawn, Matthew G. Boebinger, D. Mukherjee‡, **ACS Chemistry of Materials (2024) "***Kinetic Analyses for Solid-State Phase Transition of Metastable Amorphous-AlO_3 Nanostructures into Crystalline Alumina Polymorphs"*

In preparation:

1. E. M. Davis, et. al, D. Mukherjee‡, **(2024) "***Using LASiS to alter metastability for hyper oxidized amorphous-AlO_x/C nanocomposites"*

Patents:

• E. Davis, D. Mukherjee‡, **(2023)** "Metastable metal/intermetallic, ceramic and carbon derived nanocomposites as additives for composite joining adhesives with engineered multi-functional properties," **Patent Application Submitted with UTRF (Disclosure Number: UTRF PD 23103)**

CONFERENCE & SYMPOSIUM PRESENTATIONS:

- Elijah Davis*, Gerd Duscher, Jianguo Wen, Dibyendu Mukherjee, *"Laser-Induced Trapping of Metastable Amorphous-AlO_x/C (2.5< x ≤3.5) Nanocomposites Stabilized by Carbon Interfaces—Implications for Solid-Phase Gas Generator Additives"* **MRS Fall Meeting,** Nov. 25-31, 2023, Boston, MA.
- Elijah Davis*, Gerd Duscher, Jianguo Wen, Dibyendu Mukherjee, *"Laser-Induced Trapping of Metastable Amorphous-AlO_x/C (2.5< x ≤3.5) Nanocomposites,"* **ACS Fall Meeting,** Aug. 13-17, 2023, San Francisco, CA.
- Elijah Davis, Seyyed A. Davari, Gerd Duscher, Dibyendu Mukherjee*, *"Reactive Laser Ablation Synthesis in Solution (r-LASiS): A facile route for one-pot synthesis of Al/C-based composite energetic nanomaterials (ENMs) with tailored interfacial structures,"* **TechConnect World Innovation Conference & Expo,** June 21, 2023, National Harbor, MD.
- Elijah Davis, Dibyendu Mukherjee, Jianguo Wen, Gerd Duscher, Catherine A.M. Dillier, Jennifer L. Gottfried*, *"Laser-induced Metastability in AlO_x/C nanocomposites for the Design of Next-Generation Energetic Additives,"* **JANNAF Interagency Propulsion Committee Meeting,** May 23, 2023, Pittsburgh, PA, USA. [LIMITED DISTRIBUTION presentation and proceedings paper]
- Elijah Davis*, Gerd Duscher, Jianguo Wen, Dibyendu Mukherjee, *"Laser-Induced Trapping of Metastable Amorphous-AlO_x/C (2.5< x ≤3.5) Nanocomposites Stabilized by Carbon Interfaces—Implications for Solid-Phase Gas Generator Additives"* **MRS Spring Meeting,** May. 08-13, 2022, Honolulu, Hi.

Vita

Elijah Grew up from a young age with a love for science. He attended community college until he transferred to the University of Tennessee as an undergraduate. He started as an undergraduate researcher and when asked if he wanted to stay for a PhD he jumped at the opportunity. He loved doing research, discovering new things, solving mysteries and answering scientific questions. His curiosity led him down paths of research that he never thought would be possible when he started. If the young him were asked where he saw himself at 26, never in his wildest dreams would he have expected to have been researching rocket science and collaborating with researchers from around the world. The people he met along the way continue to surprise him and encourage excitement and facilitate a love of science. He exits with a PhD, worn out but excited. Grabbing life by the reins and holding on by the seat of his pants.